SYNTHESIS, STRUCTURAL AND MAGNETIC STUDIES OF COBALT DOPED NICKEL-ZINC FERRITE NANOPARTICLES

Thesis submitted in fulfillment of the requirements for the degree of

DOCTOR OF PHILOSOPHY

By

RAJINDER KUMAR

Department of Physics and Materials Science

JAYPEE UNIVERSITY OF INFORMATION TECHNOLOGY
WAKNAGHAT, DISTRICT SOLAN, H.P., INDIA

NOVEMBER 2017

DECLARATION

I hereby declare that the work contained in the PhD thesis entitled **"SYNTHESIS, STRUCTURAL AND MAGNETIC STUDIES OF COBALT DOPED NICKEL-ZINC FERRITE NANOPARTICLES"** is original and has been done by me under the supervision of Prof. P. B. Barman (Supervisor) and Dr. Ragini Raj Singh (Co-supervisor) submitted to **Jaypee University of Information Technology, Waknaghat, India**. The work has not been submitted to any other organization for any degree or diploma.

Date:11-11-2017

RAJINDER KUMAR

Department of Physics and Materials Science

Jaypee University of Information Technology

Waknaghat, Solan, H.P., India-173234

CERTIFICATE

This is to certify that the work reported in the Ph.D. thesis entitled "**SYNTHESIS, STRUCTURAL AND MAGNETIC STUDIES OF COBALT DOPED NICKEL-ZINC FERRITE NANOPARTICLES**", which is being submitted by Rajinder Kumar for the award of degree of Doctor of Philosophy in Physics by Jaypee University of Information Technology, Waknaghat, India, is the record of the candidate's own work, carried out under our supervision. This work has not been submitted partially or wholly to any other university or institute for the award of this or any other degree or diploma.

Date: 11-11-2017

Prof. P. B. Barman

Supervisor

Department of Physics and Materials Science

JUIT, Waknaghat, Solan (H.P), India

Email: pb.barman@juit.ac.in

Phone: +919418228268

Dr. Ragini Raj Singh

Co-supervisor

Department of Physics and Materials Science

JUIT, Waknaghat, Solan (H.P), India

Email: raginirajsingh@gmail.com

Phone: +919625643296

For my loving family............

ACKNOWLEDGEMENT

First of all, from the depth of my heart I express my deep sincere gratitude to the Almighty for the blessings He had bestowed upon me to do this work.

*I am immensely pleased to place on record my profound gratitude and heartfelt thanks to my supervisor, **Prof. P. B. Barman,** Head of the Department, Department of Physics and Materials Science, for his guidance and constant encouragement during my research. He provided inspiring guidance for the successful completion of my research work. I deem it as my privilege to work under his able guidance. I ever remain grateful to him.*

*I great fully acknowledged and thank my co-supervisor **Dr. Ragini Raj Singh,** Assistant Professor of Physics Department of Physics and Materials Science, Jaypee University of Information Technology for her guidance, help, encouragement and cooperation throughout my research work.*

*I insistently express my loyal and venerable thanks to **Prof. (Dr.) Vinod Kumar** (VC, JUIT), **Brig. (Retd.) K.K. Marwah** (Registrar JUIT), **Prof. (Dr.) Samir Dev Gupta** (Dean or Director JUIT) and **Prof. T. S Lamba** (Ex. Dean JUIT) for providing opportunity to pursue my research work at Jaypee University of Information Technology, Waknaghat (H.P).*

*I owe my thanks to **Prof. Sunil Kumar Khah, Dr. Vineet Sharma, Dr. Pankaj Sharma, Dr. Rajesh Kumar, Dr. Surajit Kumar Hazra, Dr. Sanjiv Kumar Tiwari** (**JUIT**) and **Dr. Manoj Kumar (JIIT Noida)** for providing me assistance, moral support, suggestions and necessary facilities in the department during the course of my research work.*

*I am also thankful to all members of technical and non-technical staff **Mr. Kamlash Mishra,** Mr. **Ravender Tiwari and Mr. Deepak Singh** for their valuable contributions.*

I also thanks to all Universities (JIIT Noida, IIT Rorkee, Panjab University) for allowing me the facilities for characterization.

It was indeed my good luck to have seniors Hitanshu Kumar, Ankush Thakur, Abhishek Kandwal, Pawan Kumar Jai Vardhan and Arun Kumar, who extended their support in all possible ways. I thank them for always being there to guide and encourage whenever the journey got tough. I am also privileged to have friends who always stood beside me. I extend my heartfelt thanks to my friend Hitanshu Kumar and Bandana Bharti. I also thank my other colleagues Rajinder Singh, Dikshita Gupta, Sarita kango, Krishna Hari Sharma, Prashant Thakur, Rohit Sharma, Jonny Dhiman, Asha Kumari and Neha Kondal,

This work would have taken scans the moral supports and encouragement rendered by my family. I can never enough thanks to my brother in law and sisters for supporting my decision to take research and always being there.

Words cannot express my humble gratitude to my dear parents for their affectionate encouragement and blessing to complete this research work. My research work have couldn't be possible without their unconditional love and support.

Date*:*   **Rajinder Kumar**

ABSTRACT

This thesis work preferentially concerned with the tunable structural and magnetic properties of undoped and Co doped Ni-Zn ferrite nanoparticles synthesized by sol-gel method and new optimized non-aqueous method. The changing properties of prepared nanoparticles have been explained in terms of distribution of cations, synthesis method and annealing temperature.

The work has been systematically described in six different chapters as follows:

Chapter I contains a brief introduction of nanotechnology, history of ferrites and magnetism, classifications of ferrites, magnetism in ferrites, synthesis method and spinel ferrites nanoparticles properties.

Chapter II describes the synthesis of ferrite nanoparticles and experimental techniques used for the characterization of prepared nanoparticles for structural, morphology, stoichiometry and magnetic properties.

Chapter III intended to synthesis, structural and magnetic studies of Co doped Ni-Zn ferrite nanoparticles. All the nanoparticles have been prepared by sol-gel method and annealed at 700°C. We have employed X-ray diffraction (XRD), Field emission scanning electron microscopy (FESEM), Energy dispersive X-ray spectroscopy (EDX) and Vibrating sample magnetometer (VSM).

Chapter IV describes the effect of annealing temperature on structural and magnetic properties of Co doped Ni-Zn ferrite nanoparticles. The nanoparticles were also prepared by sol-gel method but annealing temperature is 1100$^{\mathrm{O}}$C.

Chapter V defines the development of Co doped Ni-Zn ferrite nanoparticles by non-aqueous method and their structural and magnetic properties studies. In this chapter the nanoparticles have been prepared by optimized new method that is non-aqueous method and characterized for their structural and magnetic properties.

Chapter VI shows the overall conclusion of work**.**

CONTENTS

LIST OF FIGURES

LIST OF TABLES

LIST OF PUBLICATIONS

1. **Rajinder Kumar**, Hitanshu Kumar, Manoj Kumar, Ragini Raj Singh, and P. B. Barman. "Enhanced Saturation Magnetization in Cobalt Doped Ni-Zn Ferrite Nanoparticles." Journal of Superconductivity and Novel Magnetism 28, no. 12 (2015): 3557-3564.

2. **Rajinder Kumar**, Hitanshu Kumar, Ragini Raj Singh, and P. B. Barman. "Variation in magnetic and structural properties of Co-doped Ni–Zn ferrite nanoparticles: a different aspect." Journal of Sol-Gel Science and Technology 78, no. 3 (2016): 566-575.

3. **Rajinder Kumar**, Ragini Raj Singh, and P. B. Barman. "Cobalt Doped Nickel Zinc Ferrite nanoparticles–Xrd Analyses an Insight". International Journal of Scientific & Engineering Research 5 (5) 2014.

4. **Rajinder Kumar**, Hitanshu Kumar, Ragini Raj Singh, and P. B. Barman. "Structural analysis of emerging ferrite: Doped nickel zinc ferrite." In *ADVANCED MATERIALS AND RADIATION PHYSICS (AMRP-2015):* 4th National Conference on Advanced Materials and Radiation Physics, vol. 1675, p. 030003. AIP Publishing, 2015.

PARTICIPATION / PRESENTATIONS IN WORKSHOPS / CONFERENCES

1. One-week Workshop on "Nanotechnology (Fabrication and Characterization)" December 11, 2013 at JUIT Waknaghat.

2. 1st "International Convention of Engineering and Management" (iCEM-2014) (April 26-27, 2014) [JUIT Waknaghat, Solan (H.P), India].

3. National Conference on "Advanced Materials and Radiation Physics" (AMRP-2015) (March 13-14, 2015) [SLIET, Longowal (Punjab) India].

4. 2nd International Convention of Engineering and Management" (iCEM-2015) (April 4-5, 2015) [JUIT Waknaghat, Solan (H.P), India].

5. International conference on "Science Emerging Scenario and Future Challenged" (SESFC 2016) (June 11-12, 2016) [Dharamshala (H.P), India].

CHAPTER-1

INTRODUCTION

1.1 Introduction

The technology term refers to the collection of techniques that is used by scientist to design the materials for different applications. Technology describes the study of somewhat and also says that the branch of knowledge of a discipline. Now a day's everything depends on technology and it decrease the social efforts and increase the efficiency or no one can carry on without it. Nanoscience is an interdisciplinary field of science which deals with the study of the properties or phenomena of matters at atomic, molecular and macromolecular scale. "Nanotechnology" means the technology that performs on nanoscale level by controlling shape and size at nanometer scale for design, production, characterization and application. Nanotechnology first described by renowned physicist Richard Feynman in a meeting held at American Physical Society, California Institute of Technology in 1959 entitled "There is plenty of room at the bottom- An invitation to enter a new field of physics". The term "Nano" comes from Greek word "dwarf "which means Nano. One nanometer designated as 1nm and is equal to 10^{-9} m, means one nanometer in length is approximately equivalent to width of 6 carbon atoms or 10 water molecules [1-2]. Development of nanoscience and investigation on nanostructure was initiated around 1980. The field nanotechnology is a versatile field of the technology and proved as a boon for many fields such as material technology [3], information technology [4], cellular and molecular biology [5], bio-technology [6], manufacturing [7], Nano-electronics [8], communications [9], robotics [10], etc. Nanomaterials or nanostructured materials are those materials whose one dimension at least lies in 1-100 nm range which includes nanoparticles, quantum dots, nano rods, nano wire and nano rings. The nanoparticles or nanomaterials are used in many applications which shown in figure 1.1 [11]. Thin films and bulk materials are also constructed from nanoscale building blocks or nanoscale structure [12]. Richard Feynman explored the manipulating possibility of material at individual atomic or molecular level. Norio Taniguchi, a scientist at the University of Tokyo in 1974 has first introduced the concept of nanotechnology. He referred the nanotechnology for engineer, the materials precisely at nanometer level [2]. The research on nanoscience development and nanostructure investigation was started around 1980 with the invention of scanning tunneling microscope (STM) and then nanostructure solids concept was suggested [13-14]. The nanostructure size of a single sugar molecule is about 1 nm which was measured by Albert Einstein during his doctoral study from experimental diffusion data of sugar in water [15].

Figure 1.1: Applications of nanoparticles in various fields [11].

Properties of any material depend on its size and it was mentioned by Michael Faraday in 1857 during a lecture on the optical properties of Gold noticeable that "a mere variation in size of the particles gave rise to a variety of resultant colors" [16]. The creations of Atomic Force Microscopy (AFM) in 1986, first electron transistor in 1987 and discovery of carbon nanotube in 1991 are the significant signs in growth of the field nanotechnology. Some of the historical contents about the nanotechnology development are listed in table1.1 [17].

Table 1.1: Historical content about the nanotechnology development [17].

Year	Development in Nanotechnology
1959	R. Feynman initiated thought process
1974	The term nanotechnology was used by Taniguchi for the first time.
1981	IBM Scanning Tunneling Microscope
1985	Bucky Ball
1986	First book on nanotechnology Engines of Creation published by K. Eric Drexler, Atomic Force Microscope
1989	IBM logo was made with individual atoms
1991	S. Iijima discovered Carbon Nano tube for the first time.
1999	1st nano medicine book by R. Freitas "Nano medicine" was published
2000	For the first time National Nanotechnology Initiative was launched
2001	For developing theory of nanometer-scale electronic devices and for synthesis and characterization of carbon nanotube and nano wires, Feynman Prize in Nanotechnology was awarded
2002	Feynman Prize in Nanotechnology was awarded for using DNA to enable the self-assembly of new structures and for advancing our ability to model molecular machine systems.
2003	Feynman Prize in Nanotechnology was awarded for modeling the molecular and electronic structures of new materials and for integrating single molecule biological motors with nano-scale silicon devices.
2004	First policy conference on advanced nanotech was held. First center for nano mechanical systems was established, Feynman Prize in Nanotechnology was awarded for designing stable protein structures and for constructing a novel enzyme with an altered function.
2005-2010	3D Nano systems like robotics, 3D networking and active nano products that change their state during use were prepared.
2011	Era of molecular nano technology started

1.1.1 History of ferrites and magnetism

Ferrites are the ferrimagnetic materials which made up of iron oxide and metal oxides. Iron oxide is the main component of the ferrites. Ferrite is a very important magnetic material from commercial point of view having electrical, magnetic and dielectric properties. The ferrite term come from the Latin word for iron having different meaning for different field of scientist. For the field of science and metal technology, ferrite signifies pure iron. Geologists describes that ferrites are a group mineral that contains iron oxide as a principle component. The electrical engineer defines that ferrites are also iron oxide based group of materials having useful magnetic and dielectric properties. The first naturally occurring magnetic material iron oxide known as lodestone (Fe_3O_4) or magnetite was first found in the district of Magnesia in Asia slight [18] and then termed as ferrite. The magnetic properties of magnetite then known by ancient Chinese and used it in compass for navigation [19]. In 1600, William Gilbert describes the magnetic properties of lodestone or magnetite (Fe_3O_4) and published it in first book of magnetism entitled "De Magnete" [20].

The difference between electricity and magnetism is also described by William gilbert and has a great contribution for the discovery of earth magnetic field that itself behaved like a giant magnet. In 1750, a balance has been invented by John Michel, the English geologist for the study of magnetic forces. During 1736-1806, French physicists Charles Augustine de coulomb has established the inverse square law of force between magnetic poles and electric charges. The influence of electric current flowing through a wire on magnetic needle was observed by the Danish physicist Hans Christian Oersted in 1819 and that has established the relation between electricity and magnetism. The temperature dependent magnetic behavior of magnetic materials was discovered by Pierre Curie. During 1946's, the discovery of Magnetic Resonance Imaging (MRI) has been done by M. Purcell and Flix Bloch, an American physicist by means of measuring the magnetic field of nuclei [21]. In this way many researchers have done work for the development of ferromagnetism. Subsequently, the American physicists Samuel Abraham Ooudsmit and George E Uhlenbeek during 1902-1978 gave the concept of electron spin [22]. They showed that electrons have their own spin and magnetic properties at atomic level were measured in terms of magnetic moments. The concept of soft ferrite came into account after the finding of J. L. Snoek in 1945. He synthesized different type of ferrites and found their importance in different fields. Moreover, in 1947, he also published the book entitled "New Development in Ferromagnetic Materials" [23]. In 1948, L Neel developed the basic theory of "spin-spin interaction" of ferrimagnetic materials [24]. He introduced the concept of magnetic sub

lattice interaction and developed a new phase in the field of ferrite. Further, more detailed work on concept of spin interaction has been done by Anderson and Van-Vleck [25-26]. In 1952, Yafet and Kittle have explored the theory of magnetic sub lattice by introducing the triangular arrangement of three sub lattice [27]. Ferrites are magnetic materials and very important from commercials point of view because of their unique properties. The discussion on ferrite properties in detail are being discussed in following sections.

1.1.2 Classification of ferrites based on magnetic properties

According to magnetic properties, ferrites are classified into two categories such as (i) Soft Ferrite and (ii) Hard Ferrite

1.1.2.1 Soft ferrite

Soft ferrites are the magnetic materials which possess low coercivity field and high resistivity. They can be easily magnetized and demagnetized with small application of field. By virtue of low coercivity and high resistivity of soft ferrites, the magnetization can easily reverse without losing much energy or having low hysteresis and eddy current loss. The low loss of these materials thus makes them promising candidates for high frequency applications. Most common examples of soft ferrites are manganese-zinc ferrite, cobalt-zinc ferrite, nickel-zinc ferrite, etc. High saturation magnetization, high resistivity and high permeability, make ferrites usable in transformer core, magnetic recording head, inductor, etc. [27].

1.1.2.2 Hard ferrite

Hard ferrites are permanent magnets which has high value of coercivity and retentivity after magnetization. High coercivity means high value of magneto crystalline anisotropy energy and is the most significant property of hard ferrite. They cannot be easily magnetized or demagnetized with small application of field. Hard ferrites are made up of iron and barium or strontium oxides having high value of magnetic permeability. Hard magnet has tendency to store more magnetic field than iron and widely used in house hold products mainly as refrigerator magnet. The common examples of hard ferrites are strontium ferrite, barium ferrite and cobalt ferrite which are being used in many applications such as permanent magnet, magnetic recording, etc. [28].

1.1.3 Crystal structure of ferrites

On the basis of crystal structure and chemical compositions, ferrites are divided into three different categories: (i) Spinel Ferrites, (ii) Garnets and (iii) Hexa Ferrites.

1.1.3.1 Spinel ferrites

Spinel ferrites have general formula MFe_2O_4 or AB_2O_4 (where M or A is divalent metal cations such as Fe^{2+}, Co^{2+}, Ni^{2+}, Zn^{2+}, etc. and B is Fe^{3+}) belongs to space group Fd3m, that is derived from crystal structure of natural mineral spinel $MgAl_2O_4$, where M is divalent metals cations such as Fe^{2+}, Mn^{2+}, Co^{2+}, Ni^{2+}, Cu^{2+}, etc. [29]. The crystal lattice structure of spinel ferrites is shown in figure 1.2 [30].

AB_2O_4 **spinel** The red cubes are also contained in the back half of the unit cell
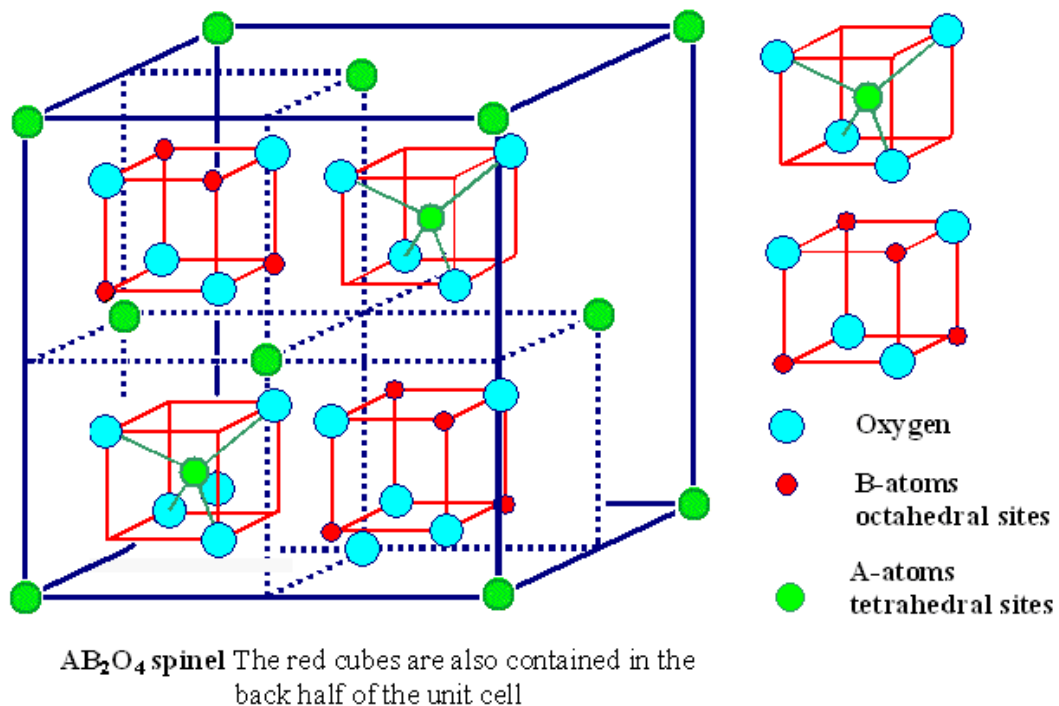
Figure 1.2: Crystal lattice structure of spinel ferrites [30].

In spinel ferrites, 32 oxygen atoms form a unit cell having face centered cubic (FCC) structure arrangement leaving two kind of sites: tetrahedral sites (A) and octahedral sites (B), that is surrounded by four and six oxygen atoms respectively. The FCC structure of spinel ferrites contains 64 tetrahedral sites and 32 octahedral sites (B). To maintain the electrical neutrality of the lattice, there are one eighth of the tetrahedral sites (A) and one half of the octahedral sites (B) are occupied by the cations in a unit cell. The crystal structure of spinel

ferrites has 8 molecules per formula unit cell [31]. On the basic of cations distribution in tetrahedral (A) and octahedral (B) sites, spinel ferrites are divided into three categories: normal spinel, inverse spinel and mixed spinel ferrite structure. When tetrahedral sites (A) are occupied by divalent metal cations and octahedral sites (B) are occupied by trivalent metal cations than the structure is known as normal spinel. The normal spinel ferrites are defined by the formula $(M_{1-\delta}Fe_{\delta})$ ^{A} $[M_{\delta}Fe_{2-\delta}]$ ^{B} O_4, where the first term in bracket described tetrahedral (A) and second term in square bracket described the octahedral (B) sites components while δ is the degree of inversion parameter of cations having 0 values. $ZnFe_2O_4$ is the example of normal spinel ferrite. In inverse spinel ferrites system, all divalent cations are distributed over half of the octahedral sites (B) and trivalent cations distributed over tetrahedral (A), whereas the remaining in octahedral sites. The value of δ in inverse spinel ferrites is 1 and in case of mixed spinel ferrites the value of δ lies $0 < \delta < 1$ [32-33].

1.1.3.2 Garnet ferrites

Garnet ferrites have a crystal structure of garnet minerals $Mn_3Al_2Si_3O_{12}$. Garnet ferrites are formed when Al and Si are replaced by Fe^{3+} ions and Mn is replaced by rare earth cation (R) to form magnetic garnet having general formula $R_3^{3+}Fe_5^{3+}O_{12}$. The garnet ferrite has body centered cubic structure with eight formula units. The garnet ferrites crystal has cubic symmetry and consists of three sub-lattices that are 24 tetrahedral (A), 16 octahedral (B) and 24 dodecahedral (C) sites. The largest dodecahedral sites are occupied by rare earth cations such as Y, La, Er, Gd, Sm, Eu, etc. and tetrahedral (A) and octahedral sites (B) are occupied by Fe^{3+} cations [34-35].

1.1.3.3 Hexagonal ferrites

The hexagonal ferrites and their magnetic properties identification has been firstly done by Went, Rathenau, Gorter, Van Oostershout, Jonker, Wijn and Braun [36]. Hexagonal ferrites are the class of permanent magnet having general formula $MFe_{12}O_{19}$ where M is Ba, Sr, Ca and Pb. The crystal structure of the hexagonal ferrites is made by oxygen ions having close packing hexagonal arrangement unit cell which contains two molecules of $MFe_{12}O_{19}$. The high magneto crystalline anisotropy energy and coercivity of hexagonal ferrites makes it possible to form permanent magnet. On the basis of chemical formula and crystal structure, they are divided into five categories such as M-type or $SrFe_{12}O_{19}$, W-type or $SrMe_2Fe_{16}O_{27}$, Y-type or $SrMe_2Fe_{12}O_{22}$, X-type or $Sr_2Me_2Fe_{28}O_{46}$ and Z-type or $Sr_2Me_2Fe_{24}O_{41}$ [37-38].

1.1.4 Types of magnetism

Magnetism is the property of magnetic materials by which materials are capable to experience an interaction (attractive or repulsive forces) with another substance or by means of applied field. The interaction of the magnetic materials depends upon the magnetic moment of the atoms. The origin of the magnetic moments arises from the orbital motion, spin motion of electron around its axis and change in orbital motion by applied field. The types of magnetic interactions in the magnetic materials depend on un-paired electrons of the atoms. On the basis of magnetic interaction that depends upon alignment of electrons spins and relative arrangement of atoms or molecules under the influence of magnetic field, magnetism is divided into five different categories i.e. (i) Diamagnetism, (ii) Paramagnetism, (iii) Ferromagnetism, (iv) Anti-ferromagnetism and (v) Ferrimagnetism.

1.1.4.1 Diamagnetism

Diamagnetism is the property of the substance that has no unpaired electrons; mean zero magnetic moment and are known as diamagnetic materials. When a diamagnetic material is placed in a magnetic field, the magnetic lines of force are weakly repelled by the materials and this phenomenon is known as diamagnetism. The phenomena of repulsion in these types of materials are caused by the induced orbital moment of atoms of the material that opposed the applied magnetics flux (Lenz's Law). Hence these types of materials possess small and negative susceptibility which is independent of temperature. Copper, gold, diamond, silver, bismuth, zinc, etc. are the examples of diamagnetic materials [39-41].

1.1.4.2 Paramagnetism

Paramagnetism phenomena occur only in those materials whose atoms or molecules has net magnetic moment or unpaired electrons and those materials are identified as paramagnetic materials. When paramagnetic materials are subjected to a magnetic field, the orbital or spin magnetic moment aligned in the direction of the applied field, therefore, weakly attracted by the magnetic field. In the absence of magnetic field, the magnetic moment of the material is randomly oriented (no net magnetic moment) by means of thermal agitation because of small magnetic moment interaction. These types of materials have small but positive value of susceptibility and have permeability value slightly greater than that of the free space. The susceptibility of these materials are temperature dependent and temperature proportional. When temperature or thermal agitation of the materials increases, then it is harder to align the

magnetic moments in the direction of the applied magnetic field and hence susceptibility decreases according to curie law. Chromium, platinum, aluminium, alkali and alkaline earth metals, etc. are the example of paramagnetic materials [39, 42].

1.1.4.3 Ferromagnetism

Ferromagnetism is a phenomenon that exhibits in ferromagnetic materials by which material is strongly attracted by the magnetic field or with another magnetic material. Ferromagnetism occurs in those magnetic materials which have permanent high magnetic atomic moment even in the absence of applied magnetic field. In ferromagnetic materials, magnetic moments of all ions are oriented in the same direction giving rise to high magnetic moment or high value of saturation magnetization. The magnetic moments interactions between atoms of these types of materials are favored to parallel alignment. The ferromagnetic materials consist of domains. Domains are the region, in which atomic magnetic moments of ions are aligned in particular direction. Without applied magnetic field, all domains within the material are randomly aligned. The exchange interaction within the domains is very strong because of atomic spins causing the materials to retain magnetization even after removal of magnetic field. The magnetic properties of ferromagnetic materials are temperature dependent. When ferromagnetic material is heated to certain temperature limit (Curie temperature), the behavior of materials gets changed to paramagnetic. Above this temperature, the thermal energy is sufficiently high to overcome the atomic moment exchange interaction causing atomic magnetic moment flip in random direction. Ferromagnetic materials have high value of permeability, susceptibility and Curie temperature. Nickel, Cobalt and iron are the examples of ferromagnetic materials [41, 43].

1.1.4.4 Anti-ferromagnetism

Anti-ferromagnetism is the phenomena in which magnetic spin moment of the adjacent atoms, ions or molecules are aligned antiparallel to each other which causes zero net magnetic moment of the system. The magnetic properties of these types of materials are temperature dependent. At very low temperature the antiparallel ordering between atomic moments is very strong and has no response with applied magnetic field. At high temperature, the antiparallel ordering of some atoms diminishes and magnetic moments align with respect to the applied magnetic field and shows week magnetism. The temperature at which anti-ferromagnetic substances shows some week magnetism is known as Neel temperature. Above

Neel temperature, magnetism of anti-ferromagnetic materials gets changed into typical paramagnetic substances because of thermal agitation. MgO, ZnO, NiO, etc. are the examples of anti-ferromagnetic substances.

1.1.4.5 Ferrimagnetism

Ferrimagnetic materials or ferrites exhibit the phenomena of ferrimagnetism by virtue of super exchange interaction between metal and oxygen ions electrons. The alignment of spins magnetic moments of ferrimagnetic materials are similar to that of antiferromagnetic materials *i. e.* antiparallel alignment, but have different magnitude which gives rise to high net magnetic moment. Magnetic behavior of ferrimagnetic materials is very similar to magnetic behavior of ferromagnetic substances. Ferrites are the most important group of ferrimagnetic materials which has high resistivity than ferromagnetic substances. Ferrimagnetism in ferrites are described by Neel's two sub lattice model [24]. Different types of interactions exist in ferrimagnetic materials which hold the magnetization in certain direction as long range. On the basis of Heisenberg's forces, Neel has explained the magnetization of ferrites. There are three types of magnetic interaction exhibited in ferrites materials between magnetic ions such as (i) A-O-A (A-A) interaction, (ii) B-O-B (B-B) interaction and (iii) A-O-B (A-B) interaction, where A and B are designated for tetrahedral and octahedral sites respectively [20, 44]. Here the interaction between metal cations is held through oxygen anion known as indirect interaction. The strength of the magnetic interaction between metal ions which are located on the different sites depends on distance between metals cations and oxygen anions and also on angle between them. The A-B interactions are the strongest interaction than A-A and B-B interaction. In A-A and B-B interactions, the angle between metals cations is too small and distance between metals cations and oxygen anions is too large. The B-B interactions are the much weaker interactions in ferrites system. The dominant A-O-B interactions will align the A and B sub lattice spin in opposite direction that cause net or resultant magnetic moment which is the difference of magnetic moment of A and B sub lattice magnetic ions.

According to Neel two sub lattice model, spinel ferrites nanoparticles exhibited the phenomena of ferrimagnetism. The saturation magnetization or net magnetic moment of the spinel ferrite system $M = |M_B - M_A|$, where M_B and M_A are the total magnetic moment of octahedral (B) and tetrahedral (A) sites respectively. Fe_3O_4 (magnetite), γ - Fe_2O_3 (maghemite) are the examples of ferrimagnetic materials. The magnetic behavior of

diamagnetic, paramagnetic, ferromagnetic, anti-ferromagnetic and ferrimagnetic substances are shown in figure 1.3 [45] and their examples with properties are tabulated in table 1.2.
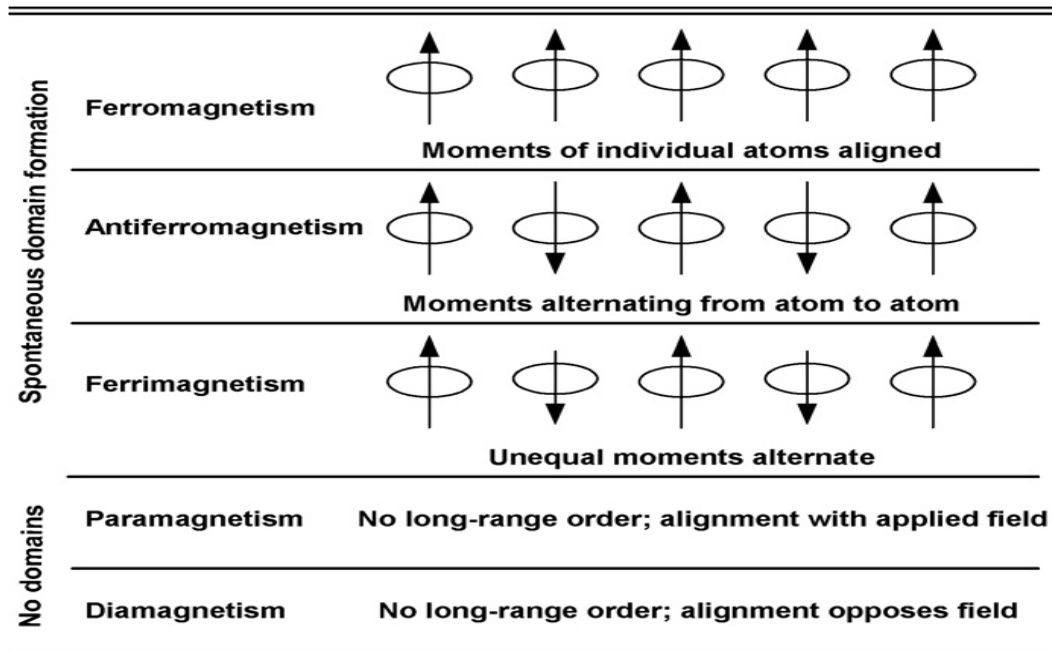
Figure 1.3: Magnetic ordering in diamagnetic, paramagnetic, ferromagnetic, anti-ferromagnetic and ferrimagnetic substances [45].

Table 1.2: Classification of Diamagnetic, Paramagnetic, Ferromagnetic, Anti-ferromagnetic and Ferrimagnetic Materials.

Sr. No.	Class	Magnetic Property	Examples
1	Diamagnetic	Atoms of the material have no permanent dipole.	Copper, gold, diamond, silver, bismuth, zinc
2	Paramagnetic	Atoms of the material have permanent dipole.	Chromium, platinum, aluminium, alkali and alkaline earth metals.
3	Ferromagnetic	Atoms of the material have permanent dipole with parallel alignment.	Nickel, Cobalt, iron
4	Anti-Ferromagnetic	Atoms of the material have permanent dipole with anti-parallel alignment.	MgO, ZnO, NiO
5	Ferrimagnetic	Atoms of the material have different magnitude permanent dipole with anti-parallel alignment.	Fe_3O_4(magnetite), γ-Fe_2O_3 (maghemite

1.1.5 Properties of spinel ferrites nanoparticles

The properties of magnetic nanoparticles depend on particle size, surface effect, cations distribution in tetrahedral (A) and octahedral (B) sites, synthesis techniques, amount and types of dopant and annealing temperature. As the particle size decreases from bulk to nanometer range, there is significant change in the physical, chemical and mechanical properties of the system because of the increase in the surface to volume ratio of atoms in particles [46-47]. The magnetic properties such as magnetic moment or magnetization and magnetic anisotropy of nanoparticle system are different from those of bulk specimen [48]. The magnetic properties of magnetic materials which are size dependent observed in the range of few microns to few nanometers. In bulk form, particles exist in multi domain structure. Individually, domain is the region where all the spins magnetic moments of atoms are aligned in a particular direction and causes uniform magnetization. The magnetization of multi domain structure can be reversed by the moment of domain walls. When the particle size decreases in nanometer range, the domain walls of the system become energetically unfavorable leading to the formation of single domain state where all spins moments are aligned in one direction. The diagrams of multi domain and single domain structure are shown in figure 1.4.
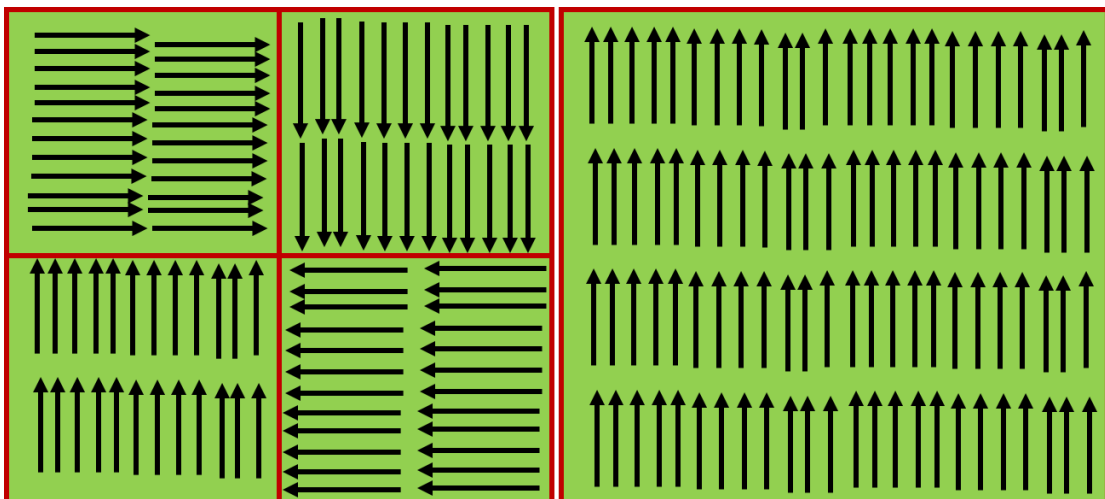
Figure 1.4: Diagram of multi domain and single domain structure.

Single domain state exists in nanometer scale when the size of particles decreases below to critical diameter [49] causing superparamagnetism above the blocking temperature. Above the critical diameter, nanoparticles show the behavior of ferromagnetism hence these

particles have some value of coercivity and retentivity or have hysteresis nature. The size dependent variation in coercivity of magnetic nanoparticles is shown in figure 1.5 [47].
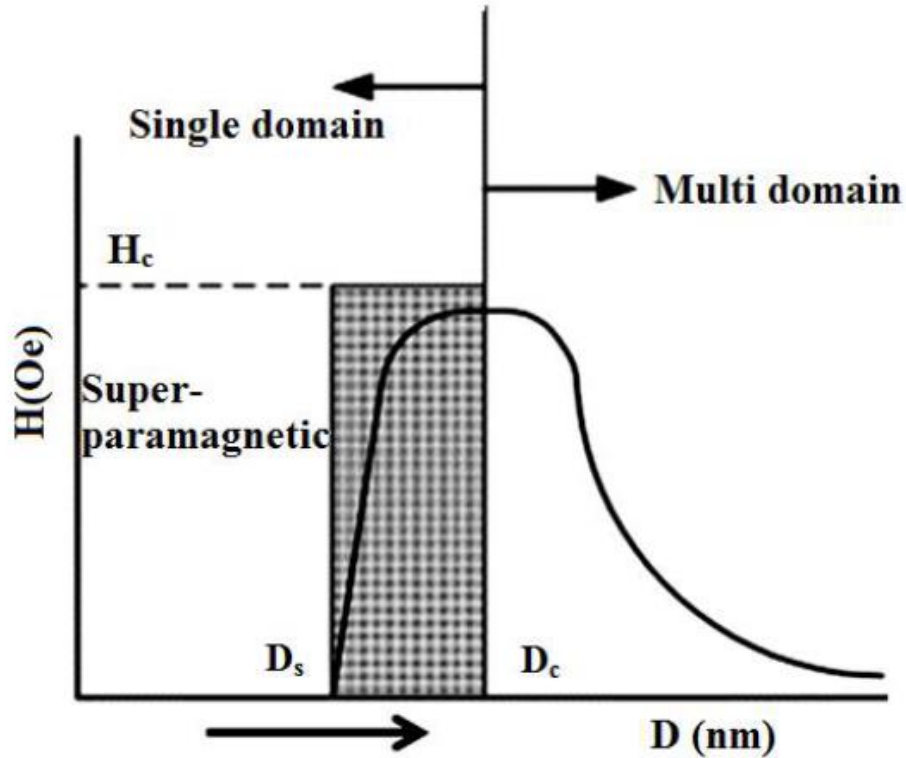
Figure 1.5: Particle size dependent coercivity [47].

The coercivity of the material is known as the reverse magnetic field which required to demagnetize the magnetic materials after saturation. The coercivity of the materials is maximum when the size of the particle reached to its critical diameter because the magnetization was not achieved due to rotation of domains wall. The increase in the value of coercivity with decreasing particles size is attributed to conversion of multi domains materials into mono domains materials [49]. When particle size reduced below to its critical diameter, coercivity of the materials decreases by virtue of thermal effect and follow the equation [50]:

$$H_C = g - h/D^{1.5} \qquad\qquad (1.1)$$

where H_C is the coercivity, D is the critical diameter, g and h are the constant.

Below the critical diameter, the coercivity of the material becomes zero because thermal energy is sufficient to overcome the interaction energy and randomize the spin magnetic moment of the particle causing superparamagnetism. The phenomenon of superparamagnetism occurs when each particle behaves like a single domain or particles have single giant magnetic moment instead of individual magnetic moment [51].

Superparamagnetism means particles have zero value of retentivity and coercivity and only saturation magnetization exists. The hysteresis loops of different types of magnetism are exhibited by the materials is shown in figure 1.6 [52].
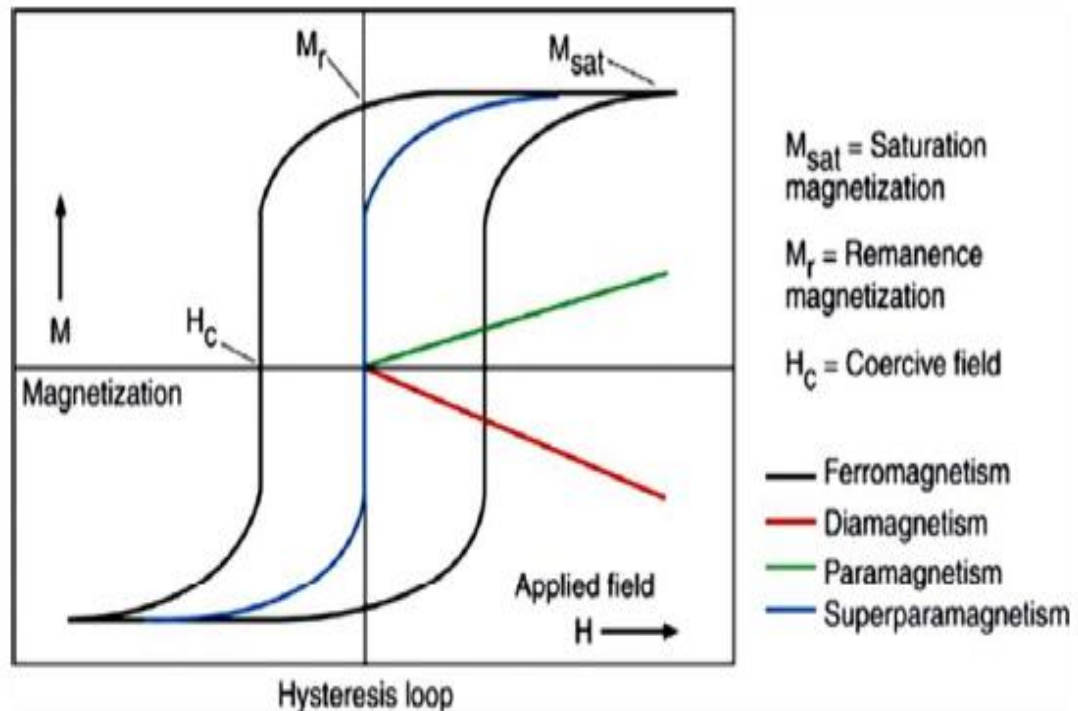
Figure 1.6: Hysteresis loops of different types of magnetism [52].

The coercivity or magnetic properties of magnetic nanoparticles also depend on the magnetic anisotropy energy i.e. (i) Magneto crystalline anisotropy energy, (ii) Shape anisotropy, (iii) Magneto elastic anisotropy and (iv) Induced anisotropy. The magneto crystalline anisotropy energy has the main contribution for the magnetic properties of spinel ferrites nanoparticles. Magneto crystalline anisotropy energy is the energy which is required to rotate the magnetization or magnetic moment from easy axis to hard axis. The shape of the hysteresis loop, value of retentivity and coercivity were also strongly affected by magneto crystalline anisotropy energy. The magneto crystalline anisotropy energy does not depend on the shape and size of the nanoparticles in spinel ferrites nanoparticles. It is the intrinsic property of the ferrimagnetic materials that depends only on the spin-orbit coupling of atoms in the materials lattice. In spinel ferrite nanoparticles, coercivity mainly depends on magneto crystalline anisotropy energy of the ions in different sites. Higher value of magneto crystalline anisotropy energy attributes to the high coercivity of the materials. The magnetization of spinel ferrite nanoparticles strongly depends on the distribution of cations in tetrahedral (A)

and octahedral (B) sites having different magnetic moment and super-exchange interaction between them.

The Curie temperature of the spinel ferrites nanoparticles also depend on super exchange interaction. Stronger the super exchange interaction, higher the value of Curie temperature. Spinel ferrites are good candidates for applications or commercial point of view because of their significant properties. The unique properties of spinel ferrites such as high magnetic permeability, high thermal stability, high electrical resistivity, high electrolytic activity, low magnetic losses and resistance to corrosion make it promising candidate in electronic and magnetic devices applications [53-54]. The chemical, structural, electrical and magnetic properties of spinel type ferrite nanoparticles also depend on distribution of cations in different lattices having different ionic radii, their composition and synthesis method [55].

Among the different spinel ferrites, Ni-Zn ferrites are the soft magnetic material and very important from scientific point of view. Ni-Zn ferrite nanoparticles have significant properties like low coercivity, high Curie temperature, high resistivity, moderate saturation magnetization, good mechanical hardness and chemical stability [56]. Therefore, Ni-Zn ferrites are commonly used in antenna rods, recording heads, loading coils and microwave devices [57-60]. The power transformer cores and inductor cores in power applications are also being made by Ni-Zn ferries nanoparticles [61]. Ni-Zn ferrites have mixed spinel structure which contains two types of interstitial sites i.e., tetrahedral (A) and octahedral (B) sites. The eight tetrahedral (A) sites are occupied by Zn^{2+} and Fe^{3+} cations whereas the sixteen octahedral (B) sites are occupied by all Ni^{2+} and remaining Fe^{3+} cations [62]. The properties of ferrites nanoparticles are very sensitive to synthesis techniques, their microstructure and cations distribution [63-64]. Magnetic nanoparticles can be synthesized using physical and chemical methods. Various methods used to prepare the magnetic nanoparticles are presented in figure 1.7 [65]. Qian Chen *et. al.* reported $Ni_{0.5}Zn_{0.5}Fe_2O_4$ nanoparticles prepared by self-combustion technique [66]. It is found that the prepared nanoparticles by self-combustion technique have higher value of resistivity (10^{10} Ω cm) and low value of dielectric loss (0.008) making them suitable for high quality electrical applications. Poh Lin Leng *et. Al.* reported the synthesis and characterization of Ni-Zn ferrites nanoparticles by thermal treatment technique [67]. It is found that the structural and magnetic properties are changed with varying annealing temperature. The particle size found to increase from 7 to 25 nm and saturation magnetization increase from 11 emu/g to 26 emu/g as annealing temperature increases from 723 K to 875 K respectively.

Figure 1.7: Schematic diagram of magnetic nanoparticles prepared by different methods [65].

Properties of the Ni-Zn ferrites nanoparticles can be further improved by doping with different metals cations such as chromium, copper, manganese, cobalt, zinc, etc. for desired applications [68]. The improved properties of doped nickel zinc ferrite nanoparticles such as high resistivity and high permeability make it capable to use for radio frequency device applications [69]. B. Parvatheeswara Rao *et. al.* reported the microstructure and magnetic behavior of Ni-Zn-Co ferrites synthesized by classical ceramic method [70]. It is found that the increased value of saturation magnetization depends on cobalt doping, its concentration and cation distribution in sub lattices. M Siva Ram Prasad *et. al.* reported the structural and magnetic studies on $Ni_{0.5}Zn_{0.5}Cr_xFe_{2-x}O_4$ (x = 0 to 0.25 with 0.05 step variation) and synthesized by citrate gel auto combustion method [71]. Single phase spinel cubic structure was formed and particle size increase when samples were annealed at 1000^oC temperature (confirmed by XRD). The magnetic properties of prepared samples such as saturation magnetization measured from VSM decreases with Cr^{3+} doping. The decrease in magnetic

properties with doping are attributed to the reduction in A-B prominent interaction by virtue of low magnetic moment of substituted Cr^{3+} ions that displaces Fe^{3+} ions.

Hichem Huilia *et. al.* presented the effect of cobalt substitution on the structural, electrical and magnetic properties of nano crystalline $Co_xNi_{0.5-x}Zn_{0.5}Fe_2O_4$ at x = 0, 0.02 and 0.4 processed by the polyol process [72]. The prepared samples have been annealed at 700°C for 4 h. The average crystallite size of un-sintered samples is found in 2-4 nanometer range which enhanced to 28-41 nm range after sintering. The increase in crystallite size with annealing is due to diffusion of small crystallites. The room temperature resistivity of the prepared samples was found to increase with Co doping at a maximum value of x = 0.2. The prepared samples at x = 0.2 shows best magnetic behavior than other composition. The best properties of prepared samples were found at x = 0.2 which make it promising material for high frequency applications. Kaustav Bhattacharjee *et. al.* synthesized $Ni_{0.5}Zn_{0.5}Fe_2O_4$ nano powder by auto combustion method and annealed at different temperature to know the effect of temperature on the properties of the samples [73]. It was found from XRD that the crystallite size increases from 10.66 nm to 55.58 nm with increasing annealing temperature that is due to distribution of cations in different sub lattices which is effected by thermal energy. The room temperature magnetic behavior of prepared samples at different annealing temperature is measured from superconducting quantum interference device (SQUID). It has been found that the saturation magnetization of the samples increases with increasing annealing temperature because of increasing magnetic ordering inside the sub lattices of the crystallites with temperature.

Kandasamy Velmurugan *et. al.* has synthesized the $Ni_{1-x}Zn_xFe_2O_4$ at x = 0 to 1 (with step variation of 0.1) using co-precipitation method and characterized with respect to their structural and magnetic properties [74]. It was found that with increasing zinc doping concentration from x = 0 to 1, the crystallite size found to decrease from 8.95 nm to 6.92 nm as measured from XRD. Also the magnetic properties like saturation magnetization decreases with Zn doping and the prepared particles shows super paramagnetic behavior. Z. Beji *et. al.* has reported the effect of annealing temperature on the magnetic properties of $Ni_{1-x}Zn_xFe_2O_4$ (x = 0.2, 0.4) synthesized by polyol route [75]. The chemical analysis of prepared samples without annealing and with annealing at 400°C, 600°C and 800°C temperature has been done by energy dispersive X-ray spectroscopy (EDX) technique. It was confirmed that, prepared samples have all elements present according to composition and contains some carbon content that diminished at high annealing temperature. All the prepared samples have pure spinel

structure as confirmed by XRD. The crystallinity of prepared samples also increases as the annealing temperature increases. The particle size measurement of all prepared samples has been carried out by TEM. It was found that as prepared samples have particle sizes of about 6 nm and as the annealing temperature increase from 400°C to 800°C, the particles size reached to about 70 nm. The increase in particle size with increasing annealing temperature is attributed to crystal growth by heating. The magnetic properties of prepared samples were measured by SQUID technique. It was found that the saturation magnetization at room temperature of prepared samples increase with Zn doping and also with increasing temperature other than samples annealed at 400°C. The as prepared samples and samples annealed at 400°C shows superparamagnetic behavior. The increase in the value of saturation magnetization is attributed to distribution of Ni and Zn cations in both octahedral (B) and tetrahedral (A) sites and decreasing spin canting effect by virtue of increasing particle size with increasing temperature. The Blocking temperature of samples also increases with annealing temperature.

Na Chen *et. al.* has studied the effect of Yttrium ions doping or substitution on the microstructure and microwave absorbing properties of Ni-Zn ferrites powder [76]. In this study undoped and yttrium doped Ni-Zn ferrites nanoparticles were prepared by sol-gel method and calcined at 1173 K for one hour. XRD study revealed the formation of single phase spinel cubic structure of all prepared samples and crystallite size decrease with Yttrium doping. The magnetic properties such as saturation magnetization increased and coercivity decreased with Yttrium doping in Ni-Zn ferrites system. The microwave absorbing properties such as imaginary part of permittivity and permeability has increased with Yttrium doping as found from vector network analyzer (VNA) characterization. Finally, Yttrium doped Ni-Zn ferrites have good microwave absorbing properties than undoped Ni-Zn ferrites system by virtue of grain refinement which is caused by yttrium substitution in Ni-Zn ferrite system.

Xiang Shen *et. al.* has presented the magneto-dielectric properties of nanostructures $Ni_xZn_{1-x}Co_yFe_{2-y}O_4$ (x = 0.0, 0.4, 0.5, 0.6, y = 0.0, 0.01) processed by hydrothermal route [77]. It is found that Ni and Co doped ferrite samples have larger crystallite size than the undoped one. Also single phase spinel cubic structure of all prepared samples were confirmed from XRD analysis. The cobalt doped nickel zinc ferrite nanoparticles have high value of saturation magnetization than the other prepared samples measured by VSM. The prepared Co doped Ni-Zn ferrites nanoparticles has low value of dielectric constant that attributes to

usefulness of this material in microwave frequency range. The obtained high saturation magnetization, low dielectric constant and high permeability of Co doped nickel zinc ferrite nanoparticles make it promising candidates for microwave absorbing application in GHz range. G. S. V. R. K. Choudary $et.$ $al.$ reported the formation of $Ni_{0.65-x}Zn_{0.35}Co_xFe_2O_4$ (x = 0.0, 0.04, 0.08, 0.12, 0.16, 0.20, 0.24, 0.28) [78] by sol-gel method with single phase spinel cubic structure. The lattice constant of prepared samples has been found to increase with Co doping and is attributed to the larger ionic radii of Co ions that replace the smaller size Ni ions in octahedral sites causing lattice expansion. Also the saturation magnetization and coercivity increased with Co doping is due to high magnetic moment and high magneto crystalline anisotropy of Co ions replacing Ni ions. Impedance analysis results show that the initial permeability of prepared samples decreased with Co doping because of high magneto crystalline anisotropy of Co ions.

Sangeeta Thakur $et.$ $al.$ synthesized the indium substituted nickel zinc ferrites nanoparticles ($Ni_{0.58}Zn_{0.42}In_xFe_{2-x}O_4$ at x=0, 0.1, 0.2) using reverse micelle technique [79]. The samples prepared at x = 0 and 0.1 has single phase spinel cubic structure with partial formation of hematite phase with spinel phase at x = 0.2 as measured from XRD spectra. The crystallite size or particles size was found to increase with indium doping. The obtained values of saturation magnetization at x = 0, 0.1 and 0.2 are 22.29 emu/g, 39.38 emu/g and 24.85 emu/g respectively has been measured from SQUID at room temperature. The low value of saturation magnetization at x = 0 sample is attributed to surface spin canting effect. At x = 0.1, increased value of saturation magnetization is due to distribution of diamagnetic indium cations in tetrahedral sites which migrate the Fe^{3+} cations in octahedral sites and increase the total net magnetic moment. The decreased value of saturation magnetization at x = 0.2 is attributed to spin canting effect caused by hematite interaction with spinel phase. Sample for x = 0 shows super paramagnetic behavior or have no value of coercivity and retentivity. The super paramagnetic behavior of the sample gets changed to ferrimagnetic or ferromagnetic with indium doping or contains some value of coercivity and retentivity. Pure spinel ferrites and best ferrimagnetic magnetic behavior at room temperature of sample prepared at x = 0.1 is attributed to the usefulness of this material in magnetic storage device.

Samaila Bawa Waje $et.$ $al.$ has reported room temperature measurements of physical and magnetic characteristics of $Co_{0.4}Ni_{0.3}Zn_{0.3}Fe_2O_4$ polycrystalline material prepared using mechanically alloyed technique [80]. It was found that $Co_{0.4}Ni_{0.3}Zn_{0.3}Fe_2O_4$ nanoparticles prepared by taking Fe_2O_3, Co_3O_4, NiO and ZnO and milled using mechanical alloying for 12

h. The prepared sample was made in pallet form and sintered at different temperatures from 600^oC to 1000^oC. It was found that there is formation of spinel phase cubic structure of sintered samples and as the sintering temperature increases, the crystallinity of the prepared samples also increases. Permeability and permittivity values also increased with sintering because of grain growth. The obtained saturation magnetization of sintered samples is higher than that of un-sintered sample because of its low crystalline order. S. R. Shannigrahi *et. al.* reported the EMI shielding behavior of $(Ni_xR_{1-x})_{0.5}Zn_{0.5}Fe_2O_4$ composite thin film prepared by microwave sintering and melt blending approach (R = Mn, Co, Cu; x = 0, 0.5) [68]. It was found that Co doped Ni-Zn ferrite have high value of saturation magnetization and have high EMI shielding efficiency than other metals doped Ni-Zn ferrite system. In literature, Ni-Zn and doped Ni-Zn ferrites nanoparticles has been synthesized by many researcher using different method and these materials can be used in different applications because of their different properties.

In the present work, Ni-Zn ferrite was used as a basic material on account of its excellent properties and its applications in many fields. Among the different metals cations, Co^{2+} ions have been used as a dopant to enhance the properties of Ni-Zn ferrite nanoparticle. Co is a ferromagnetic material and has high magnetic moment, high permeability, high magneto crystalline anisotropy energy and high Curie temperature. Here in Ni-Zn ferrite system, Ni ions have been replaced by Co ions by doping to enhance the properties. The methods used for the preparation of un-doped and Co doped Ni-Zn ferrite is simple and cost effective. Sol-gel method has been used to prepare ferrite nanoparticle on the grounds of its exclusive advantages such as precursors materials dissolve at atomic or molecular level, low processing temperature, homogeneous reaction distribution, excellent composition control, cost effectiveness and better results over other complex methods. Further, non-aqueous method has also been developed to prepare the undoped and Co doped Ni-Zn ferrite nanoparticle. Because in non-aqueous method, nanoparticles can be prepared by using non-hydrated solvent, without using any complexing agent, without adjusting the pH, low temperature synthesis process and moreover very less time is required to prepare the nanoparticles. Table 1.3 shows the synthesis process feature highlights of sol-gel and non-aqueous method.

Table **1.3:** Synthesis process features of *sol-gel* and non-aqueous method.

Content used	*Sol-gel* Method	Non-Aqueous Method
Solvent	Hydrated	Non Hydrated
Complexing Agent used	Yes	No
pH Adjusted	Yes	No
Synthesis Temperature	high	Low
Synthesis Time	more	less

1.1.6 Objectives of the thesis

I. Synthesis, structural and magnetic studies of Co doped Ni-Zn ferrite nanoparticles.

II. Effect of annealing temperature on structural and magnetic properties of Co doped Ni-Zn ferrite nanoparticles.

III. Development of Co doped Ni-Zn ferrite nanoparticles by non-aqueous method and their structural and magnetic properties studies.

In order to analyze the synthesized ferrite nanoparticles, several characterization tools and techniques have been used to know the properties and discussed in the next chapters. Subsequently in coming chapters each and every objective will be presented and discussed in thoroughly.

1.1.7 Outline of thesis

Chapter 1. General introduction of nanotechnology along with history of ferrites and magnetism is described in this chapter. Classification of ferrites based on their magnetic properties and crystal structure were also discussed.

Chapter 2. Experimental techniques used for the preparation of doped and undoped Ni-Zn ferrites nanoparticles are described. This section also includes the characterization techniques that are used to know the structural and magnetic properties.

Chapter 3. This chapter describes the synthesis of undoped and Co doped Ni-Zn ferrites nanoparticles synthesized by sol-gel method annealed at low temperature. This chapter also includes measurement of structural, elemental and magnetic properties by XRD, FESEM, EDX and VSM. The effect of Co doping on the structural and magnetic properties of Ni-Zn ferrites nanoparticles was also discussed.

Chapter 4. In this chapter synthesis of undoped and Co doped Ni-Zn ferrites nanoparticles were also carried out by sol-gel technique and been annealed at high temperature. The effect of Co doping and high annealing temperature on the properties Ni-Zn ferrite system has been described by various techniques.

Chapter 5. This chapter includes synthesis, structural and magnetic studies of undoped and Co doped Ni-Zn ferrites synthesized by non-aqueous method. The comparisons of properties were also carried out for nanoparticles prepared by sol-gel and non-aqueous method.

Chapter 6. Finally, this chapter deals with the overall summary and conclusion of the work.

CHAPTER – 2

SYNTHESIS AND CHARACTERIZATION TECHNIQUES
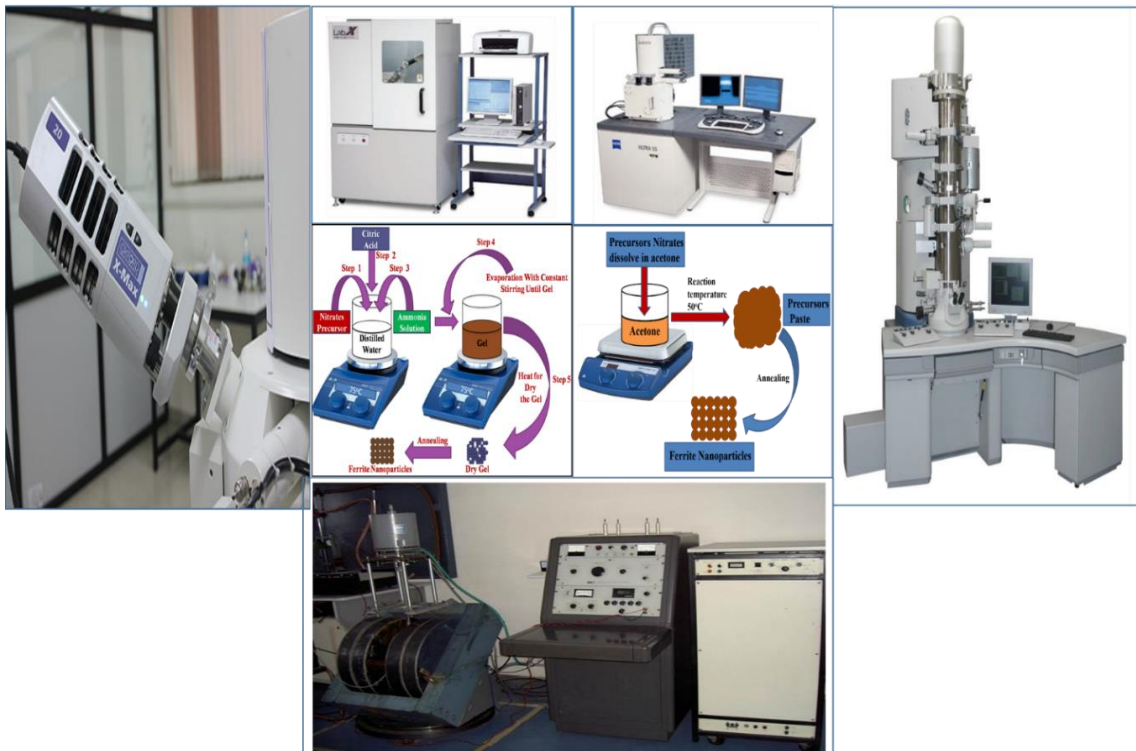
2.1 Overview

Materials scientist has made great efforts to the development of new and convenient methods for synthesis of ferrites nanoparticles. Number of physical and chemical methods has been used to prepare the ferrites nanoparticles. Auto combustion method [66], ceramic method [70], polyol method [72, 75], co-precipitation method [74], hydrothermal method [81-82, 77], *sol-gel* method [83, 76, 78], reverse micelle method [79], mechanically alloyed method [80] are some of the most commonly used techniques to prepare the ferrites nanoparticles. Among the different methods, *sol-gel* method is the most important method for preparing ferrites nanoparticles because of their important features such as precursors materials dissolve at atomic or molecular level, low temperature synthesis process, homogeneous reaction distribution, excellent composition control, high purity product formation, better size and morphological control, cost effectiveness and better results over other complex methods [84]. This chapter presents the detailed information on the subject of the synthesis and experimental techniques that is employed for the preparation of undoped and Co doped Ni-Zn ferrites nanoparticles. In this chapter *sol-gel* method for synthesis of undoped and Co doped Ni-Zn ferrites at different annealing temperature are being explained. Synthesis of undoped and Co doped Ni-Zn ferrites nanoparticles by new optimized non-aqueous methods has also been included in this chapter. Structural, morphological, elemental and magnetic properties of as prepared nanoparticles were studied by X-ray diffraction (XRD), Field emission scanning electron microscopy (FESEM), Energy dispersive X-ray spectroscopy (EDX), Transmission Electron Microscope (TEM), and Vibrating sample magnetometer (VSM).

2.2 Synthesis of $Ni_{0.6-x}Zn_{0.4}Co_xFe_2O_4$ nanoparticles by *sol-gel* method

Synthesis of $Ni_{0.6-x}Zn_{0.4}Co_xFe_2O_4$ nanoparticles at x = 0, 0.03, 0.033, 0.066, 0.09, 0.132, 0.264, 0.27 and 0.528 by *sol-gel* method and annealed at 700^oC and 1100^oC temperature.

2.2.1 Chemical required for synthesis of $Ni_{0.6-x}Zn_{0.4}Co_xFe_2O_4$ nanoparticles

I. The chemicals nickel nitrate hexahydrate (Ni $(NO_3)_2.6H_2O$) (Merck 99.9%), zinc nitrate hexahydrate (Zn $(NO_3)_2.6H_2O$) (Merck 99.9%), cobalt nitrate hexahydrate (Co $(NO_3)_2.6H_2O$) (Merck 99.9%), ferric nitrate nonahydrate (Fe $(NO_3)_3.9H_2O$) (Merck 99.9%) were used as precursor or raw materials to prepare ferrites nanoparticles.

II. Citric acid monohydrate $C_6H_8O_7.H_2O$ (Merck, 99.9%) was used as a complexing agent.

III. Aqueous ammonia (25%) AR-grade was taken as pH controller (Merck, 99.9%).

2.2.2 Procedure for preparation of $Ni_{0.6-x}Zn_{0.4}Co_xFe_2O_4$ nanoparticles

The aqueous solution of metal nitrates has been prepared by dissolving the stoichiometric amounts of nickel nitrate hexahydrate (Ni $(NO_3)_2.6H_2O$), zinc nitrate hexahydrate (Zn $(NO_3)_2.6H_2O$), cobalt nitrate hexahydrate (Co $(NO_3)_2.6H2O$) and ferric nitrate nonahydrate (Fe $(NO_3)_3.9H_2O$) in distilled water under magnetic stirring for 30 minute. The aqueous solution of citric acid monohydrate was then added in the above solution with a molar ratio of nitrates to citric acid 1:3. Aqueous ammonia solution was added drop wise in solution to adjust the required pH = 7. The solution was heated at $75^oC\pm5^oC$ with stirring continuously for several hours until the solution changed into gel. The gel was dried at $110^0C\pm5^oC$ for 24 hours in an oven. The obtained product was further annealed at 700^0C and 1100^oC for five hours to form desired $Ni_{0.6-x}Zn_{0.4}Co_xFe_2O_4$ nanoparticles. The schematic diagram of *sol-gel* method is shown in figure 2.1. The chemical reaction of nanoparticles prepared by *sol-gel* method is given below:

$$(0.6-x)Ni(NO_3)_2.6H_2O+(0.4)Zn(NO_3)_2.6H_2O+(x)Co(NO_3)_2.6H_2O+2Fe(NO_3)_3.9H_2O+$$
$$9C_6H_8O_7.H_2O+ NH_3 \xrightarrow{\Delta} Ni_{0.6-x}Zn_{0.4}Co_xFe_2O_4+4N_2\uparrow+54CO_2\uparrow+ 49H_2\uparrow+ 8H_2O$$
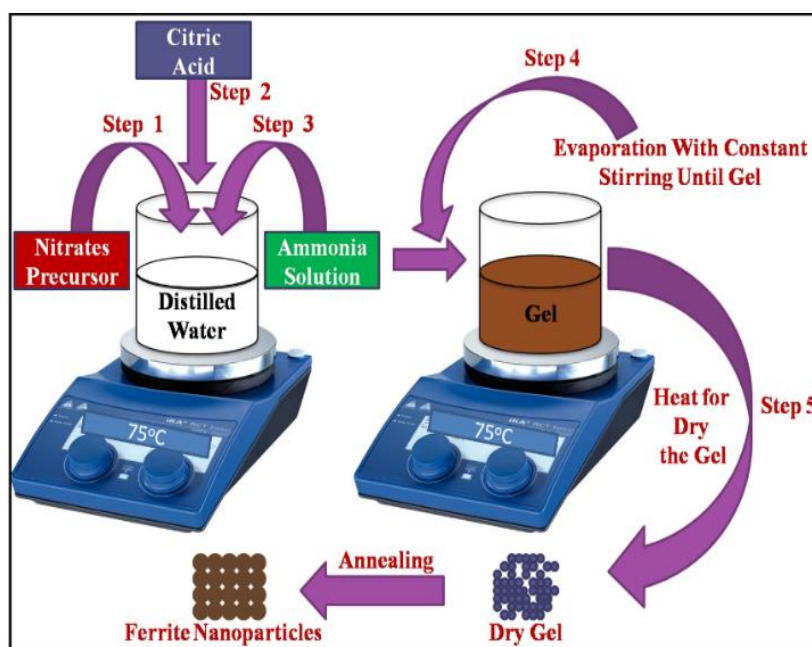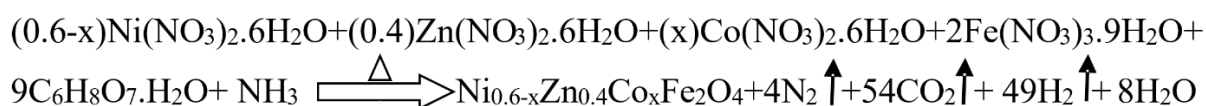
Figure 2.1: Schematic diagram of *sol-gel* method.

The various steps included in *sol-gel* process for the formation of nanoparticles are shown in figure 2.2. The two main reaction processes involved in *sol-gel* process are hydrolysis and condensation.
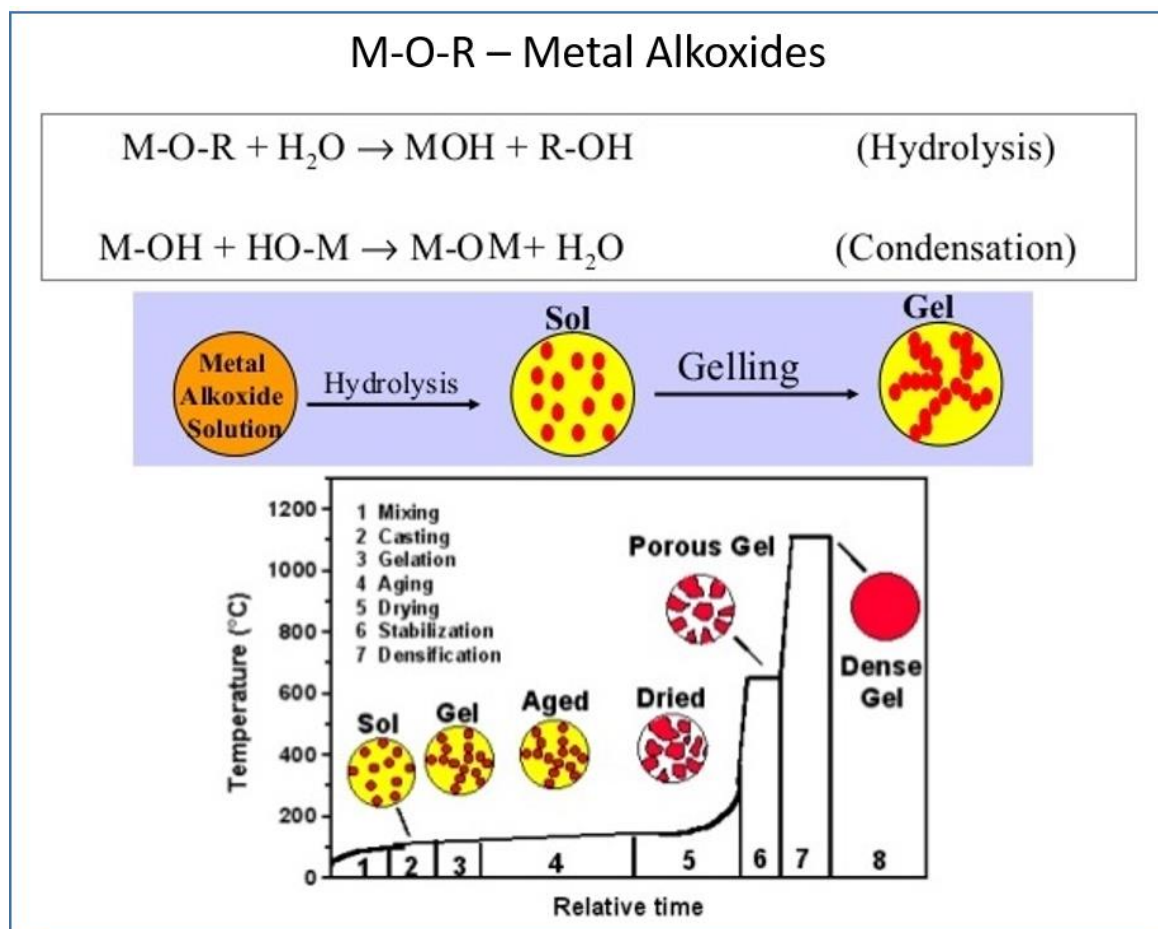
Figure 2.2: Steps included in *sol-gel* process.
(http://www.slideshare.net/tango67/nanomateriales-17839251).

In *sol-gel* method, sol is a dispersion or suspension of solid particles in liquid whereas gel is a continuous 3 D network of solid particles in liquid or gel in a state by which liquid and solid are dispersed in each other. In this process molecular precursors are dissolved in solvent to form sol or colloidal suspension and then 3D liquid filled solid network formed by linkage of colloidal nanoparticles with one another. The formation of gel from sol is possible by virtue of changing the pH of the reaction solution. The gel is dried through evaporation process which creates high density xerogel by collapsing of gel network. Further, high density xerogel is heated at high temperature to remove organic or inorganic component and for the formation of nanoparticles. The reaction mechanism of sol gel method is shown in figure 2.3. Figure 2.3 (a) shows the synthesis steps of sol gel method and (b) shows the reaction mechanism that are (i) hydrolysis of precursor and condensation, (ii) gelation and (iii) calcination or drying [85].
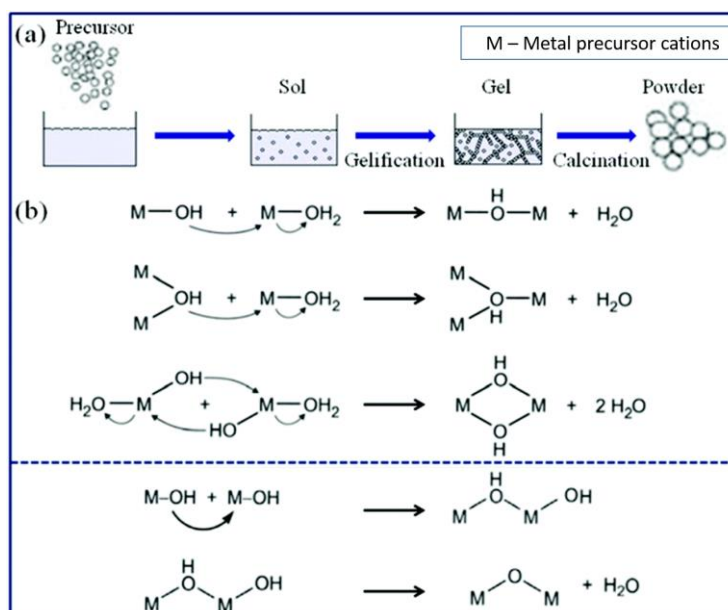
Figure 2.3: (a) the synthesis steps of sol gel method and (b) reaction mechanism of
sol-gel process [85].

2.3 Synthesis of $Ni_{0.6-x}Zn_{0.4}Co_xFe_2O_4$ nanoparticles by non-aqueous method

Synthesis of $Ni_{0.6-x}Zn_{0.4}Co_xFe_2O_4$ nanoparticles at x = 0, 0.033, 0.066, 0.132, 0.264 and 0.528 by non-aqueous method and then samples were annealed at 1100^oC temperature.

2.3.1 Chemical required for synthesis of $Ni_{0.6-x}Zn_{0.4}Co_xFe_2O_4$ nanoparticles

The chemicals nickel nitrate hexahydrate (Ni $(NO_3)_2.6H_2O$) (Merck 99.9%), zinc nitrate hexahydrate (Zn $(NO_3)_2.6H_2O$) (Merck 99.9%), cobalt nitrate hexahydrate (Co $(NO_3)_2.6H_2O$) (Merck 99.9%) and ferric nitrate nonahydrate (Fe $(NO_3)_{3.}9H_2O$) (Merck 99.9%) were also used as precursor materials. Acetone was used as a solvent to prepare ferrite nanoparticles.

2.3.2 Procedure for preparation of $Ni_{0.6-x}Zn_{0.4}Co_xFe_2O_4$ nanoparticles

The stoichiometric amounts of nickel nitrate hexahydrate (Ni $(NO_3)_2.6H_2O$), zinc nitrate hexahydrate (Zn $(NO_3)_2.6H_2O$), cobalt nitrate hexahydrate (Co $((NO_3)_2.6H_2O$) and ferric nitrate nonahydrate (Fe $(NO_3)_3.9H_2O$) has been dissolved in acetone under magnetic stirring for 30 minutes at room temperature to make a homogenous solution. After that the reaction was performed at $50^oC\pm5^oC$ with continuous stirring until the solution gets changed into paste. Further, prepared samples were annealed at 1100^oC for five hours and desired $Ni_{0.6-x}Zn_{0.4}Co_xFe_2O_4$ nanoparticles has been formed. The schematic diagram of non-aqueous method is shown in figure 2.4. The chemical reaction of non-aqueous method is given below:

$$(0.6\text{-}x)Ni(NO_3)_2.6H_2O + (0.4)Zn(NO_3)_2.6H_2O + (x)Co(NO_3)_2.6H_2O + 2Fe(NO_3)_3.9H_2O + (CH_3)_2CO$$
$$\underset{\Delta}{\Rightarrow} Ni_{0.6\text{-}x}Zn_{0.4}Co_xFe_2O_4 + 2N_2\uparrow + CO_2\uparrow + H_2\uparrow + 6O_2\uparrow + 23H_2O + 4NO_2 + 2CH_3OH$$
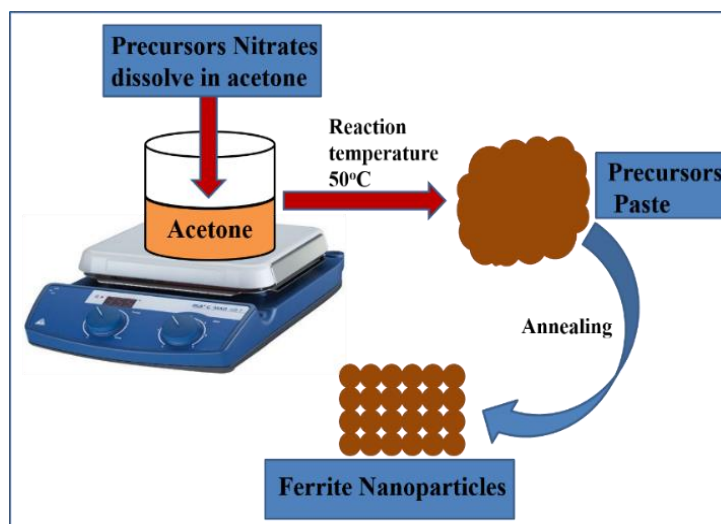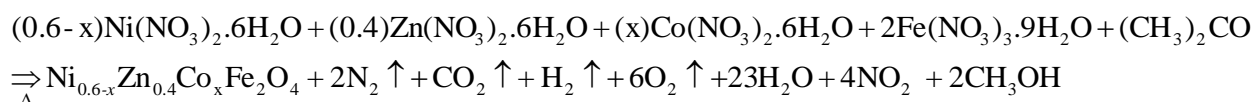
Figure 2.4: Schematic diagram of non-aqueous method.

2.4 Characterization Techniques

2.4.1 X-ray diffraction

XRD is the most important and widely used characterization technique in materials science. XRD is a versatile and nondestructive technique which used for the qualitative and quantitative analysis of the materials. XRD works on the principle of constructive interference of monochromatic X-ray when X-ray falls on crystallite sample. Powder XRD is a long range order technique, which provide the information about structural properties. The measurement of size, shape, internal stress, identification of unknown materials, crystallinity of the materials and average spacing can also be examined by XRD. It also provides the information regarding orientation of planes and impurity phase present in crystal lattice. X-rays are produced by means of bombarding the target (usually Cu or Mo) with a beam of electrons which emitted from a filament. XRD instrument require an X-ray source, specimen or sample and detector. When X-ray falls on sample or specimen, it gets diffracted in possible direction and satisfies the Bragg's conditions ($2d\sin\theta = n\lambda$). Bragg's law relates the diffraction angle and lattice spacing of the crystallite to the wavelength of electromagnetic radiation. The diffracted rays are recorded by movable detector as a function 2θ. The recorded XRD spectra provide useful information regarding the samples. The ray diagram of XRD is shown in figure 2.5 [86].
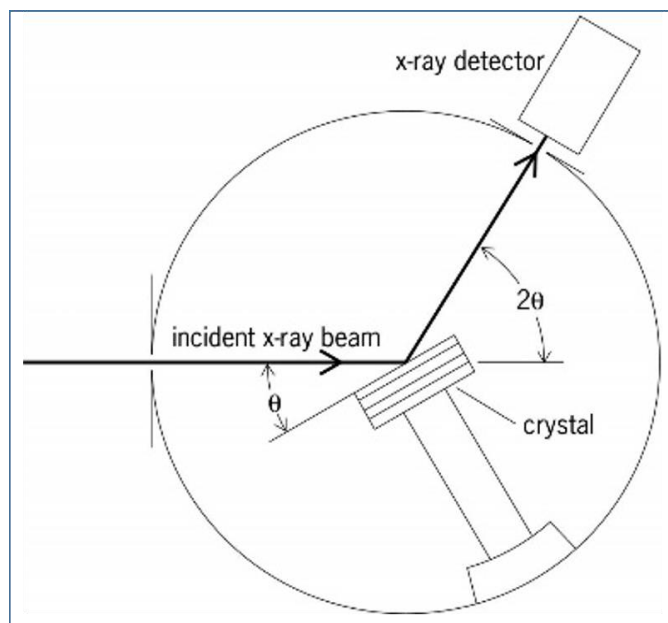
Figure 2.5: Ray diagram of XRD.

In the present work, the prepared samples were characterized by XRD Shimadzu-6000 to know the structural properties such as phase identification, measurement of crystallite size and other structural parameters. Figure 2.6 shows the photograph of X-ray diffractometer Shimadzu-6000. The samples were scanned in the range 15° to 65° in 2°/min with step size 0.02^o.

Figure 2.6: Photograph of X-ray diffractometer Shimadzu-6000 model.

2.4.2 Field emission scanning electron microscopy (FESEM)

FESEM is a high-resolution microscope that works with electron instead of light and used to study the topology, morphology and composition of the material. Image produced from FESEM have high spatial resolution (3-6 times better) and high magnification (10 X to 300000 X) than scanning electron microscope (SEM). In FESEM, electron beam generated from cathode through field emission and provides narrower beam at low and high electron energy which results to improve the spatial resolution and minimize the sample damage. In FESEM, electrons are liberated through field emission from source and accelerated in a high electric field gradient. These primary electrons are focused and deflected by electronic lenses in high vacuum to produce narrow beam. When narrow electron beam bombards on the samples or specimens, secondary electrons are emitted from the specimen are recorded by detector that produces the electrical signals. These electrical signals are then amplified and transformed to image that provide the information regarding the samples. The ray diagram of FESEM is shown in figure 2.7.
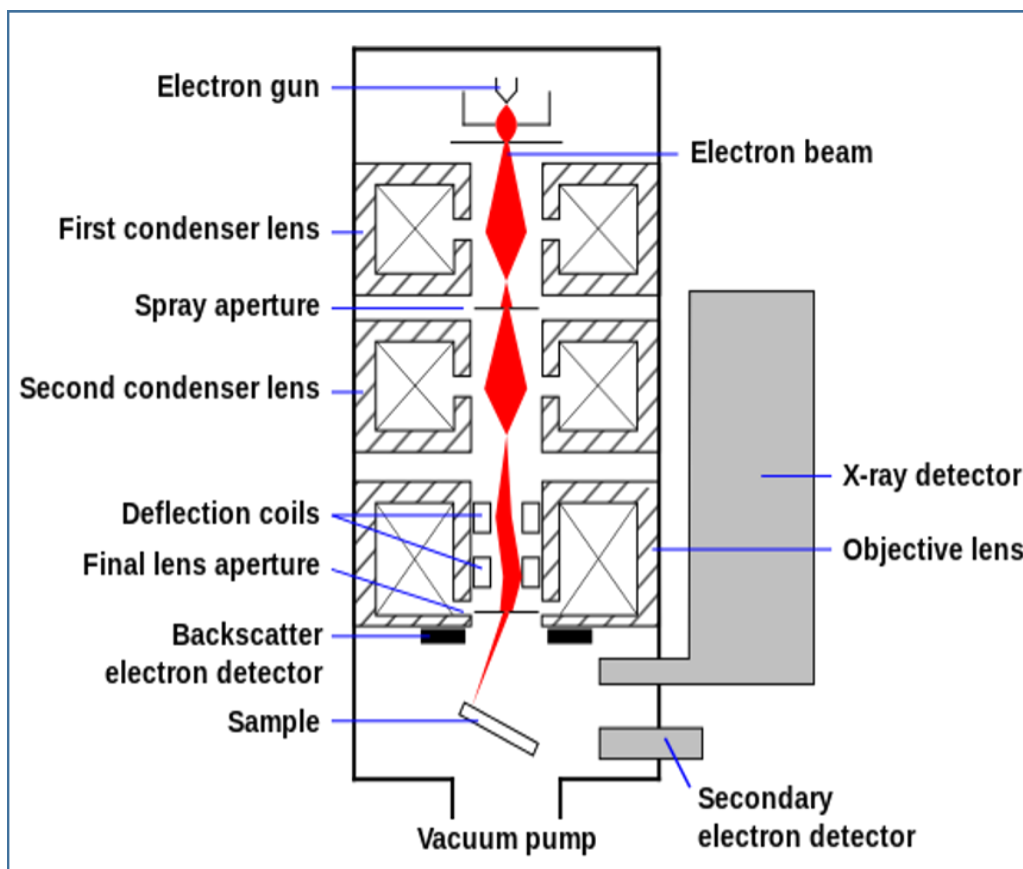
Figure 2.7: FESEM ray diagram.
(https://en.wikipedia.org/wiki/Scanning_electron_microscope)

Presently the prepared samples have been employed to Carl Zeiss Modal No-Ultra Plus-55 FESEM. The photograph of Carl Zeiss Modal No-Ultra Plus-55 FESEM is shown in figure 2.8.

Figure 2.8: Photograph of Carl Zeiss Modal No-Ultra Plus-55 FESEM.

2.4.3   Energy dispersive X-ray spectroscopy (EDX)

Energy Dispersive X-ray Spectroscopy is a qualitative and quantitative technique used for the elemental analysis or provides information about the chemical composition of a sample containing elements, whose atomic number greater than 3. In Energy Dispersive X-ray Spectroscopy, when high energy beam of electrons incident on the samples, X-ray is emitted by the samples. The schematic ray diagram of EDX is shown in figure 2.9.
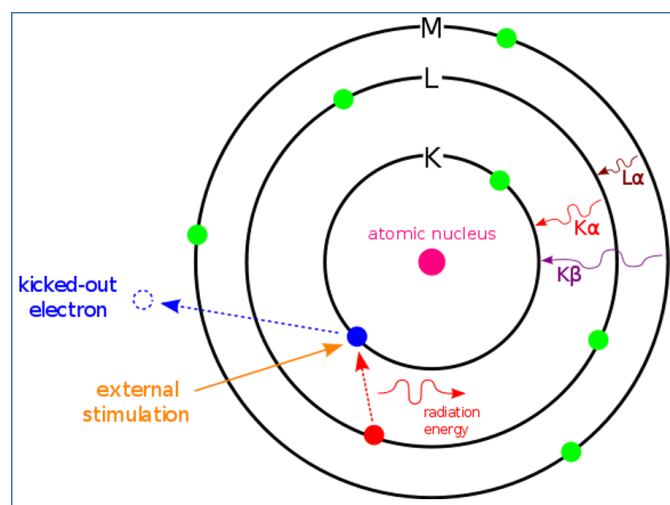
Figure 2.9: Schematic ray diagram of EDX.

(https://commons.wikimedia.org/wiki/File:EDX-scheme.svg.)

The nature of emitted X-rays from the sample provides the information about the elements present in the samples and also the information about amount of content of element in the samples. The energy of emitted X-rays is energy characteristic difference of two shells and atomic structure of the elements that is present in the samples which gives the information about the elemental composition of the materials. Here, prepared samples have been employed to oxford instruments EDX to know the elemental composition. The photograph of oxford instruments EDX is shown in figure 2.10.

Figure 2.10: Photograph of oxford instruments EDX.

2.4.4 Transmission electron microscopy (TEM)

Transmission electron microscope is very important tool to study the microstructure of the materials with high magnification $3x10^5$ to 10^6 and high resolution about 1nm. TEM work on the principle of transmission of electrons and obtained images is of many orders of magnitude better than that obtained from a light microscope. In transmission electron microscopy, a beam of electrons of very small wavelength emitted from tungsten filament source. When this beam of electrons incident or falls to an ultra-thin specimen, it gets transmitted. The transmitted electron beam is focused on phosphor screen or charge coupled device (CCD) camera by objective lens to form an image. The darker area of image represents the area of sample by which fewer electrons were transmitted and lighter area of the image represent those areas in which more electrons were transmitted through the sample. The ray diagram of TEM is shown in figure 2.11. The TEM resolving power is directly proportional to the wavelength of the irradiation which is used to form an image and provide information about the crystal structure and size. The resolution of microscope is increased, when accelerating voltage of the electron beam is increased. Presently, TEM model Hitachi H-7500 has been

used to characterize the samples. The photograph of TEM model Hitachi H-7500 is show in figure 2.12.
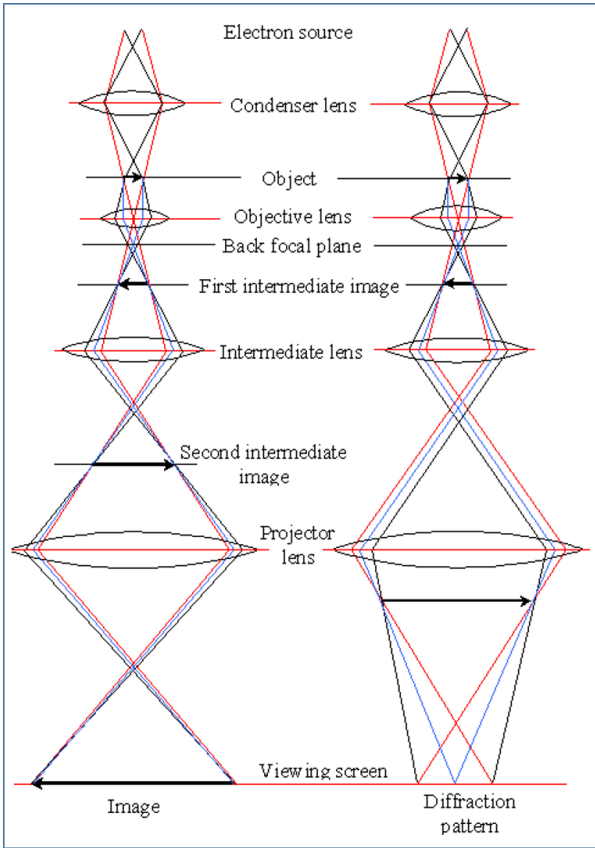
Figure 2.11: TEM ray diagram. (http://labs.mete.metu.edu.tr/tem/TEMtext/TEMtext.html).

Figure 2.12: Photograph of TEM model Hitachi H-7500.

2.4.5 Vibrating sample magnetometer (VSM)

The magnetic properties of prepared samples have been investigated with the help of vibrating sample magnetometer model PAR-155 at room temperature in -10 KOe to + 10 KOe range of magnetic field. The photograph of vibrating sample magnetometer model PAR-155 is shown in figure 2.13. Vibrating Sample Magnetometer works on the principle of Faraday laws of induction i.e. varying magnetic field will cause an induce electric field. When sample is placed in uniform magnetic field in VSM, it is physically vibrated and induced changes in the magnetic field are detected by search coil. The induce change in field by virtue of movement of sample in up and down direction is measured as a function of time by pick up coils in term of electric field. The measured electric field provides the information regarding changing magnetic field and proportional to the magnetization of the samples. Higher the magnetization of the materials, larger the induced current in the material and that can be amplified which gives the information about the magnetic properties such as saturation magnetization, retentivity and coercivity of the materials. The schematic diagram of VSM and their component is shown in figure 2.14. The behavior and magnetic properties of different materials are estimated by plotting the graph between saturation magnetization (M_S) versus applied field (H).

Figure 2.13: Photograph of vibrating sample magnetometer model PAR-155.
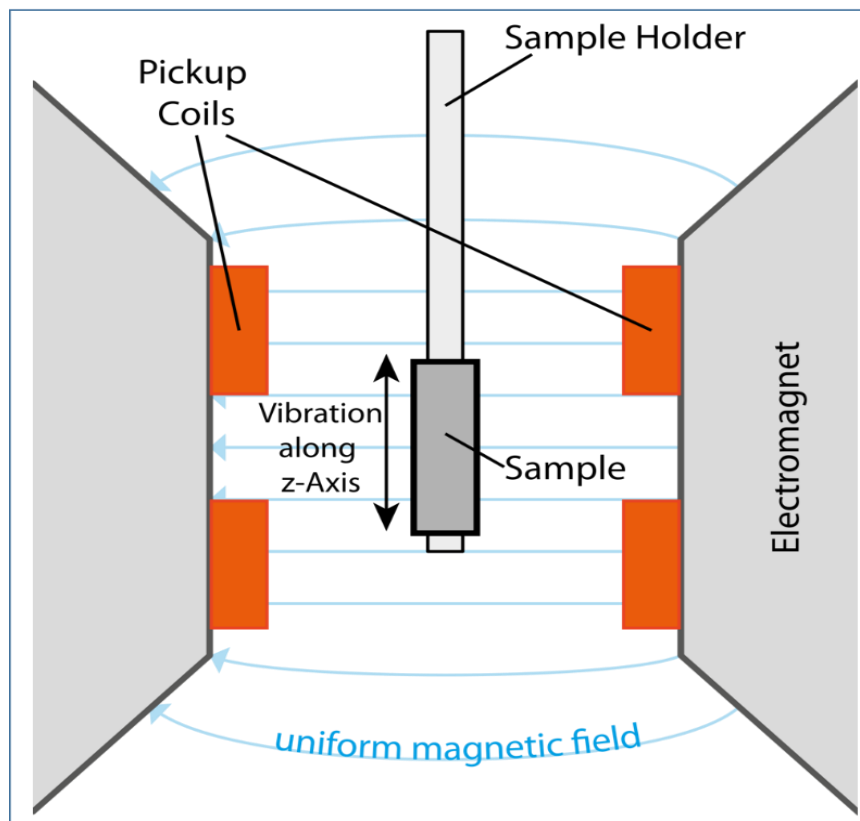
Figure 2.14: Schematic diagram of VSM and their components.

(http://en.wikipedia.org/wiki/Vibrating_sample_magnetometer)

2.5 Formulas

1. The crystallite size (***D***) of the nanoparticles have been calculated using Scherrer's formula (eqn.2.1)

$$D = K\lambda/\beta \cos\theta \qquad (2.1)$$

where *K* is Scherer's constant having value 0.9 in case of cubic system. $\lambda = 1.54$ Å is the wavelength of X-rays used, *β* is the full width at half maximum of the XRD peak and *θ* is the Bragg's angle.

2. The lattice parameters such as lattice constant (***a***) (eqn.2.2) and d-spacing (***d***) (eqn.2.3) of prepared nanoparticles were calculated using the formula

$$2\,d\,\sin\theta = n\,\lambda \qquad (2.2)$$

$$a = d\,(h^2 + k^2 + l^2)^{1/2} \qquad (2.3)$$

where *h*, *k*, and *l* are miller indices of the plane.

3. The strain (***ε***) of nanoparticles has been estimated using Stocks-Wilson relation (eqn.2.4)

$$\varepsilon = \beta/4\tan\theta \qquad (2.4)$$

4. The crystallite size (**W-H D**) and types of strain present in nanoparticles has been calculated using Williamson-Hall (W-H) method. The width of individual reflections in W-H method has been expressed by relation (eqn.2.5)

$$\beta \cos\theta = K\lambda/D + 4\varepsilon \sin\theta \qquad (2.5)$$

where β is the FWHM of peaks, D is the crystallite size from W-H plot, λ is the wavelength of Cu Kα radiation and ε is the types of strain.

5. Theoretical lattice constant (a_{th}) has been calculated from cation distribution using formula (eqn.2.6)

$$a_{th} = 8/3\sqrt{3}[(r_A + R_o) + \sqrt{3}(r_B + R_o)] \qquad (2.6)$$

by taking the mean ionic radii of both sites A and B (cations radii) from cations distribution. r_A and r_B are the mean ionic radii of site tetrahedral (A) and octahedral (B) site respectively and has been calculated from proposed cation distribution where R_o is the ionic radii of oxygen i. e. 1.32 Å.

6. The value of oxygen positional parameter (u) has been calculated using following equation (eqn.2.7)

$$u = 1/a_{th}(r_A + R_o) + 1/4 \qquad (2.7)$$

where a_{th} is the theoretical lattice constant.

7. The inversion parameter (δ) or deviation from ideal oxygen positional parameter (u) was calculated using relation (eqn.2.8)

$$\delta = u - u_{ideal} \qquad (2.8)$$

where u_{ideal} is the ideal oxygen positional parameters 0.375 Å.

8. The magneto crystalline anisotropy energy constant (**K**) of prepared nanoparticles has been calculated using formula (eqn.2.9)

$$H_c = 2K/M_s \qquad (2.9)$$

where H_c and M_s are the coercivity and saturation magnetization of the samples respectively.

9. The experimental magnetic moment (**M$_\mu$**) of all prepared samples was calculated using formula (eqn.2.10)

$$M_\mu = (M_w \times M_s)/5585 \qquad (2.10)$$

where M_w is the molecular weight of the samples and M_s is the saturation magnetization of prepared nanoparticles.

10. The theoretical total magnetic moments (N_μ) per formula unit cell of prepared samples are also calculated from Neel's two sub lattices model of ferrimagnetism using equation (eqn.2.11)

$$N_\mu = M\,(B) - M\,(A) \tag{2.11}$$

by taking magnetic moment of cations, where *M(B)* and *M(A)* are the sub lattice moments of B and A sites respectively.

11. The interatomic distance between cation-cations (*b-f*) (eqn. 2.12 - eqn.2.16) and cation-anion (*p-s*) (eqn.2.17 – eqn.2.20) has been calculated using the following equations

Cation-cation distances

$$b = a/4\,(2)^{1/2} \tag{2.12}$$
$$c = a/8\,(11)^{1/2} \tag{2.13}$$

$$d = a/4\,(3)^{1/2} \tag{2.14}$$
$$e = 3a/8\,(3)^{1/2} \tag{2.15}$$

$$f = a/4\,(6)^{1/2} \tag{2.16}$$

Cation-anion distances

$$p = a\,(5/8 - u) \tag{2.17}$$
$$q = a\,(u - 1/4)\,(3)^{1/2} \tag{2.18}$$

$$r = a\,(u - 1/4)\,(11)^{1/2} \tag{2.19}$$
$$s = a\,(1/3u + 1/8)\,(3)^{1/2} \tag{2.20}$$

where *a* is the experimental lattice constant and *u* is the oxygen positional parameter.

12. The bond angles $\theta_1, \theta_2, \theta_3, \theta_4$ and θ_5 were calculated using the following equation (eqn.2.21 – eqn.2.25)

$$\theta_1 = \cos^{-1}[p^2 + q^2 - c^2/2pq] \tag{2.21}$$
$$\theta_2 = \cos^{-1}[p^2 + r^2 - e^2/2pr] \tag{2.22}$$

$$\theta_3 = \cos^{-1}[2p^2 - b^2/2p^2] \tag{2.23}$$
$$\theta_4 = \cos^{-1}[p^2 + s^2 - f^2/2ps] \tag{2.24}$$

$$\theta_5 = \cos^{-1}[r^2 + q^2 - d^2/2rq] \tag{2.25}$$
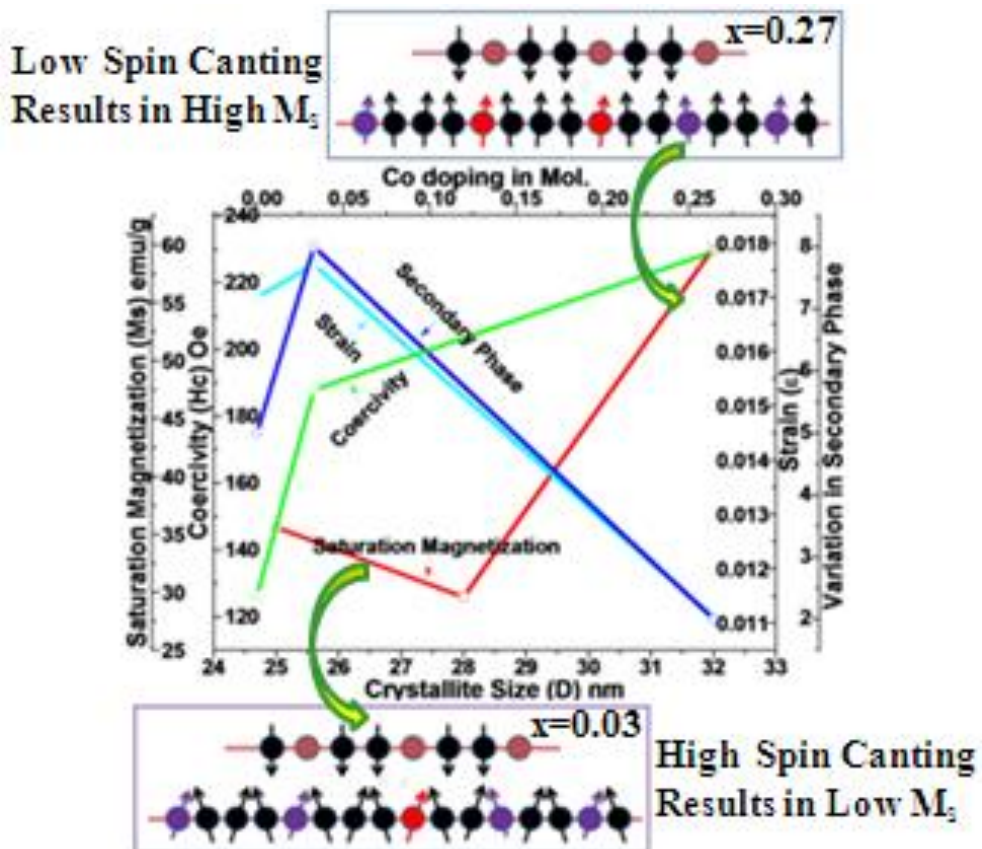
3.1 Introduction

The last decade has been marked for the spinel ferrites as these materials become promising candidates for emerging research on account of their good magnetic properties and high resistivity over a wide range of frequencies (few hundred Hz to several GHz). Spinel ferrites are technologically very important materials because of their magnetic, electrical and optical properties having a general formula MFe_2O_4 (where M is divalent metal cations such as Fe^{2+}, Co^{2+}, Ni^{2+}, Zn^{2+}, etc.). These ferrites have been widely used in electronic and magnetic devices because of their unique properties like high magnetic permeability, low magnetic losses, high thermal stability, high electrical resistivity, electrolytic activity and resistance to corrosion [53-54]. The chemical, structural, electrical and magnetic properties of spinel ferrites are strongly influenced by their compositions, synthesis methods and cations substitutions [55]. Now- a- days, soft ferrimagnetic Ni-Zn ferrites are the subject of intense research because they possess high resistivity, moderate saturation magnetization, low coercivity, high Curie temperature, good mechanical hardness and chemical stability [56]. Owing to their excellent properties, Ni-Zn ferrites are promising magnetic materials used in many applications such as antenna rods, recording heads, loading coils, core materials for power applications, microwave devices, etc. [57-60]. The magnetic properties of Ni-Zn ferrites can be enhanced by doping of various metals such as chromium, copper, manganese, cobalt, zinc, etc. [68]. Doped Ni-Zn ferrites possess high resistivity and high permeability and can be used in radio-frequency (RF) electronic device applications [69]. Co doped Ni-Zn ferrites are much approved material for electromagnetic interference (EMI) shielding applications.

B. P. Rao et. al. [70] reported the Co dependent magnetic behavior of $Ni_{0.35}Zn_{0.65-x}Co_xFe_2O_4$ (x = 0 to 0.25) synthesized using a conventional ceramic technique. S. R. Shannigrahi et. al. [68] described the EMI shielding nature of $(Ni_xR_{1-x})_{0.5}Zn_{0.5}Fe_2O_4$ composite thin film prepared by microwave sintering and melt blending approach (R = Mn, Co, Cu; x = 0, 0.5). It has been found that, among the different dopants, Co doped ferrites shows the best saturation magnetization and high EMI shielding effectiveness value. X. Shen et. al. [87] also studied the microwave absorbing properties of $(Ni_xZn_{1-x}) Co_yFe_{2-y}O_4$ (x = 0.0, 0.4, 0.5, 0.6; y = 0.0, 0.01) synthesized using a hydrothermal route and showed an increased saturation magnetization as a function of Co doping. J. S. Ghodake et. al. [88] has reported the permeability and magnetic behavior of Co substituted Ni-Zn ferrites processed using an oxalate precursor method. S. L. Pereira et. al. [89] investigated the modified magnetic

behavior of Co substituted Ni-Zn ferrite synthesized using a hydrothermal process. L.-Z. Li et. al. [90] studied the influence of Cu and Co substitution on the properties of Ni-Zn ferrite thin films synthesized using a *sol-gel* method. The soft magnetic materials are used as EMI shielding materials having high value of saturation magnetization and low value of coercivity. In this chapter, $Ni_{0.6-x}Zn_{0.4}Co_xFe_2O_4$ (x = 0, 0.03, 0.033, 0.066, 0.09, 0.132, 0.264, 0.27 and 0.528) has been synthesized using *sol-gel* method. Here Co has been introduced in Ni-Zn ferrite system to enhance the magnetic properties for EMI shielding application. The effect of cobalt doping and composition on structural, morphological, stoichiometry and magnetic properties has been studied on the basis of Co ion distribution and spin canting effect by X-ray diffraction (XRD), field emission scanning electron microscopy (FESEM), energy dispersive X-ray spectroscopy (EDX) and vibrating sample magnetometer (VSM) respectively.

3.2 Experimental detail

3.2.1 Synthesis of undoped and Co doped Ni-Zn ferrite nanoparticles

The ferrite nanoparticles have been synthesized by *sol-gel* method. The chemicals nickel nitrate hexahydrate (Ni $(NO_3)_2.6H_2O$), zinc nitrate hexahydrate (Zn $(NO_3)_2.6H_2O$), cobalt nitrate hexahydrate (Co $((NO_3)_2.6H_2O$), ferric nitrate nonahydrate (Fe $(NO_3)_3.9H_2O$) and citric acid monohydrate ($C_6H_8O_7$) were used as raw materials to prepare $Ni_{0.6-x}Zn_{0.4}Co_xFe_2O_4$ nanoparticles. The appropriate amounts of nitrates were dissolved in distilled water under magnetic stirring for 30 minutes then citric acid monohydrate was dissolved in it with a molar ratio of nitrates to citric acid is 1:3. Ammonia solution is added into the solution to adjust pH = 7 kept at 75^oC and stirred continuously until the solution changed into gel. The gel was dried at 110^oC for 24 hours annealed at 700^0C for five hours. Finally, desired ferrite nanoparticles have been obtained. Schematic diagram of sol-gel method is shown in figure 3.1. The chemical reaction of prepared nanoparticles is given below:

$$(0.6-x)Ni(NO_3)_2.6H_2O+(0.4)Zn(NO_3)_2.6H_2O+(x)Co(NO_3)_2.6H_2O+2Fe(NO_3)_3.9H_2O+$$
$$9C_6H_8O_7.H_2O+ NH_3 \xrightarrow{\Delta} Ni_{0.6-x}Zn_{0.4}Co_xFe_2O_4+4N_2\uparrow+54CO_2\uparrow+ 49H_2\uparrow+ 8H_2O$$
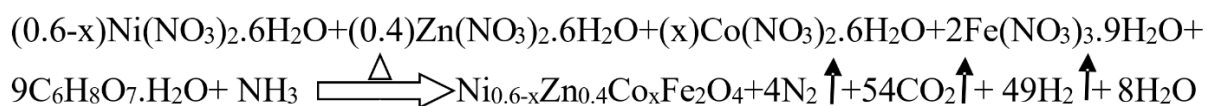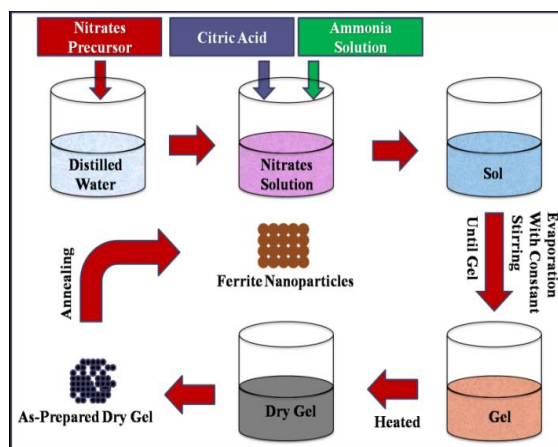
Figure 3.1: Schematic diagram of sol-gel method to synthesize $Ni_{0.6-x}Zn_{0.4}Co_xFe_2O_4$.

3.2.2 Characterization

Prepared $Ni_{0.6-x}Zn_{0.4}Co_xFe_2O_4$ samples were characterized by Shimadzu-6000 XRD using Cu-Kα ($\lambda = 1.546°A$) radiation for phase identification, measurement of crystallite size and other structural parameters. Morphology and elemental analysis of the prepared samples were observed by Carl Zeiss Modal No-Ultra Plus-55 FESEM and Oxford Instruments EDX respectively. The effect of Co doping on the magnetic properties of Ni-Zn ferrite has been examined by PAR-155 VSM in a magnetic field range from −10 KOe to +10 KOe.

3.3 Results and discussion

3.3.1 Structural analysis

Structural analysis of the samples of $Ni_{0.6-x}Zn_{0.4}Co_xFe_2O_4$ has been performed using the powder XRD patterns and are presented in figure 3.2. The XRD peaks (111), (022), (113), (222), (004), (224), (333) and (044) indicate that prepared samples at x = 0.264, 0.27 and 0.528 have single phase spinel cubic structure. The other prepared samples at x = 0, 0.03, 0.033, 0.066, 0.09 and 0.132 have partial formation of hematite secondary phase with spinel phase cubic structure. In the reported literature, it has been found that the Ni-Zn ferrite nanoparticles prepared using a sol-gel method and annealed below 700ºC have single-phase spinel structure [91-92]. The diffraction peaks have good agreement with standard JCPDS card no. 52-0277 and 89-0599 corresponding to spinel Ni-Zn ferrite and hematite secondary phase respectively. The peaks intensity of hematite secondary phase of $Ni_{0.6-x}Zn_{0.4}Co_xFe_2O_4$ nanoparticles is in the order $I_{x=0.033} > I_{x=0.066} > I_{x=0.03} > I_{x=0.09} > I_{x=0} > I_{x=0.132}$. The secondary phase present in the samples is due to unreactive component of hematite or naturally occurring hematite [93].
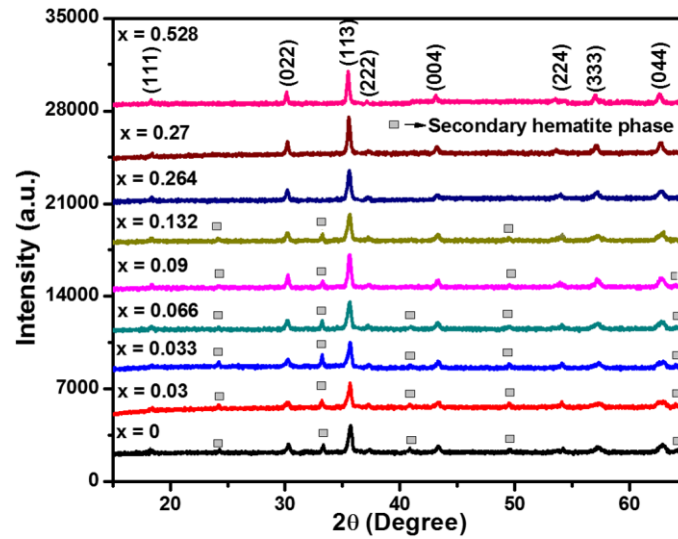
Figure 3.2: XRD Spectra of $Ni_{0.6-x}Zn_{0.4}Co_xFe_2O_4$ (x = 0, 0.03, 0.033, 0.066, 0.09, 0.132, 0.264, 0.27 and 0.528)

The average crystallite size of all prepared samples has been calculated from full-width at half-maxima (FWHM) of most prominent peak (113) of XRD patterns using Scherrer's formula (eqn.3.1) [94] and tabulated in table 3.1.

$$D = 0.9\ \lambda/\beta\ cos\theta \qquad\qquad (3.1)$$

where D is the average crystallite size, β is the FWHM of the peak intensity measured in radians, λ = 1.54 Å is the wavelength of X-ray and θ is Bragg's angle.

Ni-Zn ferrite has a mixed spinel structure. The octahedral (B) sites are occupied by Ni^{2+} and Fe^{3+} ions, whereas tetrahedral (A) sites are occupied by Zn^{2+} and remaining Fe^{3+} ions [62]. Co^{2+} ions have strong tendency to occupy B sites [77]. It is found that D value of prepared nanoparticles increases with cobalt doping from 25 to 34 nm. The D value obtained at x = 0.033 and 0.066 is smaller than that at x = 0.03. This variation in D with doping has been explained on the basis of cations distribution over tetrahedral (A) and octahedral (B) sites having different size and secondary hematite phase effect. The increase in D with Co doping might be due to the replacement of Ni^{2+} (ionic radii = 0.69 Å) ions by larger Co^{2+} (ionic radii = 0.745 Å) ions in sites B resulting to size enlargement of unit cells. Further as the doping concentration increases, more Co^{2+} cations replace the Ni^{2+} cations in sites B and enlarge more number of unit cells and reduces hematite secondary phase effect. The obtained smaller D value at x = 0.033 and 0.066 then at x = 0.03 possibly attributes to slight unit cell shrinkage due to prominent hematite secondary phase effect at these compositions as observed in XRD spectra. The D obtained at x = 0.27 is similar to that obtained at x = 0.264 and is because of minimum Co doping variation. The obtained larger value of D at x = 0.528

is due to high concentration of Co^{2+} ions in sites B that replaces the smaller size Ni^{2+} ions causing enlargement in unit cells. The effect of Co doping on structural parameters includes d-spacing (d) [95] and lattice constant (a) [96] which have been calculated and presented in table 3.1 using the following relations (eqn.3.2 and eqn.3.3):

$$2\, d\, sin\theta = n\, \lambda \qquad (3.2) \qquad\qquad a = d * \sqrt{h^2 + k^2 + l^2} \qquad (3.3)$$

Table 3.1. Crystallite size (D), d spacing (d), lattice constant (a) and strain (ε) calculated from the prominent peak (113) of XRD; crystallite size (**WH D**) calculated from Williamson-Hall plots.

x (Co doping)	D (nm)	d (Å)	a (Å)	ε	W-H D (nm)
0.000	25	2.5209	8.3608	0.00425	30
0.030	28	2.5195	8.3563	0.00432	33
0.033	26	2.5143	8.3389	0.00453	23
0.066	27	2.5161	8.3449	0.00442	22
0.090	29	2.5173	8.3489	0.00429	25
0.132	30	2.5191	8.3549	0.00412	23
0.264	31	2.5205	8.3595	0.00376	30
0.270	31	2.5209	8.3608	0.00369	32
0.528	34	2.5267	8.3801	0.00335	33

It has been noticed that in all prepared samples, the d as well as a value first decrease up to x = 0.033 and then increases with Co doping. The slight decrease in d and a value with Co doping is due to lattice shrinkage caused by segregation of Co^{2+} ions at grain boundaries and possibly by prominent secondary phase effect (as found in XRD spectra). The increased value of d and a with doping after x = 0.033, firstly attributes to lattice expansion caused by distribution of larger size Co^{2+} ions at sites B in place of smaller size Ni^{2+} ions and secondly, possibly decreasing the hematite phase effect. The strain (ε) present in nanoparticles has been calculated using Stocks-Wilson equation (eqn.3.4) [97] and presented in table 3.1.

$$\varepsilon = \beta/4tan\theta \qquad (3.4)$$

The calculated ε present in nanoparticles first increase up to x = 0.033 and then decreases with Co doping. The maximum ε present in nanoparticles at x = 0.033 is due to prominent hematite phase effect and decreasing values is due to increasing D as well as diminishing hematite phase. Finally, it is concluded that the ε present in the crystal structure is proportional to the concentration of the hematite secondary phase with primary phase. Also crystallite size (**W-H D**) and types of strain present in nanoparticles have been estimated from

Williamson-Hall (W-H) method and values of **W-H D** are inscribed in table 3.1. The width of individual reflections in W-H method has been expressed by eqn.3.5 [98].

$$\beta\,cos\theta = k\lambda/D + 4\,\varepsilon\,sin\theta \qquad (3.5)$$

where β is the FWHM of peaks, D is the crystallite size from W-H plot, λ is the wavelength of Cu Kα radiation and ε is the strain.

Figure 3.3 shows the W-H plots for $Ni_{0.6-x}Zn_{0.4}Co_xFe_2O_4$. The obtained values of **W-H D** from W-H plots are approximately equivalent to that calculated by Scherer's formula in nm range. The positive slope of the linear fit in W-H plots shows a tensile strain present in all prepared samples [98].
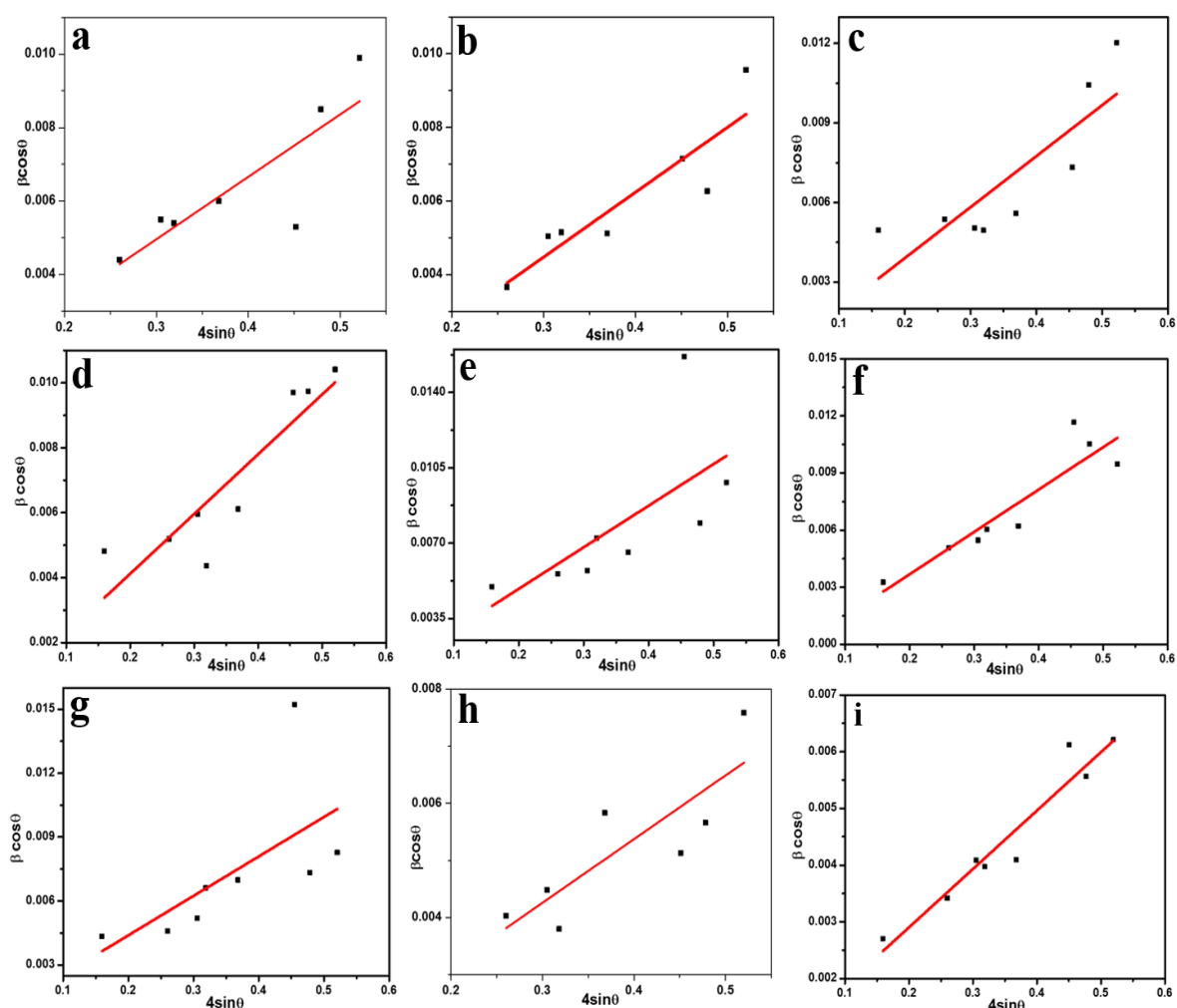
Figure 3.3: W-H plots of $Ni_{0.6-x}Zn_{0.4}Co_xFe_2O_4$ at (**a**) $x = 0$, (**b**) x = 0.03, (**c**) $x = 0.033$, (**d**) $x = 0.066$, (**e**) x = 0.09, (**f**) x = 0.132, (**g**) x = 0.264, (**h**) x = 0.27 and (**i**) **x = 0.528.**

3.3.2 FESEM-EDX characterizations

The prepared samples were further characterized by FESEM for morphological study. Figure 3.4 show the FESEM micrographs of $Ni_{0.6-x}Zn_{0.4}Co_xFe_2O_4$ at x = 0, 0.03, 0.27 and 0.528. It is observed that the morphology of prepared samples is very similar to each other. The crystallinity increased with Co^{2+} doping has been marked and the particles sizes lies in nanometer range having fairly narrow size distribution with some agglomeration of particles. The porous nature of samples has also been clearly seen in FESEM micrograph. The agglomeration in samples is due to the magnetic nature of nanoparticles.
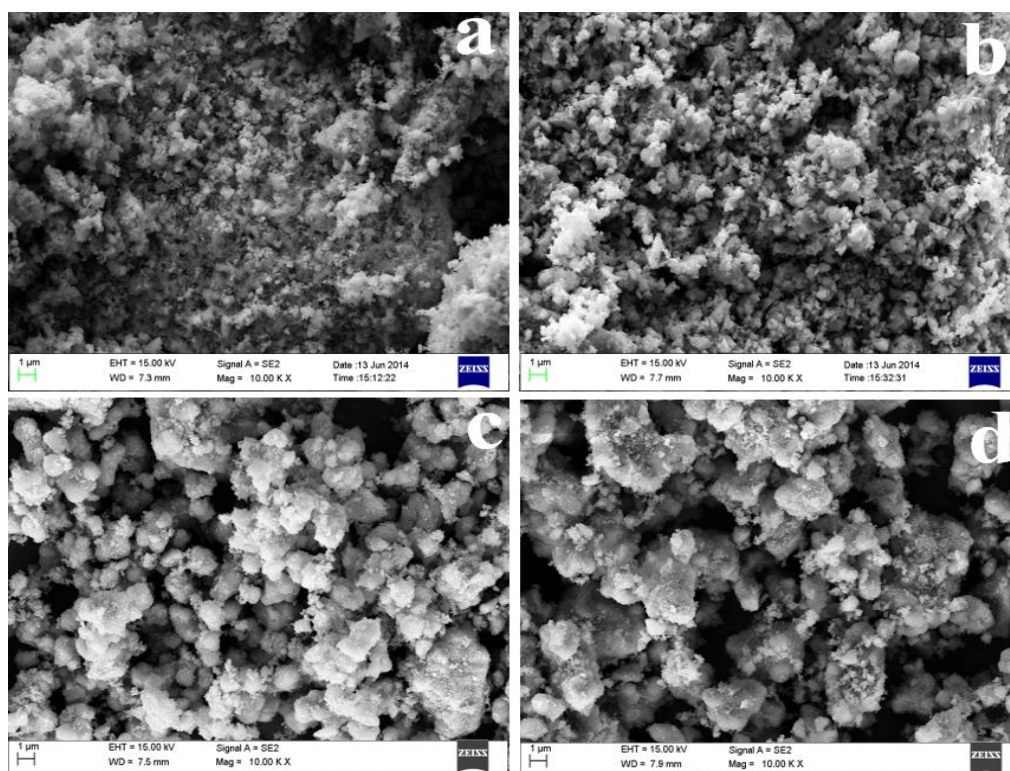
Figure 3.4: FESEM Micrographs of $Ni_{0.6-x}Zn_{0.4}Co_xFe_2O_4$ (a) x = 0, (b) x = 0.03, (c) x = 0.27 and (d) x = 0.528

The stoichiometry study of prepared samples has been performed by EDX. The EDX spectra of $Ni_{0.6-x}Zn_{0.4}Co_xFe_2O_4$ at x = 0, 0.03, 0.264, 0.27 and 0.528 are being presented in figure 3.5. The atomic percentage of elements present in prepared nanoparticles is tabulated in table 3.2. The results revealed that the prepared samples other than x = 0.264, 0.27 and 0.528 compositions are off-stoichiometric. At x = 0.264, 0.27 and 0.528, all the elements are found in expected composition. On the basis of these findings, it has been concluded that the sample prepared at x = 0.264, 0.27 and 0.528 attains good stoichiometry.
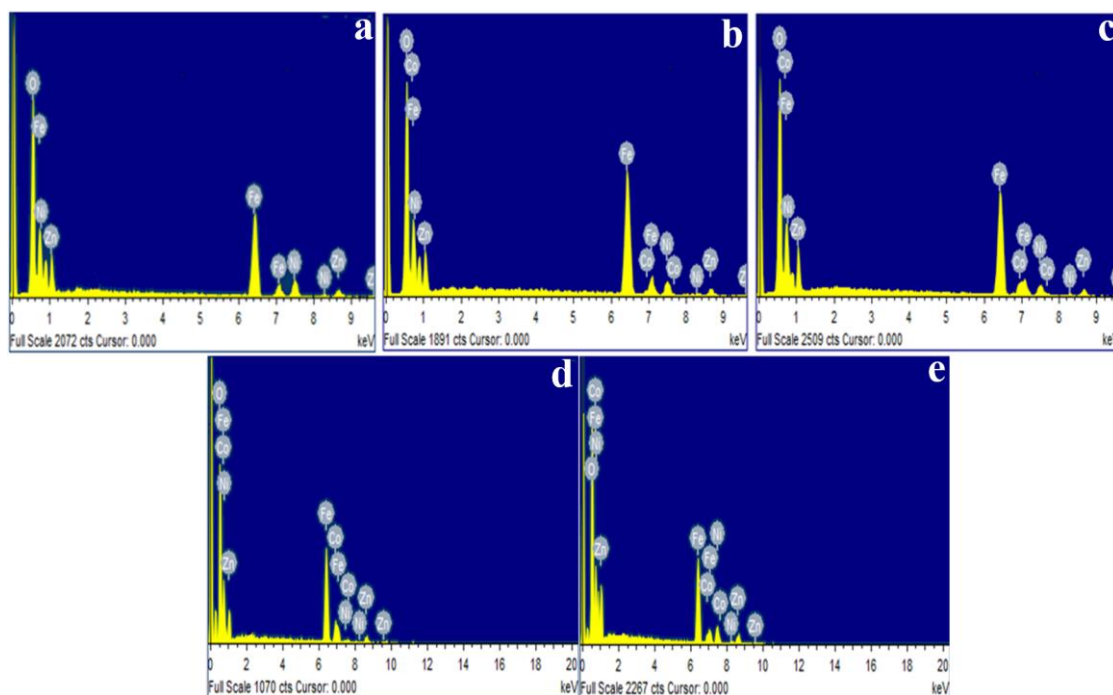
Figure 3.5: EDX spectra of $Ni_{0.6-x}Zn_{0.4}Co_xFe_2O_4$ (a) x = 0, (b) x = 0.03, (c) x = 0.264, (d) x = 0.27 and (e) x = 0.528.

Table 3.2. Atomic percentage of element present in prepared $Ni_{0.6-x}Zn_{0.4}Co_xFe_2O_4$ nanoparticles.

Composition x	*O (At. %)*	*Fe (At. %)*	*Ni (At. %)*	*Zn (At. %)*	*Co (At.%)*
0.000	52.18	33.01	9.98	4.83	0
0.030	50.87	36.41	8.86	3.23	0.63
0.264	57.57	28.97	4.58	5.47	3.41
0.270	56.93	29.12	4.67	5.53	3.75
0.528	57.34	28.89	1.03	5.76	6.98

3.3.3 Magnetic characterization

The magnetic properties of $Ni_{0.6-x}Zn_{0.4}Co_xFe_2O_4$ have been studied using VSM at room temperature and are illustrated in Figure 3.6. The obtained values of saturation magnetization (M_s), retentivity (M_r), coercivity (H_c) and squareness ratio (M_r/M_s) from the VSM are listed in table 3.3. The magnetization of spinel ferrite material strongly depends upon the super-exchange interaction between B and A sites magnetic ions. The net magnetic moment of the spinel system is the difference of B and A sites magnetic moment [99]. The standard magnetic moment values of Zn^{2+}, Ni^{2+}, Co^{2+} and Fe^{3+} ions are 0, 2, 3 and 5 μ_B respectively. The obtained value of M_s at x = 0, 0.03, 0.033, 0.066, 0.09, 0.132, 0.264, 0.27 and 0.528 are 35.61, 29.58, 27.63, 29.73, 30.57, 40.95, 58.53, 59.75 and 63.25 emu/g respectively. The magnetic moment (M_μ) was calculated using eqn.3.6 [100] and are listed in table 3.3.

$$M_{\mu} = (M_w \times M_s)/5585 \qquad\qquad (3.6)$$

where M_w is the molecular weight of the samples and M_s is the saturation magnetization of prepared nanoparticles.
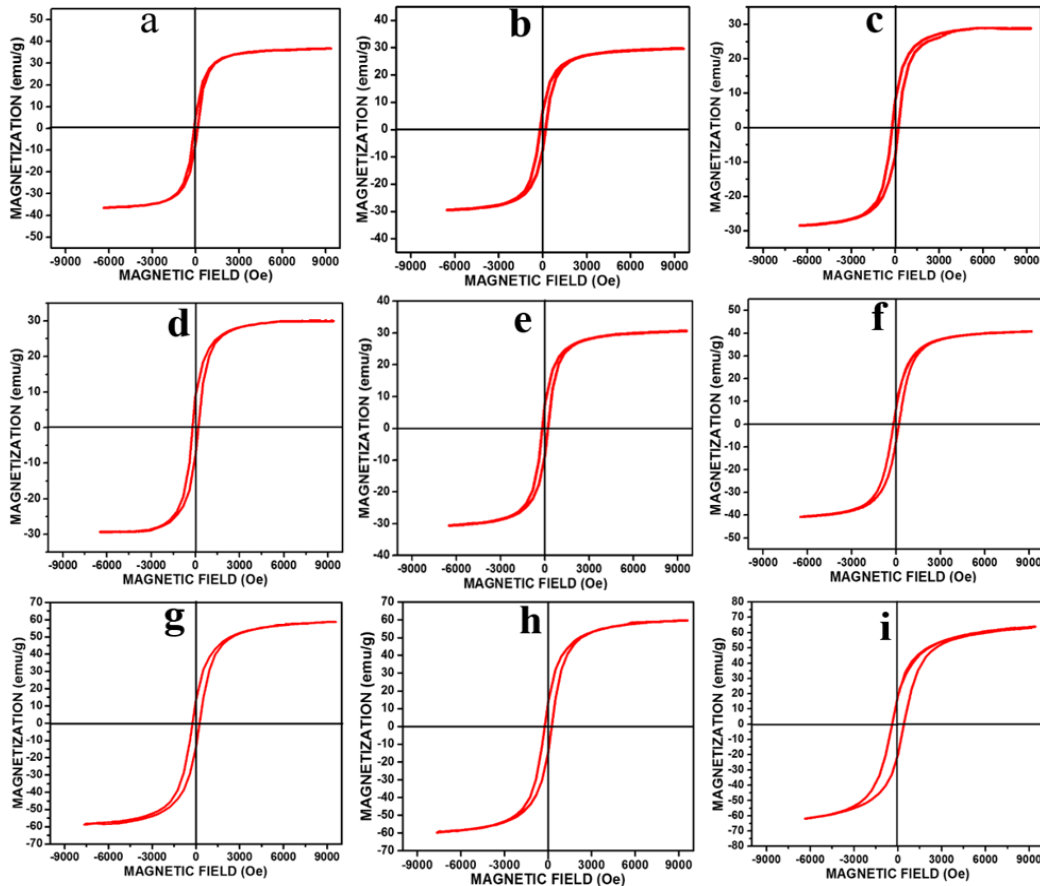
Figure 3.6: Hysteresis loops of $Ni_{0.6-x}Zn_{0.4}Co_xFe_2O_4$ of (a) x = 0, (b) x = 0.03, (c) x = 0.033, (d) x = 0.066, (e) x = 0.09, (f) x = 0.132, (g) x = 0.264, (h) x = 0.27 and (i) x = 0.528 at room temperature (300K).

It is found that M_s first decrease up to x = 0.033 and then increases with Co doping. The observed variation in M_s is explained on the basis of Co doping and secondary hematite phase effect. The effect of secondary hematite phase on M_s is explained on the basis of spin canting effect. The schematic diagram of spin canting effect is shown in figure 3.7. The obtained low value of M_s at $x = 0.033$ is due to anti-ferromagnetic hematite phase that is present in large extent at this composition with spinel phase (as seen in hematite phase peaks in XRD spectra). The interaction of anti-ferromagnetic hematite phase with ferromagnetic spinel phase cause dominant spin canting and decreases the total magnetic moment. This consequently decreases the M_s value of the system [101].

Table 3.3. Saturation magnetization (M_s), magnetic moment (M_μ), retentivity (M_r), coercivity (H_c), squareness ratio (M_r/M_s) and magneto crystalline anisotropy (K) measured using VSM.

x (Co Doping)	M_s (emu/g)	M_μ (μ_B)	M_r (emu/g)	H_c (Oe)	M_r/M_s	K (erg/cm^3)
0.000	35.61	1.511	06.24	126.28	0.1752	2248.41
0.030	29.58	1.255	07.15	188.00	0.2417	2780.52
0.033	27.63	1.172	07.65	189.32	0.2768	2615.45
0.066	29.73	1.262	08.32	191.73	0.2807	2850.06
0.090	30.57	1.297	08.98	193.11	0.2937	2951.68
0.132	40.95	1.738	10.12	202.25	0.2471	4141.06
0.264	58.53	2.485	13.95	234.45	0.2383	6861.17
0.270	59.75	2.536	14.26	236.46	0.2386	7064.24
0.528	63.25	2.686	18.43	448.23	0.2913	14175.27
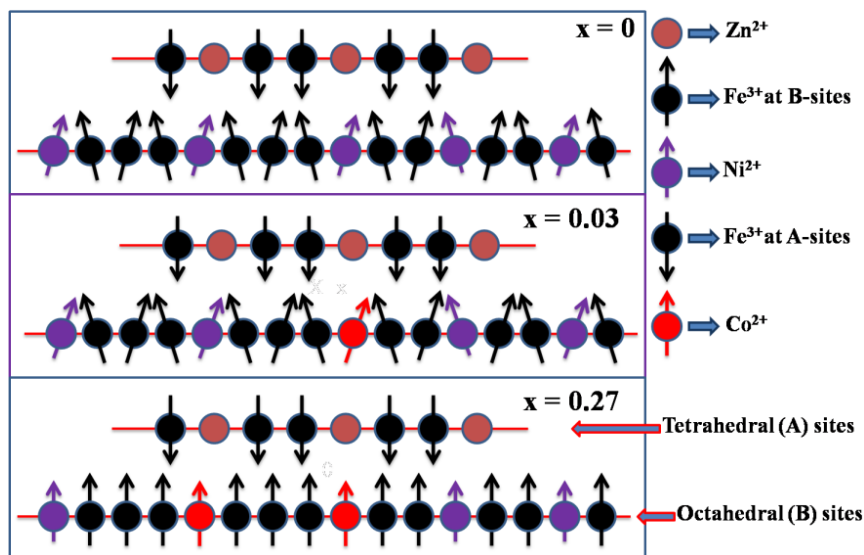
Figure 3.7: Spin canting behavior in $Ni_{0.6-x}Zn_{0.4}Co_xFe_2O_4$ systems on Co doping.

Figure 3.7 shows that prepared sample at x = 0.03 has high spin canting effect then that at x = 0. Higher the concentration of hematite secondary phases in spinel ferrite nanoparticles, higher the spin canting effect resulting to decrease in total magnetic moment of the system. Increased M_s after x = 0.033 doping is credited to the increasing concentration of Co^{2+} ions which has high magnetic moment that replace the lower magnetic moment Ni^{2+} ions in sites B and also decreases the spin canting effect caused by decreasing hematite secondary phase. These consequently increase the super-exchange interaction and total magnetic moment. Further at high concentration of Co doping (x = 0.264, 0.27 and 0.528),

concentration of Co^{2+} ions also increase in sites B that increase the total magnetic moment of the system with nil spin canting effect (figure 3.7) as no secondary hematite phase exists at this composition (confirmed by XRD peaks). Consequently, net magnetic moment and M_s increases. The values of M_r and H_c have slightly increased with Co doping because of its high magneto-crystalline anisotropy energy in sites B. With increasing doping concentration, carrier concentration of Co^{2+} ions increase in B sites and because of this, M_r and H_c increases. The value of M_r/M_s lies in the range of 0 to 0.5 indicates the magneto static interaction between the prepared nanoparticles. The increment in magneto crystalline anisotropy energy (K) value of Ni-Zn ferrite with Co doping has been calculated by following relation (eqn.3.7) [102] and tabulated in table 3.3:

$$H_c = 2K/M \qquad (3.7)$$

The above results show that all prepared powder samples are magnetically soft in nature and among them at $x = 0.528$ have highest saturation magnetization value. The best magnetic behavior at $x = 0.528$ indicates that this material can be useful as EMI shielding material. The relation between Co doping, D, M_s, H_c and ε is shown in Figure 3.8.
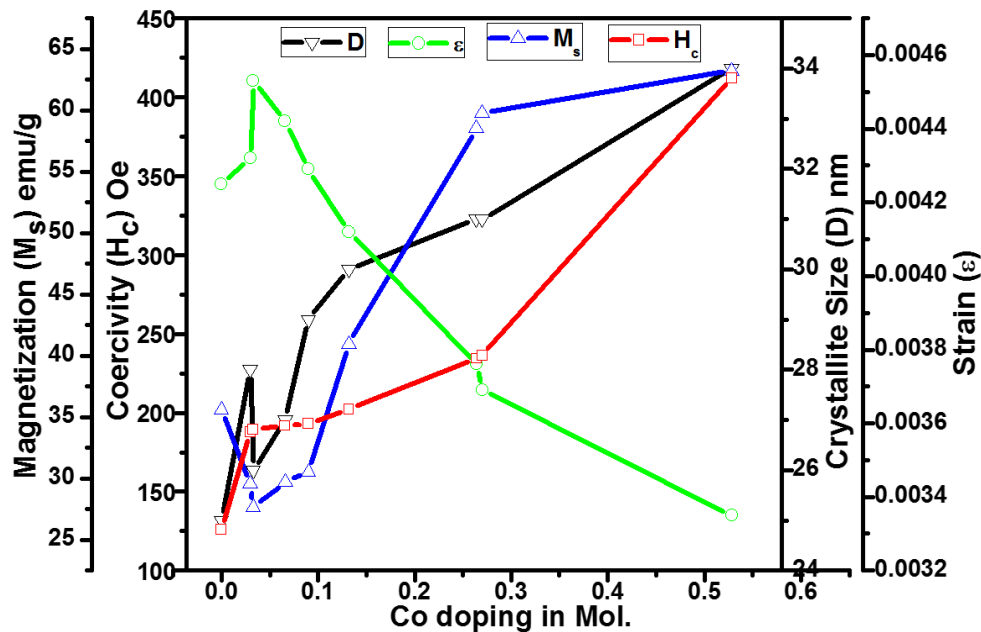
Figure 3.8: The relation between Co doping, crystallite size (D), saturation magnetization (M_s), coercivity (H_c) and strain (ε) for $Ni_{0.6-x}Zn_{0.4}Co_xFe_2O_4$.

It is concluded that D increases with Co doping because of larger ionic radii of Co^{2+} (0.745 A°) ions as compared to Ni^{2+} (0.69 A°). The obtained decreased value of D attributes to prominent secondary hematite phase effect that causes unit cells distortion. The value of H_c

increases with Co doping. The positive K value of Co^{2+} ions slight increases the value of H_c in ferrite. The secondary hematite phase found in the prepared samples is in the order of $I_{x=0.033}>$ $I_{x=0.066}> I_{x=0.03} > I_{x=0.09} > I_{x=0} > I_{x=0.132}$ as seen from XRD spectra. From figure 3.8, it is concluded that as the secondary phase increases in the samples, ε also increases. Thus ε is proportional to the secondary hematite phase. The M_s value is also strongly influenced by hematite secondary phase. The secondary hematite phase is higher with respect to spinel phase cubic structure, resulting to higher spin canting effect which in turn reduces the value of M_s. The M_s value of the ferrite inversely depends on the secondary hematite phase. Lastly, it is concluded that structural and magnetic properties of spinel ferrite system directly depend upon dopant concentration with different size and magnetic moment and the amount of hematite phase present in the system.

3.4 Theoretical calculation for cation distribution

The confirmation of variation in structural and magnetic properties with Co doping has been done theoretically from most suitable proposed cations distribution.

3.4.1. Structural analysis

Theoretical value of lattice constant (a_{th}) has been calculated using eqn.3.8 [103] by taking the mean ionic radii of both sites A and B (cations radii) from proposed cations distribution. The r_A and r_B are the mean ionic radii of site A and B respectively and has been calculated from cation distribution (eqn.3.9 and eqn.3.10) [104-106] and R_o is the ionic radii of oxygen 1.32 Å. The most appropriate proposed cations distribution, calculated lattice constant (a_{th}), r_A, r_B, oxygen positional parameter (u) and inversion parameter (δ) for $Ni_{0.6-x}Zn_{0.4}Co_xFe_2O_4$ system are listed in table 3.4.

$$a_{th} = 8/3\sqrt{3}[(r_A + R_o) + \sqrt{3}(r_B + R_o)] \qquad (3.8)$$

$$r_A = [C_{Zn2+}.r_{Zn2+} + C_{Fe3+}.r_{Fe3+}] \qquad (3.9)$$

$$r_B = 1/2[C_{Ni2+}.r_{Ni2+} + C_{Co2+}.r_{Co2+} + C_{Fe3+}.r_{Fe3+}] \qquad (3.10)$$

where C and r are the concentration and ionic radii of metal cations respectively.

Table 3.4. Proposed cations distribution [(*A1-A9: Zn₀.₄Fe₀.₆*) and (*B1: Ni₀.₆Fe₁.₄*, *B2: Ni₀.₅₇Co₀.₀₃Fe₁.₄*, *B3: Ni₀.₅₆₇Co₀.₀₃₃Fe₁.₄*, *B4: Ni₀.₅₃₄Co₀.₀₆₆Fe₁.₄*, *B5: Ni₀.₅₁Co₀.₀₉Fe₁.₄*, *B6: Ni₀.₄₆₈Co₀.₁₃₂Fe₁.₄*, *B7: Ni₀.₃₃₆Co₀.₂₆₄Fe₁.₄*, *B8: Ni₀.₃₃Co₀.₂₇Fe₁.₄*, *B9: Ni₀.₀₇₂Co₀.₅₂₈Fe₁.₄*], mean ionic radii of tetrahedral site (*r_A*), mean ionic radii of octahedral site (*r_B*), theoretical lattice constant (*a_{th}*), experimental lattice constant (*a*), oxygen parameter (*u*) and inversion parameter (*δ*).

x	*Cation Distribution Site A*	*Cation Distribution Site B*	*r_A* (Å)	*r_B* (Å)	*a_{th}* (Å)	*a* (Å)	*u* (Å)	*δ* (Å)
0.000	A1	B1	0.7300	0.6760	8.4786	8.3608	0.38959	0.01459
0.030	A2	B2	0.7300	0.6768	8.4808	8.3563	0.38956	0.01456
0.033	A3	B3	0.7300	0.6769	8.4810	8.3389	0.38955	0.01455
0.066	A4	B4	0.7300	0.6778	8.4834	8.3449	0.38951	0.01451
0.090	A5	B5	0.7300	0.6784	8.4850	8.3489	0.38949	0.01449
0.132	A6	B6	0.7300	0.6796	8.4882	8.3549	0.38943	0.01443
0.264	A7	B7	0.7300	0.6832	8.4978	8.3595	0.38928	0.01428
0.270	A8	B8	0.7300	0.6834	8.4984	8.3608	0.38927	0.01427
0.528	A9	B9	0.7300	0.6905	8.5173	8.3801	0.38896	0.01396

According to most suitable proposed cations distributions, all doped Co^{2+} ions are distributed over sites B in place of Ni^{2+} ions and increase the r_B because of its larger size that cause increase in lattice parameters. The sites A are unaffected by doping because of Co^{2+} ions incorporated in sites B and r_A remains constant. As the doping concentration increased with this trend, r_B increases as a increases with doping. Also a_{th} has been found continuously increasing with Co doping because of distribution of larger size all Co^{2+} ions in sites B in place of smaller size Ni^{2+} ions. On the account of these distributions in sites B, a_{th} increases as a function of Co doping. The obtained experimental a first decrease up to x = 0.033 and then increases with Co doping or the experimental a increase with Co doping from 8.3608 to 8.3801 Å. The alterations in experimental lattice constant (*a*) are due to secondary hematite phase effect as discussed in section 3.3.1. The variation in a_{th} and a is due to non-consideration of hematite secondary phase effect in theoretical calculation. The a_{th} is larger than a because of the assumption of ideal unit cell of spinel structure in which anions and cations are arranged as rigid sphere in perfect manner [105]. The value of oxygen parameter (*u*) has been theoretically calculated using eqn.3.11 [107] and found to be continuously decreasing with Co doping.

$$u = 1/a_{th}(r_A + R_o) + 1/4 \qquad (3.11)$$

The calculated *u* value is slightly higher than that of ideal oxygen parameter (*u* $_{ideal}$ = **0.375Å**) because of deformation of unit cells in nanometer range [103, 106]. In ideal spinel ferrite, all oxygen ions are arranged in exact cubical closed packing with the value of **u**$_{ideal}$=0.375 Å [103]. The decrease in the value of *u* with doping is due to the expansion of sites B by virtue of distribution of larger size Co^{2+} ions in sites B. *u* give the information regarding shifting in the position of oxygen ions with distribution of cations in A and B sites having different size [108]. The inversion parameter or deviation from ideal oxygen positional parameter (δ) has been calculated using relation (eqn.3.12) [106] and found that it is continuously decreasing because of shifting of oxygen position in B sites towards its equilibrium position with Co doping.

$$\delta = u - u_{ideal} \qquad\qquad (3.12)$$

Finally, to conclude; *a*$_{th}$ and *a* shows similar behavior and support the proposed cations distribution. The theoretical and experimental results have good agreement with each other according to proposed cations distribution.

3.4.2. Magnetic analysis:

The magnetic moments (*N*$_{\mu}$) per unit formula of prepared samples was also calculated from Neel's two sub lattices model of ferrimagnetism (eqn.3.13) [109, 99] i.e.

$$N_{\mu} = M(B) - M(A \qquad\qquad (3.13)$$

by taking magnetic moment of cations, where M(B) and M(A) are the sub lattice magnetic moments of B and A sites respectively and are tabulated in table 3.6. The values *N*$_{\mu}$ were also calculated on the basis of proposed cations distribution on B and A sites having different magnetic moment. The calculated *N*$_{\mu}$ continuously increase with Co doping by means of Co^{2+} ions distribution in sites B having high magnetic moment than replaced Ni^{2+} ions. The obtained *M*$_{s}$ value and *M*$_{\mu}$ from VSM data first decrease up to x = 0.033 and then continuously increases with Co doping as discussed in section 3.3.3. The obtained decreased value of *M*$_{s}$ and *M*$_{\mu}$ with doping is due to prominent hematite phase causing high spin canting effect as discussed in section 3.3.3 which decreases the total magnetic moment of the system (not considered in theoretical calculation). Finally, *N*$_{\mu}$ from proposed cations distribution have good agreement with increased *M*$_{s}$ and *M*$_{\mu}$ obtained from experimental data. The effect of Co doping on the overall strength of magnetic interactions; A-B, A-A and B-B interactions have been theoretically analyzed. The strength of interactions varies directly with bond angles and

inversely for bond length [110]. The configuration ions pairs with their interatomic distance and bond angle between metal cations and anions in spinel ferrite for favorable magnetic interactions are shown in figure 3.9 [106].
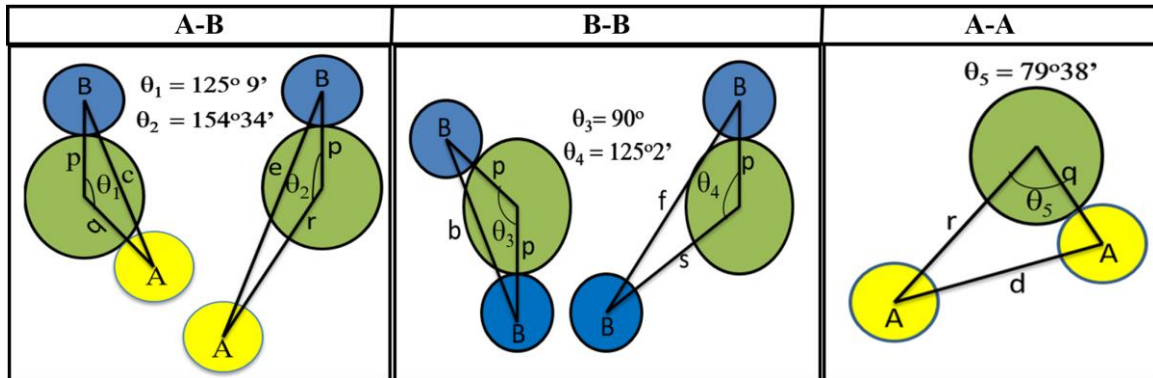
Figure 3.9: Configuration ions pairs with their interatomic distance and bond angle between metal cations and anions in spinel ferrite for favorable magnetic interactions.

The interatomic distance between cation-cations (***b-f***) (eqn.3.14-eqn.3.18) and cation-anion (***p-s***) (eqn.3.19-eqn.3.22) has been calculated using the following equations [111] by taking experimentally calculated lattice constant (***a***) and oxygen parameter (***u***). The value of cation-cation distance and cation- anion distance is tabulated in table 3.5.

Cation-cation distances

$$b = a/4\,(2)^{1/2} \qquad (3.14) \qquad\qquad c = a/8\,(11)^{1/2} \qquad (3.15)$$

$$d = a/4\,(3)^{1/2} \qquad (3.16) \qquad\qquad e = 3a/8\,(3)^{1/2} \qquad (3.17)$$

$$f = a/4\,(6)^{1/2} \qquad (3.18)$$

Cation-anion distances

$$p = a\,(5/8 - u) \qquad (3.19) \qquad\qquad q = a\,(u - 1/4)\,(3)^{1/2} \qquad (3.20)$$

$$r = a\,(u - 1/4)\,(11)^{1/2} \qquad (3.21) \qquad\qquad s = a\,(1/3u + 1/8)\,(3)^{1/2} \qquad (3.22)$$

Using cation-cation (**b-f**) and cation-anion distance (**p-s**), the bond angles θ_1, θ_2, θ_3, θ_4 and θ_5 were calculated using the following equation (eqn.3.23-eqn.3.27) [112] and listed in table 3.6.

$$\theta_1 = \cos^{-1}[p^2 + q^2 - c^2 / 2pq] \quad (3.23) \qquad \theta_2 = \cos^{-1}[p^2 + r^2 - e^2 / 2pr] \quad (3.24)$$

$$\theta_3 = \cos^{-1}[2p^2 - b^2 / 2p^2] \quad (3.25) \qquad \theta_4 = \cos^{-1}[p^2 + s^2 - f^2 / 2ps] \quad (3.26)$$

$$\theta_5 = \cos^{-1}[r^2 + q^2 - d^2 / 2rq] \quad (3.27)$$

Table 3.5. Cation-cation (**b, c, d, e, f**) and cation-anion (**p, q, r, s**) for $Ni_{0.6-x}Zn_{0.4}Co_xFe_2O_4$ nanoparticles.

x	b (Å)	c (Å)	d (Å)	e (Å)	f (Å)	p (Å)	q (Å)	r (Å)	s (Å)
0.000	2.9555	3.4655	3.6202	5.4303	5.1000	1.9681	2.0214	3.8702	3.6906
0.030	2.9539	3.4636	3.6182	5.4274	5.0973	1.9673	2.0199	3.8672	3.6885
0.033	2.9478	3.4564	3.6107	5.4161	5.0867	1.9633	2.0156	3.8590	3.6808
0.066	2.9499	3.4589	3.6133	5.4200	5.0903	1.9650	2.0165	3.8607	3.6832
0.090	2.9513	3.4606	3.6150	5.4226	5.0928	1.9662	2.0170	3.8618	3.6849
0.132	2.9534	3.4631	3.6176	5.4265	5.0964	1.9680	2.0177	3.8631	3.6873
0.264	2.9550	3.4650	3.6196	5.4294	5.0992	1.9704	2.0166	3.8609	3.6885
0.270	2.9555	3.4655	3.6202	5.4303	5.1000	1.9708	2.0168	3.8612	3.6891
0.528	2.9623	3.4735	3.6285	5.4428	5.1118	1.9780	2.0169	3.8615	3.6961

The strength of A-B and A-A magnetic interaction directly depends on θ_1, θ_2 and θ_5 while B-B interactions vary with θ_3 and θ_4 respectively [110, 112]. It is found that the interatomic distance between cation-cation (**b, c, d, e, f**) and cation-anion (**p, s**) first decrease up to x = 0.033 and then increases with Co doping.

Table 3.6. Bond angles (θ_1, θ_2, θ_3, θ_4, θ_5) between ions pairs and theoretically calculated magnetic moment (N_μ) for $Ni_{0.6-x}Zn_{0.4}Co_xFe_2O_4$.

X	θ_1 (Degree)	θ_2 (Degree)	θ_3 (Degree)	θ_4 (Degree)	θ_5 (Degree)	N_μ (μ_B)
0.000	120.595	134.279	97.326	125.887	67.613	5.200
0.030	120.606	134.318	97.307	125.883	67.639	5.230
0.033	120.607	134.323	97.304	125.883	67.643	5.233
0.066	120.619	134.367	97.282	125.879	67.672	5.266
0.090	120.628	134.397	97.268	125.876	67.692	5.290
0.132	120.644	134.455	97.239	125.870	67.731	5.332
0.264	120.693	134.632	97.152	125.853	67.848	5.464
0.270	120.696	134.642	97.147	125.852	67.855	5.470
0.528	120.793	134.991	96.977	125.818	68.087	5.728

The decreased values of cation-cation (b, c, d, e, f) and cation-anion (p, s) interatomic distance are due to hematite phase effect. The increasing values of cation-cation (b, c, d, e, f) and cation-anion (p, s) are due to increasing concentration of larger size Co^{2+} ions in sites B in place of smaller size Ni^{2+} ions and diminishing hematite phase effect. The value of θ_1, θ_2 and θ_5 continuously increased with Co doping remarks the strengthening of A-B and A-A interactions. The value of θ_3 and θ_4 continuously decreases indicating the weakening of B-B interactions with Co doping. The increase in A-B interaction is due to the incorporation of high magnetic moment Co^{2+} ions in sites B. The increase in A-A interactions is due to decrease in cation-cation interatomic distance q and r with doping with respect to x = 0. The variation in cation-cation, cation-anion interatomic distance and bond angles with Co doping also support the proposed cation distributions.

3.5 Conclusion

Present study demonstrated the effect of Co doping on structural and magnetic properties of $Ni_{0.6-x}Zn_{0.4}Co_xFe_2O_4$ nanoparticles synthesized using sol-gel method and annealed at 700°C. XRD study revealed that samples prepared at x = 0.264, 0.27 and 0.528 have single phase spinel cubic structure. There is partial formation of secondary hematite phase (α-Fe_2O_3) with spinel phase cubic structure of $Ni_{0.6-x}Zn_{0.4}Co_xFe_2O_4$ nanoparticles for other composition. The crystallite size (D) increases with Co doping because of larger ionic radii of Co^{2+} ions as compared to Ni^{2+} ions. The decrease in crystallite size (D) possibly attributes to prominent hematite phase effect. The strain present in the crystal structure also increases with secondary phase because of lattice distortion produced by hematite secondary phase. Positive slope of linear fitted W-H plots indicates that tensile strain presents in all prepared nanoparticles. The crystallinity of prepared samples increases with Co doping and has been investigated by FESEM. EDX study, revealed that all the elements present in the samples at x = 0.264, 0.27 and 0.528 are in stoichiometric ratio, but the samples other than these are in off-stoichiometry. The saturation magnetization (M_s) firstly decreases with Co doping up to x = 0.033 and then increases as observed from a VSM study. The reduced value of saturation magnetization (M_s) is attributed to the dominant spin canting effect caused by prominent secondary phase found in the sample. The increased value of saturation magnetization (M_s) is credited to high magnetic moment of Co^{2+} ions that replace the

Ni^{2+} ions in octahedral (B) sites and decreasing the effect of secondary hematite phase. The values of retentivity (M_r) as well as coercivity (H_c) increased with Co doping due to the positive magneto-crystalline anisotropy energy (K) of Co ions that is imparted in Ni-Zn ferrite system. The theoretically calculated structural and magnetic parameters from proposed cations distributions have good agreement with results that are obtained from experimental data. The single phase spinel cubic structure and higher value of saturation magnetization (M_s) at 0.528 indicates the usefulness of these materials in EMI shielding.

CHAPTER-4

EFFECT OF ANNEALING TEMPERATURE ON STRUCTURAL AND MAGNETIC PROPERTIES OF Co DOPED Ni-Zn FERRITE NANOPARTICLES
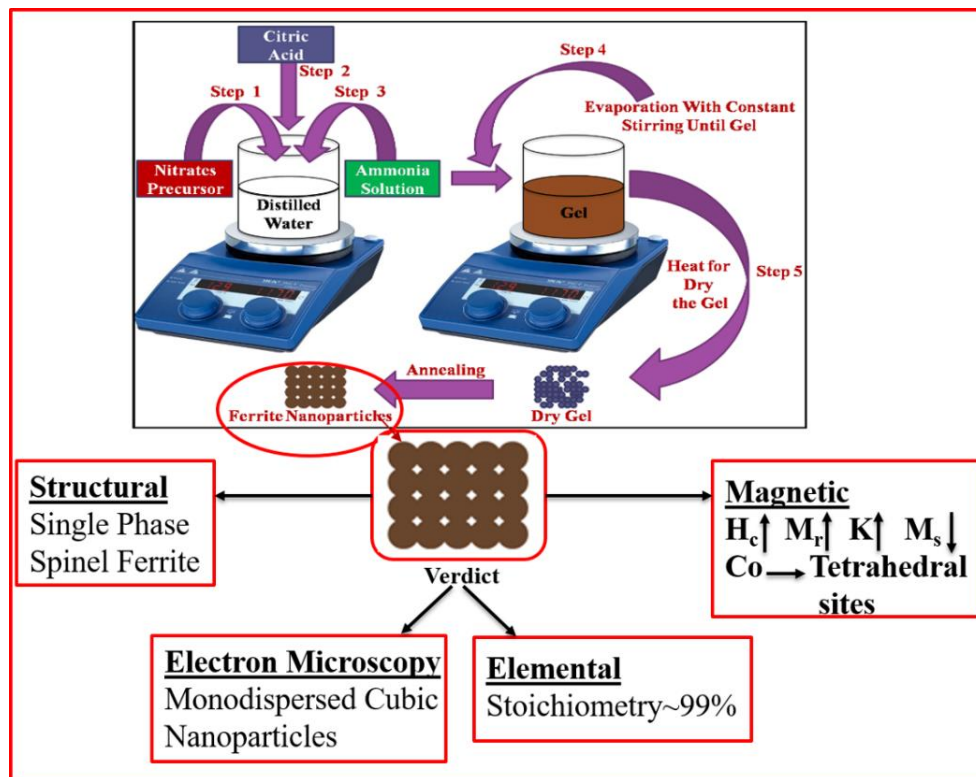
4.1 Introduction

Ferrimagnetic materials are scientifically very important because of their significant properties such as high electrical resistivity, high permeability, low eddy current losses and good chemical stability. Therefore, these materials are used in transformer cores, radio frequency coils, rod antennas, read & write heads and electromagnetic wave absorber applications [113-114, 66]. The physical properties of spinel ferrites nanoparticles depend on their chemical compositions, preparation techniques, cations substitutions on A and B sites, the type of dopants and annealing temperature [115-116]. Electrical or magnetic properties of ferrites can be improved by doping with different metal cations [117-118, 55]. Among the ferrimagnetic materials, spinel Ni–Zn ferrites are most used materials. Ni–Zn ferrites are good candidates for high frequency applications because they possess high magnetization, high electrical resistivity and low eddy current losses [119]. The power application devices such as transformer and inductor cores have found to be made up of Ni–Zn ferrites [61]. Ni–Zn ferrite normally has mixed spinel structure which consists of eight A and sixteen B sites occupied by the cations [63]. Zn^{2+} cations also have a tendency to occupy both A and B sites [120-123]. The distribution of cations in Ni-Zn ferrites sub lattices also depend upon annealing temperature [124]. The doping of Co^{2+} ions in Ni–Zn ferrites improves its magnetic properties and can be used as microwave absorber or for EMI shielding applications [87, 68-69]. Xiang et. al. [125] investigated that Co doping enhances the M_s and H_c of Mn–Zn ferrites. The magnetic properties of spinel ferrites nanoparticles are strongly influenced by distribution of cation in different sub-lattices which in turn depends on synthesis methods and annealing temperature [126-129]. In the literature, reported M_s of spinel type ferrites has been explained on the basis of cations distribution effect in sites A and B respectively [130]. H_c of spinel ferrites mainly depends upon K energy of cations and distribution of cations in different sub-lattices. Co has positive K value in sites B which increases the value of H_c [102]. H_c of spinel ferrite nanoparticles also depends on sintering or annealing temperature [131]. Khan et. al. [132] reported the Tb doped Co ferrite and the value of H_c obtained is in the range of 405–435 Oe which are very useful for high-density data storage devices. In the previous chapter 3, $Ni_{0.6-x}Zn_{0.4}Co_xFe_2O_4$ nanoparticles has been synthesized by *sol-gel* method for compositions (x = 0, 0.03, 0.033, 0.066, 0.09, 0.132, 0.264, 0.27, 0.528) annealed at 700°C temperature and studied for their structural and magnetic properties. It is found that the prepared nanoparticles with variations

of Co doping x = 0, 0.033, 0.066, 0.132, 0.264, 0.528 has reached to maximum replacement of Ni ions and attain high saturation magnetization than prepared nanoparticles with variation (x = 0, 0.03, 0.09, 0.27). It is also seen that the variation in structural and magnetic properties from x = 0.033 to 0.27 of Co doping are very small. Therefore, composition x = 0.03, 0.066, 0.09, 0.132 and 0.27 are not considered in present study. So in order to improve the magnetic properties of nanoparticles and to remove the impurity phase, again samples $Ni_{0.6-x}Zn_{0.4}Co_xFe_2O_4$ (x = 0, 0.0165, 0.033, 0.264 and 0.528) has been synthesized by sol–gel method and annealed at high temperature 1100°C. The effect of Co-doping and high annealing temperature on the structural, morphology, stoichiometry and magnetic properties of Ni–Zn ferrite has been investigated by X-ray diffraction (XRD), field emission scanning electron microscopy (FESEM), transmission electron microscopy (TEM), energy dispersive X-ray spectroscopy (EDX) and vibrating sample magnetometer (VSM). The obtained moderate M_s and low H_c of prepared samples annealed at 1100°C attributes that these materials can be useful for magnetic recording devices.

4.2 Experimental details

4.2.1 Synthesis and Characterizations of $Ni_{0.6-x}Zn_{0.4}Co_xFe_2O_4$ nanoparticles

Synthesis of $Ni_{0.6-x}Zn_{0.4}Co_xFe_2O_4$ (at x = 0, 0.033, 0.066, 0.132, 0.264, 0.528) nanoparticles has been carried out using *sol-gel* method as discussed in chapter 2 and prepared samples were annealed at high temperature 1100°C. Characterization techniques XRD, FESEM, EDX, TEM and VSM have been used to study the effect of annealing temperature and substitution on various properties.

4.3 Results and discussion

4.3.1 Distribution effect of cations

The variation in structural parameters such as D, d and a with doping can be explained on the basis of cations size difference that are distributed over sites A and B. Co doping can increase or decrease the value of D, d and a of Ni–Zn ferrite system. It depends on cations distribution in sites A and B having different radii. The distribution of cations also depends on synthesis methods and annealing temperature [126-129]. Depending on distribution, the value of D, d and a increases when all Co^{2+} ions go to site B replacing Ni^{2+} ions. Since the ionic radii of Co^{2+} (ionic

radii = 0.745 Å) is large as compared to Ni^{2+} (ionic radii = 0.69 Å) ions [78], this distribution trend results in the enlargement of the unit cells and hence, the lattice expansion occurs.

In the previous study, it was found that Co doping in Ni-Zn ferrite nanoparticle system increases the structural parameters (*D*, *d* and *a*) that is attributed to the Co distribution in site B [133] as discussed in chapter 3. When all Co^{2+} ions go to site A in place of Zn^{2+} ions (ionic radii = 0.82 Å), equivalent Zn^{2+} ions occupy site B in place of Ni^{2+} ions. With this trend of Co^{2+} and Zn^{2+} ions distribution, there is slight shrinkage in the unit cells causing *D*, *d* and *a* to decrease because of their ionic radii difference. When large fraction of Co^{2+} ions distributes over site A in place of Zn^{2+} ions and small fraction of Co^{2+} ions distributes over site B in place of Ni^{2+} ions, then enlargement in unit cells might occur. By virtue of Co^{2+} ions distribution in site A, the concentration of Zn^{2+} ions also increase in site B. Due to the effect of Co^{2+} ions distribution in site A, unit cells shrinkage is possible because of smaller ionic radii of Co^{2+} ions as compared to Zn^{2+} ions. Also with the distribution of larger Zn^{2+} ions in site B in place of smaller Ni^{2+} ions, enlargement in unit cells occurs. Moreover, small fraction of Co^{2+} ions goes to site B in place of Ni^{2+} ions and enlarge the unit cells because of larger ionic radii of Co^{2+} as compared to Ni^{2+} ions. Consequently, due to overall enlargement of the unit cells; *D*, *d* and *a* can be increased.

Tuning in the magnetic properties such as *M_s*, *M_r*, *H_c* and *K* with Co doping in Ni–Zn ferrite can also be explained by means of cations distribution effect on sites A and B having different magnetic moments in terms of annealing temperature. The standard magnetic moment values of Fe^{3+}, Ni^{2+}, Zn^{2+} and Co^{2+} are 5 μB, 2 μB, 0 μB and 3 μB respectively. The net magnetic moment of spinel ferrite is the difference between sites B and A metal cations magnetic moment that aligns antiparallel to each other. Depending on the cation distribution, the magnetic properties either increase or decrease.

The cations distribution in spinel ferrites system is strongly influenced by annealing temperature which causes magnetic properties increase or decrease with annealing temperature [115-116, 124, 131]. Depending on annealing temperature, when doped Co^{2+} ions go to site B in place of Ni^{2+} ions and the magnetic moment of site B increases because of higher magnetic moment of Co^{2+} ions as compared to Ni^{2+} ions. Consequently, net magnetic moment of the system and *M_s* increase. As doping concentration increases by means of this type of distribution, the net magnetic moment and *M_s* also increases because of higher magnetic moment of Co^{2+} ions

that replace more Ni^{2+} ions in site B and increase the magnetic moment in site B. By virtue of these consequences, net magnetic moment and M_s increases with Co doping. In the previous study, increase in magnetic properties with Co doping in Ni-Zn ferrite system were found which attributes to the distribution of Co ions in site B [133]. By virtue of annealing temperature effect, when all doped Co^{2+} ions are distributed over site A in place of Zn^{2+} ions instead of site B in place of Ni^{2+} ions, M_s decreases. Because of this type of cations distribution, the magnetic moment of site A increases (due to higher magnetic moment of Co^{2+} ions than Zn^{2+} ions). Also magnetic moment of site B decreases (due to zero magnetic moment of Zn^{2+} ions) and thus, net magnetic moment and M_s decreases. As the doping concentration increases with this type of distribution, the concentration of Co^{2+} ions increase in site A and the concentration of Zn^{2+} ions also increases in site B. Further net magnetic moment and M_s decreased with Co doping. The values of M_r and H_c directly depend upon K value of Co^{2+} ions and its distribution in different sub lattices. Distribution of Co^{2+} ions in site A decrease the value of M_r and H_c because of its minimum K value in sites A. While distribution of Co^{2+} ions in sites B increase the value of M_r and H_c that intended to positive K value of Co^{2+} ions in site B. Finally, structural and magnetic properties of spinel ferrites nanoparticles are depending on cations distribution by means of synthesis method and annealing temperature.

4.3.2 XRD characterization

All the prepared samples have been characterized by powder XRD characterization for structural analysis. The XRD patterns are presented in figure 4.1. From XRD spectra, it is found that when samples annealed at 1100°C, most of the hematite phase diminished other than at x = 0.0165. This is due to conversion of hematite phase into spinel phase cubic structure at high temperature [134-135]. The XRD peaks at (111), (022), (113), (222), (004), (224), (333) and (044) indicates that the prepared samples at x = 0, 0.033, 0.264 and 0.528 have single phase spinel cubic structure whereas at x = 0.0165 there is partial formation of hematite (α-Fe_2O_3) secondary phase with spinel structure. The diffraction peaks have good agreement with standard JCPDS card no.52-0277 and 89-0599, corresponding to spinel Ni-Zn ferrite and hematite (α-Fe_2O_3) phase respectively. Using Scherrer's formula, average D of all prepared samples has been calculated

from full-width at half-maxima (FWHM) of most prominent peak (113) of XRD patterns [94] and tabulated in table 4.1.
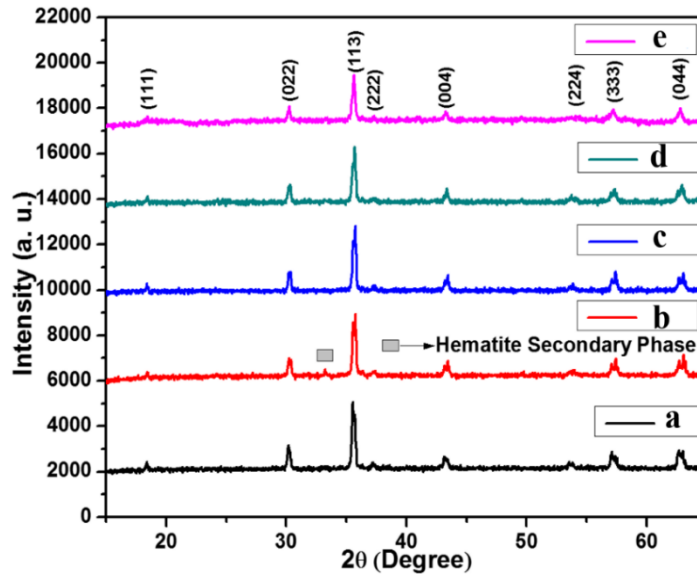
Figure 4.1: XRD Spectra of $Ni_{0.6-x}Zn_{0.4}Co_xFe_2O_4$ (a (x = 0), b (x = 0.0165), c (x = 0.033, d (x = 0.264) and e (x = 0.528)).

The D value of un-doped sample annealed at 1100°C is slightly smaller than that of samples annealed at 700°C (chapter-3). The smaller D is attributed to the increasing crystallinity, increasing density and due to removing of defects [134] at high annealing temperature (1100°C). Further with Co doping, the variation in D has been explained in terms of distribution of cation in different sub lattices. The distribution of cations also depends on synthesis methods and annealing temperature [126-129]. Co^{2+} ions also have tendency to occupy both sites A and B [136-138]. The slight decrease in D at x = 0.0165 and 0.033 is expected due to the Co^{2+} and Zn^{2+} ions distribution effect on sites A and B having different radii. With Co doping at x = 0.0165 and 0.033 in Ni-Zn ferrite, all Co^{2+} ions replace Zn^{2+} ions at site A and possibly equivalent Zn^{2+} ions occupy site B in place of Ni^{2+} (ionic radii = 0.69 Å) ions. With this type of Co^{2+} and Zn^{2+} ions distribution effect, there is slight shrinkage in the unit cell that causes decrease in D. The size obtained at x = 0.0165 is smaller than the size obtained at x = 0.033 is attributed to the presence of antiferromagnetic hematite phase (α-Fe_2O_3) with spinel phase as seen in hematite phase peak in XRD that cause distortion in the unit cell and additional unit cell shrinkage occurs. Further at x = 0.264, larger number of Co^{2+} ions go in site A with small fraction in site B. By virtue of Co^{2+}

ions distribution in site A, unit cell shrinkage is there. Also with the distribution of Zn^{2+} ions in site B, enlargement in unit cells occur. Moreover, small fractions of Co^{2+} ions go to site B in place of Ni^{2+} ions and enlarge the unit cell. At high doping concentration (x = 0.528), the concentration of Co^{2+} ions increase in both the sites causing the enlargement in unit cell occur (discussed in section 4.3.1). As a result, D value increases. The effect of annealing temperature and Co doping on d [95] and a [96] have been calculated and presented in table 4.1. It is found that d and a value of undoped Ni-Zn ferrite nanoparticles is slightly larger when annealed at high temperature 1100°C. Further with Co doping, d and a value first decreases from x = 0.0165 to 0.033 and then increases with Co doping. The variations obtained in structural parameters are due to high annealing temperature effect [139-140]. At x = 0.0165, all Co^{2+} ions go in smaller site A and comparable distribution of Zn^{2+} ions in larger site B causes the decrease in d and a values at x = 0.0165 and also attributed to the presence of hematite phase at this particular composition resulting to lattice shrinkage. With Co doping at x = 0.033, all Co^{2+} ions also distributed in site A and equivalent Zn^{2+} ions are distributed over site B. By virtue of high concentration of Co^{2+} ions in site A, more lattice shrinkage occurs than at x = 0.0165. The increasing values of d and a by means of Co doping (at x = 0.264 and 0.528) attributes to the lattice expansion caused by distribution of Co^{2+} and Zn^{2+} ions in both sites as discuss in section 4.3.1. The ε present in nanoparticles has been calculated using Stocks-Wilson equation [97] and presented in table 4.1. It is found that when samples annealed at high temperature1100°C, ε in nanoparticles slightly increase because of smaller D. Further with doping, maximum ε is present at x = 0.0165 because of smallest D and hematite phase effect.

Table 4.1. Crystallite size (D), particle size (t), d-spacing (d), lattice constant (a) and strain (ε) calculated from prominent peak (113) of XRD; crystallite size (W-H D) calculated from Williamson-Hall plots.

x	D (nm)	t (nm)	d (Å)	a (Å)	ε	W-H D (nm)
0.000	23	28	2.5218	8.3638	0.00480	18
0.0165	20	-	2.5174	8.3492	0.00508	13
0.033	22	-	2.5171	8.3451	0.00494	14
0.264	23	-	2.5193	8.3523	0.00486	17
0.528	27	33	2.5204	8.3560	0.00413	16

Also using Williamson-Hall (W-H) method [98], the estimated **W-H D** is inscribed in table 4.1. The W-H plots for $Ni_{0.6-x}Zn_{0.4}Co_xFe_2O_4$ nanoparticles system are shown in figure 4.2. The **W-H D** obtained from W-H plots is approximately equivalent to that calculated by Scherrer's formula. The negative slope of the linear fit in W-H plots shows a compressive strain which is present in all prepared samples [141-142]. The compressive strain present in annealing nanoparticles at high temperature 1100°C is due to reduction of porosity and increase in density of nanoparticles.
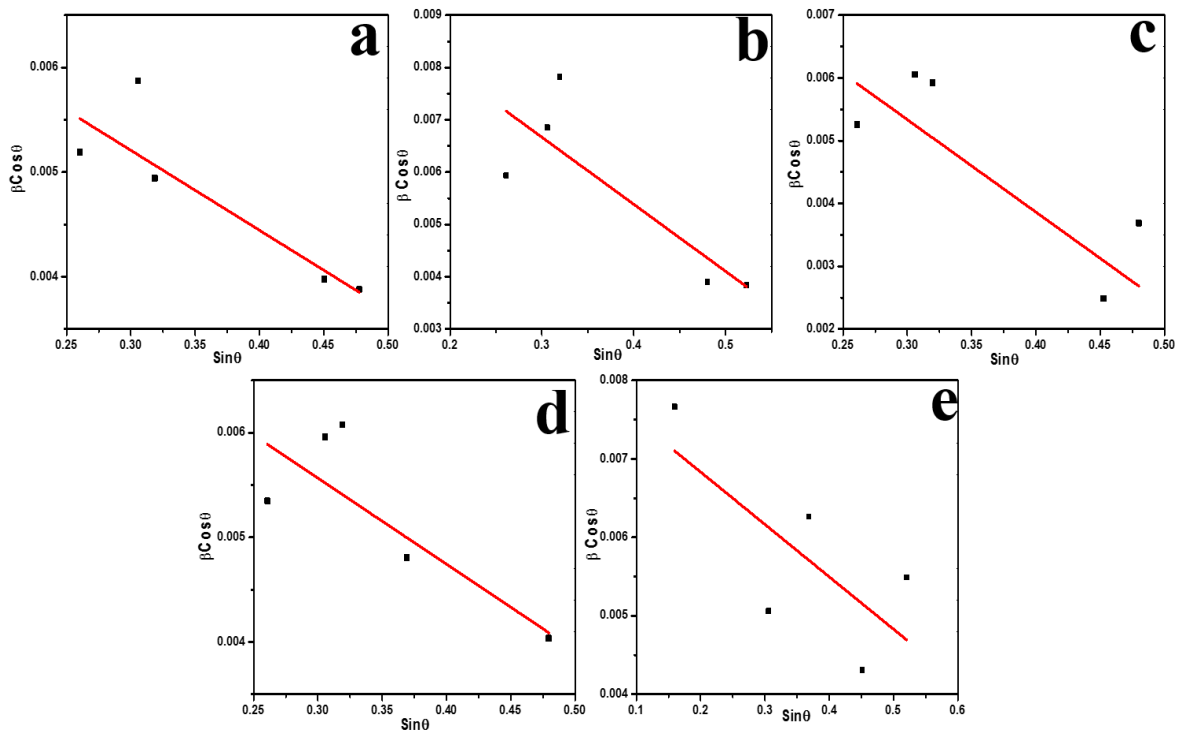
Figure 4.2: W–H plots of $Ni_{0.6-x}Zn_{0.4}Co_xFe_2O_4$ (a) x = 0, (b) x = 0.0165, (c) x = 0.033, (d) x = 0.264 and (e) x = 0.528.

4.3.3 FESEM-TEM-EDX characterizations

The morphology of prepared samples when annealed at 1100°C was further examined by FESEM. Figure 4.3 shows the FESEM micrographs of $Ni_{0.6-x}Zn_{0.4}Co_xFe_2O_4$. The morphology of the prepared samples is very similar to each other with non-uniform grain distribution and it is clearly seen that the crystallinity increase with some agglomeration of particles when annealed at high temperature 1100°C. Morphology of samples also depends on annealing temperature. The

morphology of samples annealed at 1100°C is different form that samples annealed at 700°C (chapter-3) (fig.3.5). It is clearly seen in FESEM micrograph, samples annealed at 1100°C are highly crystalline in nature than samples annealed at 700°C. Moreover, crystallinity also improves with annealing temperature [134]. By virtue of low magnification of FESEM micrographs and agglomeration of crystallites, the estimation of grain size is very difficult. Further samples have been characterized using TEM for the exact measurement of particle size and images at x = 0 and 0.528 are shown in figure 4.4 (a, b). The particle size (*t*) calculated from TEM images by using image j software and was found that the average particle size at x = 0 and 0.528 is 28 and 33 nm respectively and tabulated in table 4.1. The particle size (*t*) obtained from TEM is in good agreement with *D* measured from XRD. The particles size distribution has been observed using histogram from TEM images and results are tabulated in table 4.1. The histogram images are presented in figure 4.4 (a1, b1).
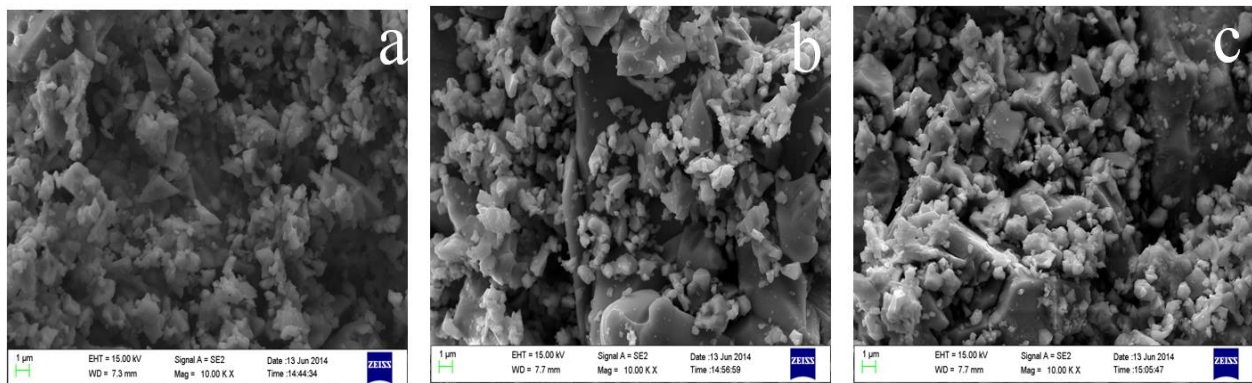
Figure 4.3: FESEM Micrographs of $Ni_{0.6-x}Zn_{0.4}Co_xFe_2O_4$ (a) x = 0, (b) x = 0.033 and (c) x = 0.264
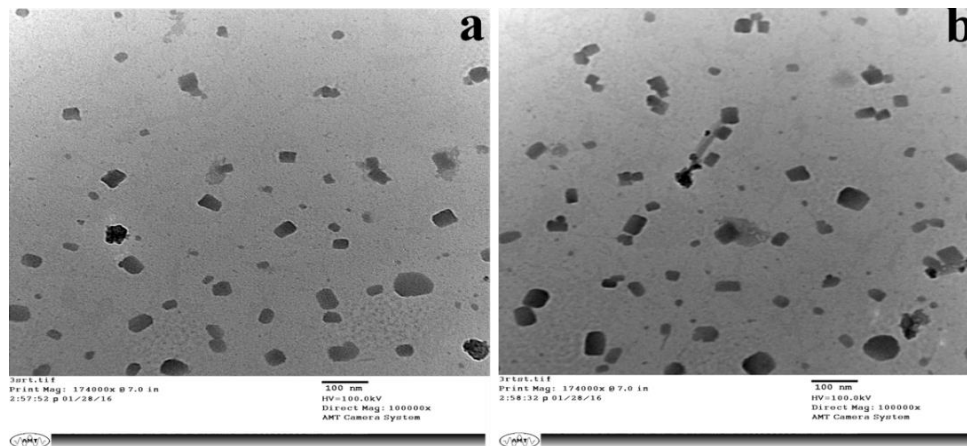
Figure 4.4 (a, b): TEM images of $Ni_{0.6-x}Zn_{0.4}Co_xFe_2O_4$ (a) x = 0 and (b) x = 0.528.
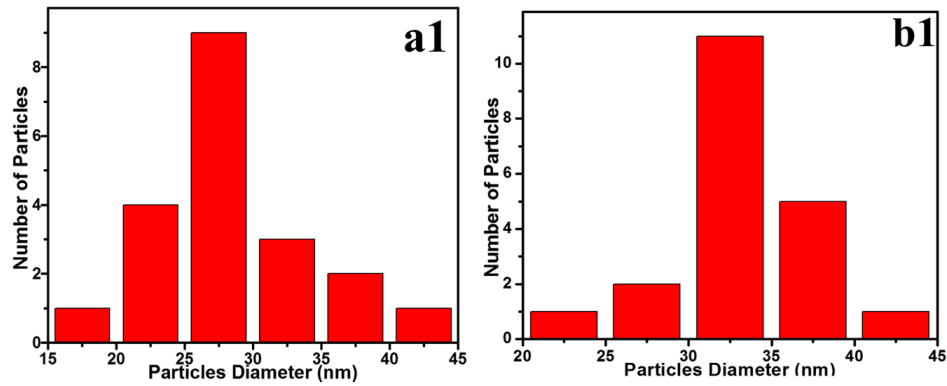
Figure 4.4 (a1, b1): Histogram of $Ni_{0.6-x}Zn_{0.4}Co_xFe_2O_4$ (a) x = 0 and (b) x = 0.528.

The prepared samples have been characterized by EDX for stoichiometry study. EDX spectra are shown in figure 4.5. The atomic compositions of the samples are tabulated in table 4.2 which reveals that the prepared samples annealed at 1100°C, all elements are present in definite and expected ratio. The obtained results show all prepared samples have good stoichiometry. As seen in chapter-3, samples annealed at 700°C are off-stoichiometric which becomes stoichiometric when annealed at 1100°C. This became at high annealing temperature where impurity phase diminishes.
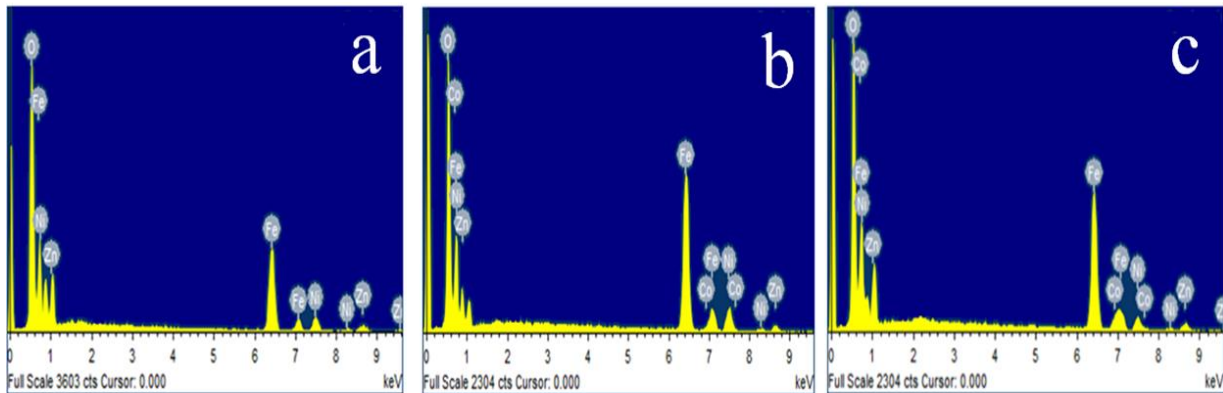
Figure 4.5: EDX micrographs of $Ni_{0.6-x}Zn_{0.4}Co_xFe_2O_4$ (a) x = 0, (b) x = 0.033 and (c) x = 0.264.

Table 4.2. Atomic percentage (At. %) of $Ni_{0.6-x}Zn_{0.4}Co_xFe_2O_4$ at x = 0, 0.033 and 0.264 obtained from EDX measurement.

Composition (x)	O (At. %)	Fe (At. %)	Ni (At. %)	Zn (At. %)	Co (At. %)
0	55.62	28.70	8.97	6.71	0
0.033	58.12	29.13	6.80	5.69	0.26
0.264	55.29	30.05	4.37	6.67	3.62

4.3.4 Magnetic characterization

$Ni_{0.6-x}Zn_{0.4}Co_xFe_2O_4$ nanoparticles have been employed to VSM for magnetic studies at room temperature and results are illustrated in figure 4.6 (M-H curve). The obtained values of M_s, M_r, H_c, M_r/M_s and K from VSM are listed in table 4.3. The magnetic properties of spinel ferrites strongly depend upon type of dopant cations, distribution of these cations in both sites (A and B) and annealing temperature. The net magnetic moment of spinel ferrite is the difference between magnetic moment of sites B and A which aligns anti parallel to each other [109].
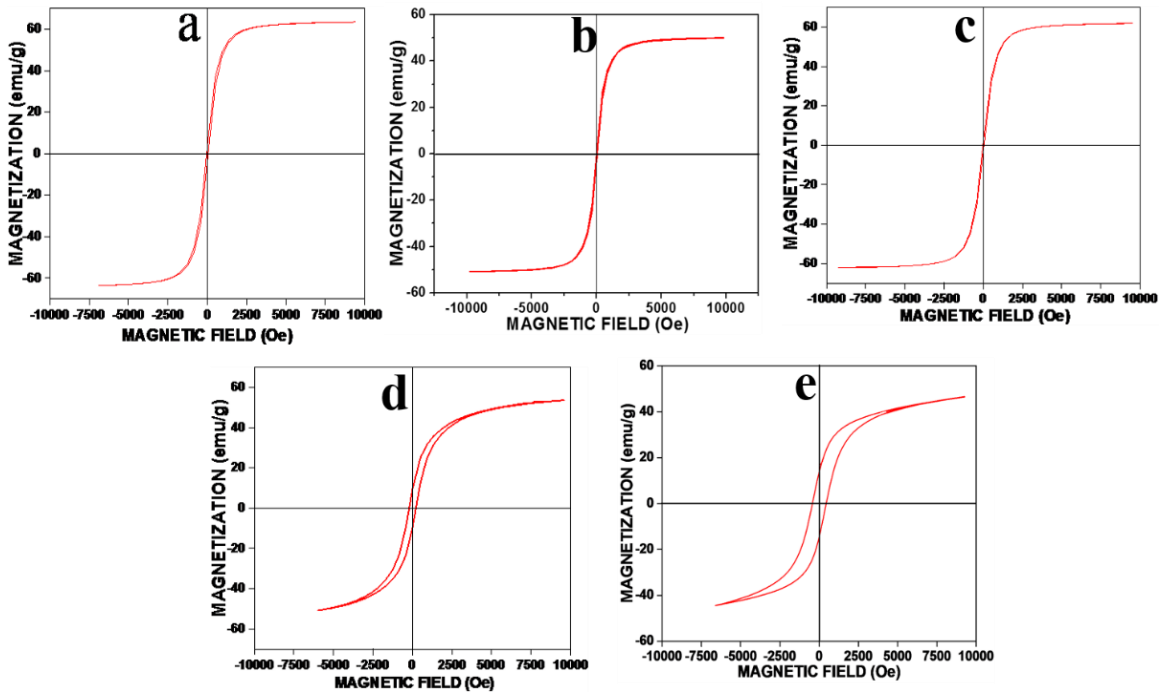
Figure 4.6: Hysteresis loops of $Ni_{0.6-x}Zn_{0.4}Co_xFe_2O_4$ (a) x = 0, (b) x = 0.0165, (c) x = 0.033, (d) x = 0.264 and (e) x = 0.528 at room temperature (300K).

Table 4.3. Saturation magnetization (M_s), Magnetic moment (M_μ), Retentivity (M_r), Coercivity (H_c), Squareness ratio (M_r/M_s) and Magneto crystalline anisotropy (K) measured from VSM.

x(Co doping)	D (nm)	M_s (emu/g)	$M_\mu(\mu_B)$	M_r (emu/g)	H_c (Oe)	M_r/M_s	K (erg/cm³)
0.000	23	63.52	2.696	3.68	49.94	0.058	1586
0.0165	20	50.49	2.143	2.61	45.63	0.051	1151
0.033	22	61.97	2.630	2.54	35.98	0.041	1115
0.264	23	51.95	2.205	9.56	215.92	0.184	5609
0.528	27	45.46	1.930	14.14	436.79	0.311	9930

In previous study (chapter-3), it is found that when samples annealed at low temperature (700°C) the M_s increases with Co doping because of Co^{2+} ions distribution in sites B.   Presently, it is clearly seen that when samples annealed at high temperature (1100°C), the value of M_s decreases with Co doping. This decrease in M_s value with doping is attributed to the distribution inversion of cations at high annealing temperature at different sub-lattices having different magnetic moments. The M_s value at x = 0 is higher when samples annealed at 1100°C then sample annealed at 700°C (chapter-3), since the cations distribution is same at both temperatures. The high value of M_s attributes to the increasing crystallinity, elimination of defects and impurity phase at high annealing temperature (1100°C) [143-144, 134-135]. Further, cations distributions are changed with Co doping when samples annealed at high annealing temperature. When Co doped at x = 0.0165 and 0.033 in Ni-Zn ferrite, all Co^{2+} ions occupy the sites A instead of sites B. As Co^{2+} ions occupy the sites A, Zn^{2+} ions get displaced from sites A to sites B. Consequently, the decrease in net magnetic moment occurs as discussed in section 4.3.1. But the large decrease in M_s at x = 0.0165 is attributed to the presence of secondary hematite phase with spinel phase structure [101]. When antiferromagnetic hematite phase ($\alpha-Fe_2O_3$) present with spinel phase cubic structure, spin canting effect take place which, decreases the total magnetic moment of the system. With the increasing doping (x = 0.264) concentration, more Co^{2+} ions distributed over sites A in place of Zn^{2+} ions and small fraction in sites B in place of Ni^{2+} ions. Also concentration of Zn^{2+} ions increases in sites B in place of Ni^{2+} ions as discussed in section 4.3.1. At high doping concentration (x = 0.528), carriers of Co^{2+} ions increase simultaneously in sites A and B whereas Zn^{2+} ions occupancy in sites B. By virtue of cations distributions effect, magnetic moment of sites B decreases and sites A increases with doping. Consequently, net magnetic moment decreases and thus M_s decreases with increasing Co doping concentration. The distribution of Co ions in sites A increase the total magnetic moment of sites A causing increase of super exchange interaction between sites B and A. The M_μ of $Ni_{0.6-x}Zn_{0.4}Co_xFe_2O_4$ nanoparticles was calculated [100] and listed in table 4.3. The value of M_r and H_c initially decreases up to x = 0.033 with respect to x = 0 and then increases with Co doping. The decreased value of M_r and H_c at x = 0.0165 and 0.033 at high annealing temperature (1100°C) attributes that all the Co^{2+} ions those occupy site A has minimum K value. The increased value of M_r and H_c attributes to positive K value of Co^{2+} ions in sites B that increases with increasing carrier concentration of Co^{2+} ions in

sites B (section 4.3.1). The calculated value of M_r/M_s of prepared samples lies between 0 and 0.5 which also confirms the magneto static interaction between the particles [145]. The K value of $Ni_{0.6-x}Zn_{0.4}Co_xFe_2O_4$ has been calculated [102] and tabulated in table 4.3. The obtained value of M_r, H_c and K at 1100°C annealed samples is lower than that obtained when samples annealed at 700°C (chapter-3). The obtained lower value is due to the inverse relation of H_c with M_s [146, 102, 134] and also due to increase of crystallinity and density of particles at high annealing temperature.

4.4 Theoretical analysis for cation distribution

In order to clarify the cations distribution in $Ni_{0.6-x}Zn_{0.4}Co_xFe_2O_4$ nanoparticles at high annealing temperature (1100°C), structural and magnetic properties have been also analyzed through theoretical calculations from most suitable proposed cations distribution.

4.4.1 Structural analysis

The theoretical value of a_{th} [103], r_A and r_B [104-106], u [107] and δ [106] were calculated from the proposed cations distribution and are listed in table 4.4. It is found that, the value of r_A continuously decreases while r_B continuously increases with Co doping. The decrease in r_A is due to replacement of larger size Zn^{2+}ions from sites A by smaller size Co^{2+} ions. The increase value of r_B possibly attributes to distribution of larger size Zn^{2+} and Co^{2+} ions in B sites in place of smaller size Ni^{2+} ions as discussed in experimental section. Theoretically calculated a_{th} follow the same trend as experimental a from XRD data and having good agreement with each other according to proposed cations distribution. The value of u continuously decreases with Co doping and is due to decrease in expansion of oxygen ion to accommodate the smaller Co^{2+} ions migrated from sites B to sites A and displacement of Zn^{2+} ions in sites B. The u value is slightly higher than that of ideal oxygen parameter ($u_{ideal} = 0.375Å$) because of deformation of unit cells in nanometer range [103, 106]. The u value gives the information regarding shifting in the position of oxygen ions with distribution of cations in A and B sites having different size [108]. The value of δ continuously decreases with Co doping.

Table 4.4. Proposed cations distribution [(**A1: $Zn_{0.4}Fe_{0.6}$, A2: $Co_{0.0165}Zn_{0.3835}Fe_{0.6}$, A3: $Co_{0.033}Zn_{0.367}Fe_{0.6}$, A4: $Co_{0.176}Zn_{0.224}Fe_{0.6}$, A5: $Co_{0.352}Zn_{0.048}Fe_{0.6}$**) and (**B1: $Ni_{0.6}Fe_{1.4}$, B2: $Zn_{0.0165}Ni_{0.5835}Fe_{1.4}$, B3: $Zn_{0.033}Ni_{0.567}Fe_{1.4}$, B4: $Zn_{0.176}Co_{0.088}Ni_{0.336}Fe_{1.4}$, B5: $Zn_{0.352}Co_{0.176}Ni_{0.072}Fe_{1.4}$**)], mean ionic radii of tetrahedral site (r_A), mean ionic radii of octahedral site (r_B), theoretical lattice constant (a_{th}), experimental lattice constant (a), oxygen parameter (u) and inversion parameter (δ).

x	Cation Distribution Site A	Cation Distribution Site B	r_A (Å)	r_B (Å)	a_{th} (Å)	a (Å)	u (Å)	δ (Å)
0.0000	A1	B1	0.730	0.676	8.4786	8.3608	0.3895	0.0145
0.0165	A2	B2	0.728	0.677	8.4782	8.3492	0.3894	0.0144
0.0330	A3	B3	0.726	0.678	8.4778	8.3451	0.3893	0.0143
0.2640	A4	B4	0.716	0.689	8.4917	8.3523	0.3884	0.0134
0.5280	A5	B5	0.703	0.707	8.5197	8.3560	0.3870	0.0120

4.4.2 Magnetic analysis

On the basis of proposed cations distribution, theoretical N_μ of $Ni_{0.6-x}Zn_{0.4}Co_xFe_2O_4$ nanoparticles at high annealing temperature is calculated from Neel's two sub lattices model of ferrimagnetism [99, 109] and is tabulated in table 4.6. The calculated N_μ follows the same trend as M_s and M_μ obtained from VSM study. The effect of cations distribution on the overall strength of magnetic interactions; A-B, A-A and B-B interaction with doping has been analyzed. The strength of magnetic interaction is inversely proportional to interatomic distance between metals cations (bond length) and directly proportional to bond angles [110] as discussed in chapter 3. The strength of A-B and A-A magnetic interaction are directly proportional to θ_1, θ_2 and θ_5 while B-B interactions are directly proportional to θ_3 and θ_4 [110, 112]. The interatomic distance between cation-cation (**b-f**), cation-anion (**p-s**) and bond angles (θ_1, θ_2, θ_3, θ_4 and θ_5) has been calculated [111-112] and are listed in table 4.5 and 4.6 respectively. Theoretically, it is found that the cation-cation (**b-f**) interatomic distance first decrease up to x = 0.033 and then increase with Co doping. The decrease value of cation-cation (**b-f**) interatomic distance attributes to the distribution of all smaller size Co^{2+} ions in tetrahedral sites (A) in place of larger size Zn^{2+} ions. The cation-anion interatomic distance **p** first decrease at x = 0.0165 and then increase with Co doping. While the value of **q**, **r** and **s** decrease with Co doping.

Table 4.5. Cation-cation (*b, c, d, e, f*) and cation-anion (*p, q, r, s*) for $Ni_{0.6-x}Zn_{0.4}Co_xFe_2O_4$ nanoparticles.

x	*b* (Å)	*c* (Å)	*d* (Å)	*e* (Å)	*f* (Å)	*p* (Å)	*q* (Å)	*r* (Å)	*s* (Å)
0.0000	2.9555	3.4655	3.6202	5.4303	5.1000	1.9681	2.0214	3.8702	3.6906
0.0165	2.9514	3.4607	3.6152	5.4228	5.0930	1.9665	2.0168	3.8613	3.6849
0.0330	2.9499	3.4590	3.6134	5.4201	5.0905	1.9666	2.0139	3.8558	3.6825
0.2640	2.9525	3.4620	3.6165	5.4248	5.0949	1.9759	2.0025	3.8339	3.6813
0.5280	2.9538	3.4635	3.6181	5.4272	5.0971	1.9879	1.9841	3.7986	3.6764

The increase value of *p* attributes to migration of larger size Zn^{2+} ions in sites B with doping. The decrease value of *q*, *r* and *s* is due to the replacement of larger size Zn^{2+} ions by smaller size Co^{2+} ions in sites A as discussed in experimental section. The values of θ_1, θ_2 and θ_5 increase with Co doping and values of θ_3, θ_4 decrease with Co doping. The increasing value of θ_1, θ_2 and θ_5 indicate the strengthening of A-B and A-A interaction while decreasing θ_3, θ_4 value indicates the weakening of B-B interaction. The increasing strength of A-B and A-A interaction with doping is due to the distribution of high magnetic moment Co^{2+} ions in place of diamagnetic Zn^{2+} ions in sites A as well as in sites B in place of Ni^{2+} ions. The decreasing strength of B-B is due to the migration of diamagnetic Zn^{2+} ions from sites A to sites B. Finally, to concluded, the calculated theoretical results have great agreement with the results obtained experimentally according to proposed cations distributions at high annealing temperature. Theoretical analysis of samples annealed at 700ºC and 1100ºC shows that the structural and magnetic properties of Co doped Ni-Zn ferrite nanoparticles directly depends on cations distribution in terms of annealing temperature.

Table 4.6. Bond angles (θ_1, θ_2, θ_3, θ_4, θ_5) between ions pairs and theoretically calculated magnetic moment (N_μ) for $Ni_{0.6-x}Zn_{0.4}Co_xFe_2O_4$.

x	θ_1 *(Degree)*	θ_2 *(Degree)*	θ_3 *(Degree)*	θ_4 *(Degree)*	θ_5 *(Degree)*	N_μ (μ_B)
0.0000	120.595	134.279	97.326	125.887	67.613	5.200
0.0165	120.635	134.424	97.255	125.873	67.710	5.117
0.0330	120.676	134.569	97.183	125.859	67.806	5.035
0.2640	120.960	135.599	96.685	125.761	68.490	4.408
0.5280	121.379	137.151	95.965	125.616	69.513	3.616

The relation between Co doping, D, M_s, H_c, K, r_A, r_B, M (A) and M (B) has been shown in figure 4.7. The D first decreases with Co doping and then increases at high concentration of Co doping (x = 0.528) as shown in figure.4.7. From figure 4.7, it was found that the value of M_s decreases with Co doping because of Co^{2+} ions distribution effect in A sites as well as Zn^{2+} ions distribution in sites B having different magnetic moment. It also shows that H_c is directly proportional to K energy. The variation in r_A, r_B, M (A) and M (B) with Co doping is also shown in figure 4.7 according to proposed cations distribution. Thus the values of D, M_s, Hc, K, r_A, r_B, M (A) and M (B) directly depends upon dopant cations as well as distribution of cations in sites A and B of spinel system. Moreover, it also been established that annealing temperature plays an important role in monitoring various structural and magnetic parameters.
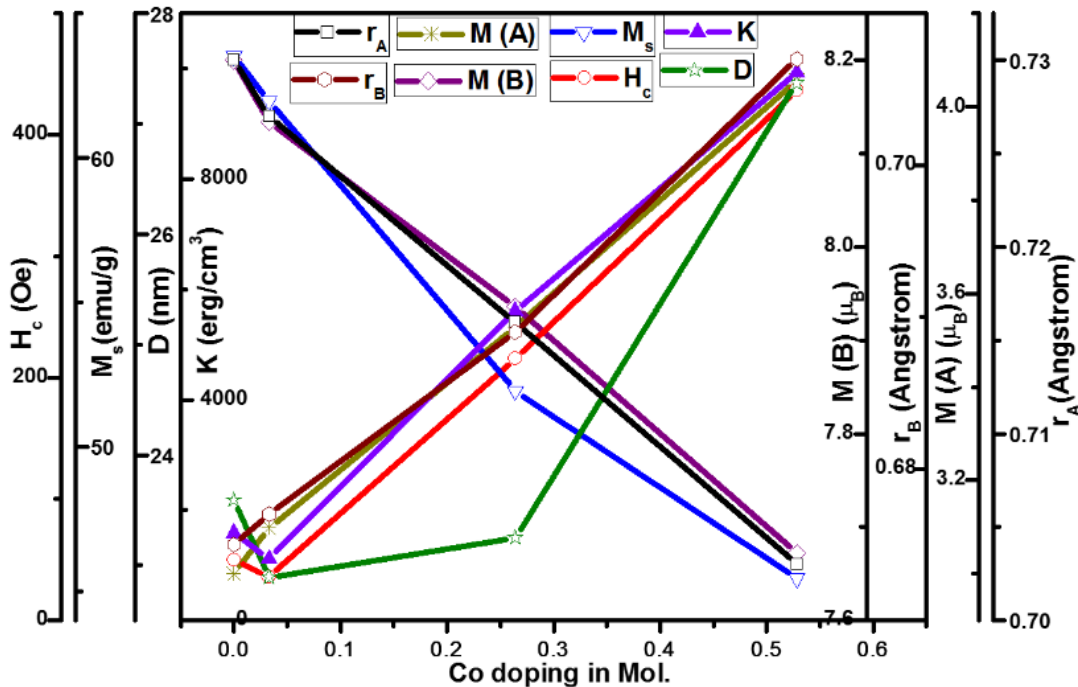
Figure. 4.7: Relationship between Co doping, crystallite (D) size, saturation magnetization (M_s), coercivity (H_c), magneto crystalline anisotropy (K), ionic radii of site A (r_A), ionic radii of site B (r_B), magnetic moment of site A (M (A)) and magnetic moment of site B (M (B)).

4.5 Conclusion

$Ni_{0.6-x}Zn_{0.4}Co_xFe_2O_4$ nanoparticles were successfully synthesized by sol gel method and annealed at 1100ºC. XRD study revealed the formation of single phase spinel cubic structure at x = 0, 0.033, 0.264 and 0.528 and there is partial formation of hematite (α-Fe_2O_3) at x = 0.0165 with

spinel phase. It is also found that when samples annealed at high temperature 1100°C, most of the hematite secondary phase diminished. The crystallite size (D) obtained from XRD lies in the nanometer range. The obtained crystallite size (D) at high annealing temperature is slightly smaller than samples annealed at 700°C. This is due to increase in crystallinity and density, removal of defects and impurity phase at high annealing temperature. The decreasing values of d-spacing (d) and lattice constant (a) by means of Co doping (x = 0.033) aspect to the lattice shrinkage caused by the distribution of all Co^{2+} ions in tetrahedral (A) sites in place of Zn^{2+} ions. The negative slop of linear fitted W-H plots indicates that annealed samples at 1100°C have compressive strain present in nanoparticles. The saturation magnetization (M_s) of undoped Ni-Zn ferrite nanoparticles is high when samples annealed at high temperature. This is also due to increase in crystallinity and density, removal of defects and impurity phase at high annealing temperature. The decrease in value of saturation magnetization (M_s) with Co doping attributes to the effect of Co^{2+} ions distribution in tetrahedral (A) sites and equivalent Zn^{2+} ions in octahedral (B) sites having different magnetic moment. Consequently, net magnetic moment decreases and decrease in saturation magnetization (M_s) is also observed. The large decreased value of saturation magnetization (M_s) at x = 0.0165 than at x = 0.033 attributed to Co^{2+} ions distribution in tetrahedral (A) sites and also due to antiferromagnetic hematite (α-Fe_2O_3) phase effect. The values of retentivity (M_r), coercivity (H_c) and magneto crystalline anisotropy energy (K) first decrease with Co doping up to x = 0.033 and then increases with Co doping. The decreased value is attributed to the Co^{2+} ions distribution in Site A having minimum magneto crystalline anisotropy energy (K). As concentration of Co^{2+} ions increases in sites B with Co doping, these values increases because of positive magneto crystalline anisotropy energy (K) of Co^{2+} ions in sites B. The value of coercivity (H_c) is directly proportional to magneto crystalline anisotropy energy (K) and also depends upon distribution of types of cations in different sites and annealing temperature. The theoretically obtained results of lattice constant (a_{th}), Neel magnetic moment (N_μ) and other parameters calculated from proposed cations distribution have good agreement with results obtained from experimental data. Finally, to conclude, the structural and magnetic properties of spinel ferrite nanoparticle depend upon synthesis method, annealing temperature, distribution of types of cations in sites A and B and dopant concentration. The moderate M_s and

low H_c values of all prepared samples attributes that these materials can be useful for magnetic recording devices.

CHAPTER-5

DEVELOPMENT OF Co DOPED Ni-Zn FERRITE NANOPARTICLES BY NON-AQUEOUS METHOD AND THEIR STRUCTURAL AND MAGNETIC PROPERTIES STUDIES

5.1 Introduction

In last few decades' synthesis of spinel ferrites nanoparticles have been great interest to make a materials have excellent chemical stability, high product purity, high crystallinity, high saturation magnetization, low coercivity, high permeability, high resistivity and low eddy current losses. Among the spinel ferrites, Ni-Zn ferrites are the most important magnetic materials from commercial point of view by virtue of its properties [56, 119] and used in many application [147-150]. The properties of Ni-Zn ferrites nanoparticles are highly sensitive to their preparation techniques, annealing temperature and distributions of cations in tetrahedral (A) and octahedral (B) sites respectively. In literature, reported Ni-Zn ferrite nanoparticles have been prepared by many different methods such as *sol-gel* method, hydrothermal method, citrate precursor method, co-precipitation method, reverse micelle method, micro-emulsion method, sonochemical reaction method, etc. [151-156, 74, 47] and found different structural and magnetic properties. The properties of Ni-Zn ferrites nanoparticles can further be improved by doping [55, 117-118].

In the previous study Co doped Ni-Zn ferrite nanoparticles have been synthesized by sol gel method and annealed at $700^{o}C$ and $1100^{o}C$ (chapter-3, chapter-4) [64, 133]. Co has been introduced in Ni-Zn ferrite system in order to improve the magnetic properties. The variation in structural and magnetic properties in previous study has been explained on the basis of cations distribution and annealing temperature. In the present study, new method i.e. non-aqueous method has been developed in order to prepare the undoped and Co doped Ni-Zn ferrite. The previous method is the best method for the preparation of spinel ferrites nanoparticles but has some disadvantages such as complicated and long procedure methods, long reaction time, high reaction temperature, use of complexing agent and pH adjustment. In the new developed non-aqueous method, spinel ferrites nanoparticles can be prepared without using any complexing agent. The reaction temperature in this method is very low. Also ferrite nanoparticles can be prepared in short duration as compared to other complexing methods. Moreover, this is very simple method, cost effective and multicomponent system nanoparticles can be prepared by this method. Because of its advantages, undoped and Co doped Ni-Zn ferrites nanoparticles with distinct composition has been synthesized by non-aqueous method. The effect of Co doping on structural and magnetic properties has been discussed for new developed non-aqueous method in terms of cations distribution in different sub lattices. The nanoparticles prepared by non-aqueous

method are highly crystalline in nature, have high saturation magnetization and low value of coercivity which can be useful in targeted drug delivery, hyperthermia, MRI, EMI shielding and magnetic recording device applications.

5.2. Experimental details

5.2.1. Synthesis of $Ni_{0.6-x}Zn_{0.4}Co_xFe_2O_4$ nanoparticles by non-aqueous method.

Nanoparticles of $Ni_{0.6-x}Zn_{0.4}Co_xFe_2O_4$ (x = 0, 0.033, 0.066, 0.132, 0.264 and 0.528) have been prepared by new direct method. Nickel nitrate hexahydrate (Ni $(NO_3)_2.6H_2O$), zinc nitrate hexahydrate (Zn $(NO_3)_2.6H_2O$), cobalt nitrate hexahydrate (Co $((NO_3)_2.6H_2O$) and ferric nitrate nonahydrate (Fe $(NO_3)_3.9H_2O$) were used as precursor materials to prepare the nanoparticles. Acetone was used as a solvent. The appropriate amounts of Nickel nitrate hexahydrate (Ni $(NO_3)_2.6H_2O$), zinc nitrate hexahydrate (Zn $(NO_3)_2.6H_2O$), cobalt nitrate hexahydrate (Co $((NO_3)_2.6H_2O$) and ferric nitrate nonahydrate (Fe $(NO_3)_3.9H_2O$) have been dissolved in acetone under magnetic stirring for 30 minutes. The reaction was performed at 50^oC with continuous stirring until the solution changed into paste. Finally, prepared paste was annealed at 1100^oC for five hours and desired $Ni_{0.6-x}Zn_{0.4}Co_xFe_2O_4$ nanoparticles have been formed. The schematic diagram of non-aqueous method is shown in figure 5.1. The chemical reaction of non-aqueous method is given below.

$$(0.6 - x)Ni(NO_3)_2.6H_2O + (0.4)Zn(NO_3)_2.6H_2O + (x)Co(NO_3)_2.6H_2O + 2Fe(NO_3)_3.9H_2O + (CH_3)_2CO$$
$$\underset{\Delta}{\Rightarrow} Ni_{0.6-x}Zn_{0.4}Co_xFe_2O_4 + 2N_2\uparrow + CO_2\uparrow + H_2\uparrow + 6O_2\uparrow + 23H_2O + 4NO_2 + 2CH_3OH$$
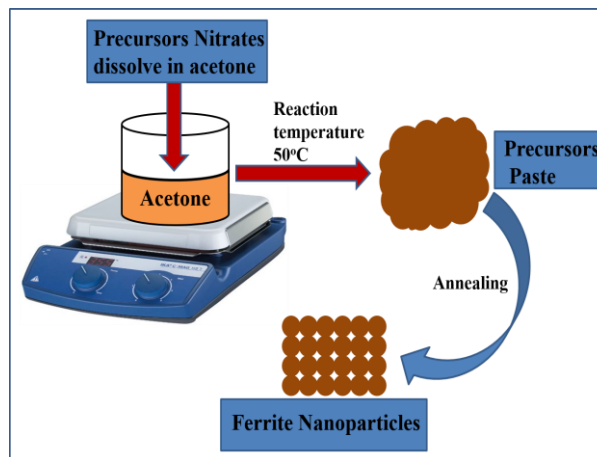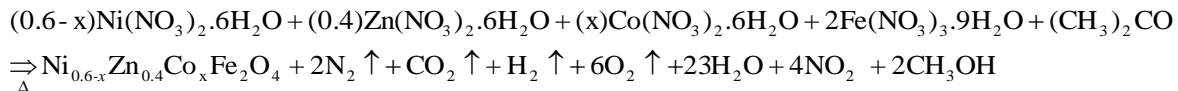
Figure 5.1: Schematic diagram of *sol-gel* method to synthesize $Ni_{0.6-x}Zn_{0.4}Co_xFe_2O_4$ nanoparticles.

5.2.2 Characterization

Prepared $Ni_{0.6-x}Zn_{0.4}Co_xFe_2O_4$ samples were characterized by Shimadzu-6000 XRD using Cu-Kα ($\lambda = 1.546°A$) radiation for phase identification, measurement of crystallite size and other structural parameters. Morphology and elemental analysis of the prepared samples were observed by Carl Zeiss Modal No-Ultra Plus-55 FESEM and Oxford Instruments EDX respectively. The effect of Co doping on the magnetic properties of Ni-Zn ferrite has been examined by PAR-155 VSM in a magnetic field range from −10 KOe.to +10 KOe.

5.3 Results and discussion

5.3.1 Structural analysis

The structural analysis of prepared samples has been carried out by powder XRD technique and the patterns are presented in figure 5.2. All the indexed peaks confirm the formation of single phase spinel cubic structure in all prepared samples. There is no evidence of any other impurity phase in the XRD spectra. The diffraction peaks have good agreement with standard JCPDS card no.52-0277 corresponding to spinel Ni-Zn ferrite. No other peaks corresponding to Co indicate that Co^{2+} ions are properly distributed in Ni-Zn ferrite spinel system. The sharp peaks in XRD spectra show that samples prepared by non-aqueous method are high crystalline in nature as compared to nanoparticles prepared by *sol-gel* method.
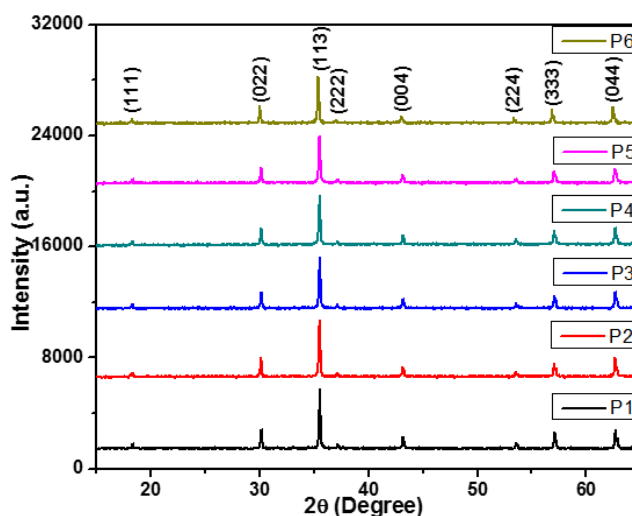
Figure 5.2: XRD spectra of $Ni_{0.6-x}Zn_{0.4}Co_xFe_2O_4$ (P1 (x = 0), P2 (x = 0.033, P3 (x = 0.066), P4 (x = 0.132), P5 (x = 0.264) and P6 (x = 0.528)).

The D of prepared samples have been calculated using Scherer's formula [64, 94, 133] from most prominent peak (113) of XRD and values are tabulated in table 5.1. The D value and other structural parameters like d and a of Ni-Zn ferrites nanoparticles system depends on synthesis methods and annealing temperature [157-165, 91, 67, 73-74, 76, 79]. The D value of samples prepared by non-aqueous method are found in the range of 51.61 to 59.39 nm with Co doping and larger than the nanoparticles prepared by *sol-gel* method (chapter-3, chapter-4) [64, 133]. This is because D depends on synthesis methods and annealing temperature.

The variation in D value with Co doping prepared by *sol-gel* method was explained in terms of distribution of cations. The distribution of cations in samples prepared by *sol-gel* method [chapter-4] is different from samples prepared by non-aqueous method because distribution of cations in spinel ferrites nanoparticles depends on synthesis methods and annealing temperature [124, 126-129]. Normally in bulk form Zn^{2+} cations occupied the sites A but in nano reign there is possibility of inversion in sites B [166-167, 120-123, 64]. In the present study, D value initially increase at x = 0.033, then decrease at x = 0.066 and further increases with Co doping.

This variation in D has also been explained on the basis of distribution of cations in sites A and B of spinel system, which depends on synthesis methods and annealing temperature [124, 126-129]. The increased D at x = 0.033 is due to the enlargement of unit cells caused by distribution of larger size Co^{2+} ions in sites B in place of smaller size Ni^{2+} ions (Chapter-3). Co^{2+} ions have strong tendency to occupy the sites B but partial inversion in sites A is possible (Chapter-4) [64, 136-138]. When Co doped at x = 0.066, larger fraction of Co^{2+} ions go to sites A and smaller fraction in sites B. With this distribution of Co^{2+} ions in sites A, some of the Zn^{2+} ions migrate from sites A to sites B in place of Fe^{3+} ions. Also some of the Fe^{3+} ions migrate from sites B to sites A in place of Zn^{2+} ions to maintain the neutrality of spinel system. The distribution of smaller size Co^{2+} and Fe^{3+} (ionic radii = 0.67 Å) ions in sites A in place of larger size Zn^{2+} ions resulting to shrinkage in unit cells that cause D decrease. The increased value of D with doping after x = 0.066 is possibly attributed to the increasing concentration of Co^{2+} ions in sites B in place of smaller size Ni^{2+} ions and less occupancy of Co^{2+} ions in sites A resulting to enlargement in unit cells that causes increment in D.

Further structural parameters like d [95] and a [96] have been calculated and presented in table 5.1. It is found that d and a value of undoped Ni-Zn ferrite nanoparticles prepared by non-aqueous method is slightly larger than the nanoparticles prepared by *sol-gel* method [chapter-3,

chapter-4]. This slight difference is due the route of preparation. The calculated value of d and a prepared by non-aqueous method first increase at x = 0.033 then decrease at x = 0.066 and further increases with Co doping. The increase value of d and a at x = 0.033 possibly attributed to the distribution of larger size Co^{2+} ions in sites B in place of smaller size Ni^{2+} ions that cause expansion in lattices. The reduced value of d and a at x = 0.066 suggested the distribution of large fraction of smaller size Co^{2+} and Fe^{3+} (ionic radii = 0.67 Å) ions in sites A in place of larger size Zn^{2+} (ionic radii = 0.82 Å) ions and that cause lattices shrinkage. Further increment in d and a after x = 0.066 doping is due to decrease in inversion of Co^{2+}, Zn^{2+} and Fe^{3+} cations in sub lattices and increasing concentration of Co^{2+} ions in Ni-Zn ferrite system. The value of a shows nonlinear behavior with Co doping which, indicate the violation of Vegards's law. This nonlinear behavior of a value with Co doping possibly attributed to the inversion of cations or their deviation from its normal spinel preference distribution [105, 100]. Also the strain in nanoparticles has been calculated using Stocks-Wilson equation [97]. It is found that the prepared nanoparticles by non-aqueous method have smaller strain as compared to nanoparticles prepared by *sol-gel* method. The minimum strain present in nanoparticles is due larger D size and no impurity phase present in nanoparticles when prepared by non-aqueous method.

Table 5.1. Crystallite size (D), d-spacing (d), lattice constant (a) and strain (ε) calculated from prominent peak (113) of XRD; crystallite size (W-H D) calculated from Williamson-Hall plots.

x (Co doping)	D (nm)	d (Å)	a (Å)	ε	W-H D (nm)
0.000	52	2.5233	8.3689	0.00204	52
0.033	53	2.5254	8.3759	0.00197	42
0.066	51	2.5239	8.3709	0.00218	53
0.132	53	2.5248	8.3739	0.00195	50
0.264	56	2.5254	8.3758	0.00191	50
0.528	59	2.5329	8.4008	0.00179	52

Also W-H D and types of ε present in nanoparticles have been estimated using Williamson-Hall (W-H) method [98] and values of W-H D being tabulated in table 5.1. The W-H plots of prepared samples are shown in figure 5.3. The estimated W-H D from Williamson-Hall (W-H) plots are approximately equivalent to that calculated using Scherrer's formula and found in nm range.
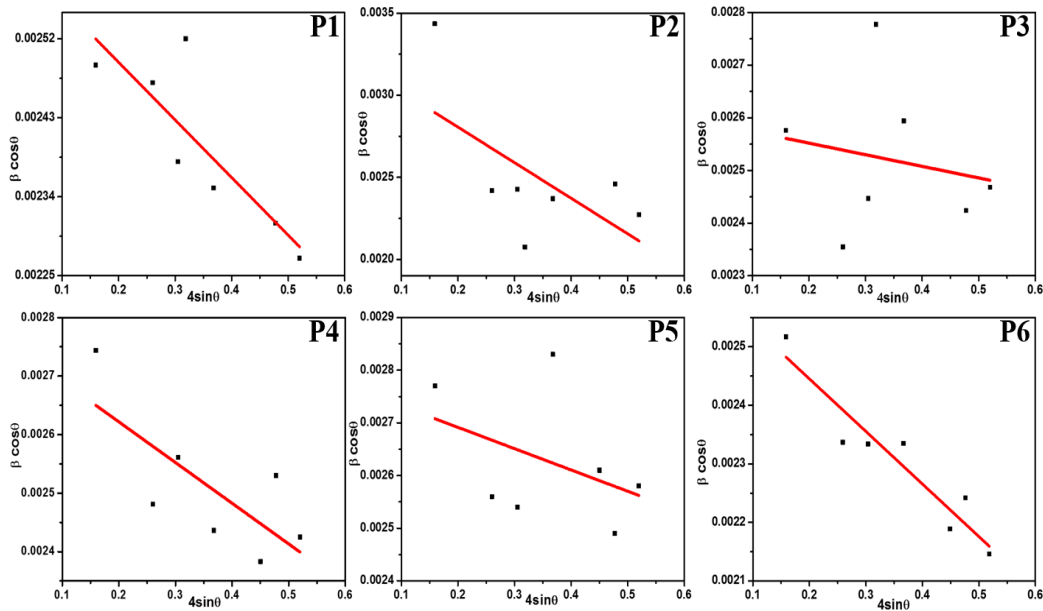
Figure 5.3: W–H plots of $Ni_{0.6-x}Zn_{0.4}Co_xFe_2O_4$ (P1) x = 0, (P2) x = 0.033, (P3) x = 0.066, (P4) x = 0.132, (P5) x = 0.264 and (P6) x = 0.528.

The linear fitted W-H plots of all prepared samples show negative slope which indicate the presence of compressive strain [141-142]. In the previous study, it was also found that samples prepared by *sol-gel* method and annealed at 1100°C show the presence of compressive strain in the system. The compressive strain present in the nanoparticles is due to high annealing temperature effect which reduced the stress and porosity and increased the density of nanoparticles.

5.3.2 FESEM-EDX Characterizations

The prepared samples have been employed to FESEM for morphological examination and FESEM micrographs of prepared samples at x = 0, 0.132 and 0.528 are shown in figure 5.4. The FESEM micrographs show uniform grain distribution as compared to previously synthesized samples by *sol-gel* method (chapter-3, chapter-4) [64, 133]. Figure 5.4 shows that morphology of samples that is very similar to each other with agglomeration of nanoparticles. The agglomeration in prepared samples is possibly attributed to the magnetic nature of nanoparticles [168]. The agglomeration of nanoparticles in samples increases with doping as seen in micrograph because of high magnetic moment of Co^{2+} ($3\mu_B$) ions as compared to replaced Ni^{2+} ions ($2\mu_B$) which

increase the interaction between nanoparticles. It is also found that samples prepared by non-aqueous method are highly crystalline in nature.
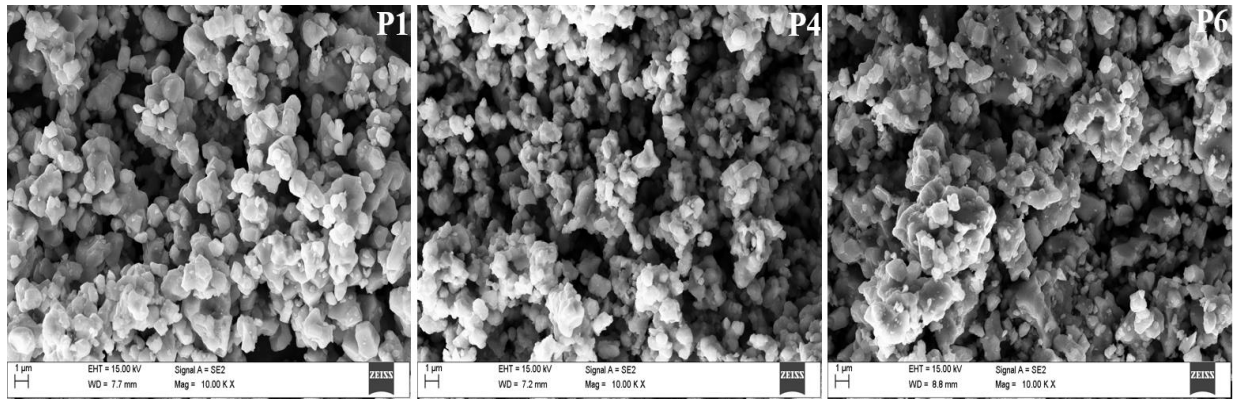
Figure 5.4: FESEM Micrographs of $Ni_{0.6-x}Zn_{0.4}Co_xFe_2O_4$ (P1) x = 0, (P4) x = 0.132 and (P6) x = 0.528.

The prepared spinel ferrite nanoparticles were further characterized by EDX for stoichiometry. The EDX spectra's of $Ni_{0.6-x}Zn_{0.4}Co_xFe_2O_4$ nanoparticles at x = 0, 0.132 and 0.528 are being shown in figure 5.5.
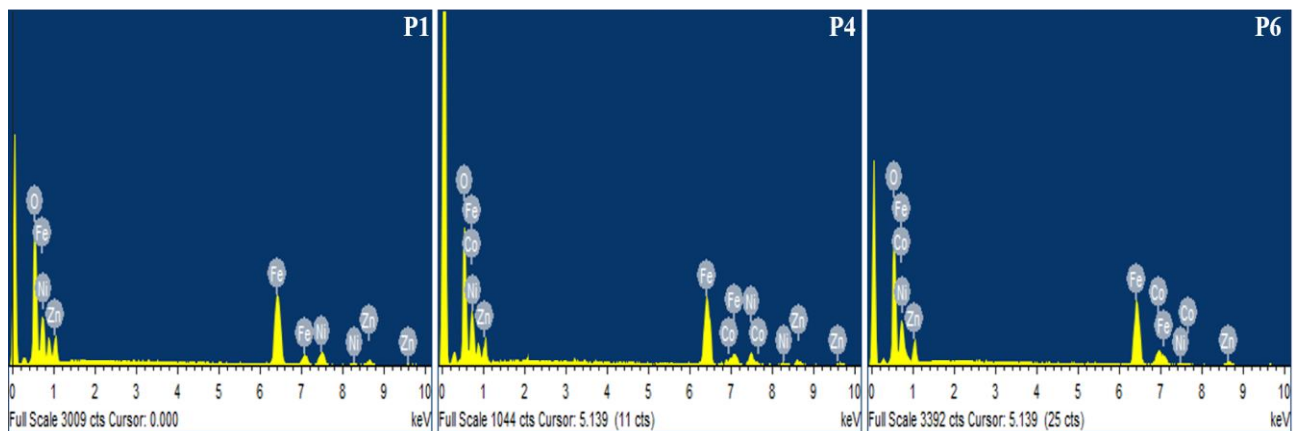
Figure 5.5: EDX micrographs of $Ni_{0.6-x}Zn_{0.4}Co_xFe_2O_4$ (P1) x = 0, (P4) x = 0.132 and (P6) x = 0.528.

The EDX results revealed that in prepared samples all elements are found in defined and expected ratio. Also peaks of Co at x = 0.132 and 0.528 in EDX spectra indicates that doped Co^{2+} ions are present in Ni-Zn ferrite system. The atomic percentage of elements present in prepared nanoparticles systems are tabulated in table 5.2. On the basis of these findings, it was concluded that the samples prepared by non-aqueous method attain good stoichiometry.

Table 5.2. Atomic percentage (At. %) of $Ni_{0.6-x}Zn_{0.4}Co_xFe_2O_4$ at x = 0, 0.033 and 0.264 obtained from EDX measurement.

x	O (At. %)	Fe (At. %)	Ni (At. %)	Zn (At. %)	Co (At. %)
0.000	55.62	28.70	8.97	6.71	0
0.033	58.12	29.13	6.80	5.69	0.26
0.264	55.29	30.05	4.37	6.67	3.62

5.3.3 Magnetic properties measurement

The magnetic measurements of prepared $Ni_{0.6-x}Zn_{0.4}Co_xFe_2O_4$ nanoparticles have been performed using VSM at room temperature. Figure 5.6 shows the M-H curve of prepared samples.
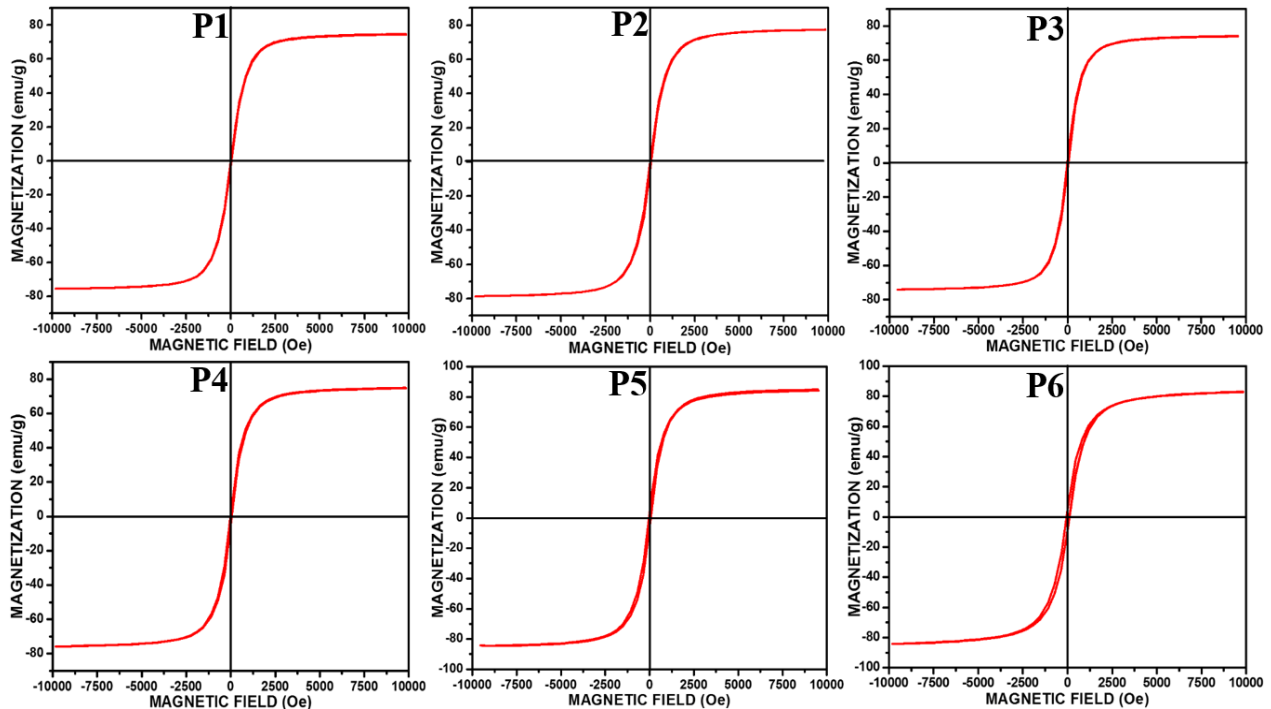
Figure 5.6: Hysteresis loops of $Ni_{0.6-x}Zn_{0.4}Co_xFe_2O_4$ (P1) x = 0, (P2) x = 0.033, (P3) x = 0.066, (P4) x = 0.132, (P5) x = 0.264 and (P6) x = 0.528 at room temperature (300K).

VSM results revealed that all prepared samples are ferrimagnetic in nature contains small values of M_r and H_c. The magnetic properties of spinel ferrite nanoparticles are strongly influenced by distribution of cation in different sub-lattices which depends on synthesis methods and annealing temperature [126-129. 64, 133]. The reported Ni-Zn ferrites nanoparticles have been synthesized by different methods and shows different magnetic behavior [157-165, 91 67,

73-74, 76, 79]. The M_s value of all prepared samples is found in the 75.07 emu/g to 84.42 emu/g range and listed in table 5.3. The M_s value of undoped Ni-Zn nanoparticles prepared by non-aqueous method is higher than that of the samples prepared by *sol-gel* method (chapter-4) while the cations distribution is same. The high M_s value of samples prepared by non-aqueous method is possibly attributed to larger D, high crystallinity, uniform morphology of samples [158, 163, 67, 73] and due to pure spinel phase. Further variation in M_s value with doping has been explained in terms of distribution of cations in different sub lattices having different moment. When Co doped at x = 0.033, M_s increase. The increased value of M_s is due to the high magnetic moment Co^{2+} ions which replace the low magnetic moment Ni^{2+} ions in sites B. Consequently, net magnetic moment and M_s of the system increase. When Co doped at x = 0.066, larger fraction of Co^{2+} ions go to sites A and smaller fraction in sites B. With this distribution of Co^{2+} ions in sites A, some of the nonmagnetic Zn^{2+} ions migrate from sites A to sites B. Also some of the Fe^{3+} ions migrate from sites B to sites A. Due to the distribution of high magnetic moment Co^{2+} and Fe^{3+} ions in place of nonmagnetic Zn^{2+} ions, total magnetic moment of sites A increase. Also with the migration of Fe^{3+} ions in sites A, site B magnetic moment is decrease. Consequently, net magnetic moment and M_s is decreased. Further x > 0.066, M_s value continuously increased up to x = 0.264 and then slightly decreased at x = 0.528. The increased value of M_s up to x = 0.264 is due to increasing concentration of Co^{2+} in sites B and decreasing occupancy in sites B causes sites B magnetic moment and net magnetic moment increase. At high doping concentration (x = 0.528), amount of Co^{2+} ions increase in sites A as compared to other composition and larger number of Co^{2+} ions distributed over sites B in place of Ni^{2+} ions. Also with the distribution of Co^{2+} ions in sites A, equivalent amount of Zn^{2+} ions occupied the sites B. Because of this, total sites A magnetic moment slightly increased and sites B magnetic moment slightly decreased cause net magnetic moment and M_s is slightly decreased as compared to x = 0.264. The value of M_r and H_c continuously increased with Co doping. The value of M_r and H_c depends on magneto crystalline anisotropy energy (K) and L-S coupling [169].

　　　　H_c value also depends on size of particles and magnetization [137]. The H_c value of samples prepared by non-aqueous method at x = 0 is smaller than samples synthesized by *sol-gel* method. This is because of inverse relation of H_c with particle size and magnetization [137, 146, 102, 134]. Further increased value of M_r and H_c with doping is due to distribution of Co^{2+} ions in sites B having positive K [102]. As the doping concentration increases, concentration of Co^{2+}

ions also increased in sites B that is responsible for increment in M_r and H_c values. The values of M_r and H_c are presented in table 5.3. The increment in K value with Co doping has been calculated [102] and presented in table 5.2. The M_r/M_s value has been calculated [25] and found continuously increased with doping and being presented in table 5.3. The very small M_r/M_s value of prepared samples by non-aqueous method indicates the magneto static interaction between the particles [145] and isotropic nature of nanoparticles. The M_μ value of prepared $Ni_{0.6-x}Zn_{0.4}Co_xFe_2O_4$ nanoparticles have also been calculated [100] and listed in table 5.3.

Table 5.3. Saturation magnetization (M_s), magnetic moment (M_μ), retentivity (M_r), coercivity (H_c), squareness ratio (M_r/M_s) and magneto crystalline anisotropy (K) measured from VSM.

x	D (nm)	M_s (emu/g)	$M_\mu(\mu_B)$	M_r (emu/g)	H_c (Oe)	M_r/M_s	K (erg/cm³
0.000	52	75.17	3.190	1.23	21.04	0.0163	790.78
0.033	53	77.85	3.304	2.24	27.97	0.0287	1088.73
0.066	51	73.94	3.138	2.70	31.28	0.0365	1156.42
0.132	53	75.07	3.186	3.67	42.90	0.0488	1610.25
0.264	56	84.42	3.584	5.64	59.90	0.0668	2528.37
0.528	59	83.72	3.555	7.48	88.78	0.0893	3716.33

5.4 Theoretical analysis for cation distribution

The confirmation of deviation in structural and magnetic properties of nanoparticles prepared by non-aqueous method have been done theoretically from most suitable proposed cations distribution.

5.4.2 Structural analysis

The most suitable proposed cations distributions are listed in table 5.4. From proposed cations distribution, theoretical a_{th} [103] has been calculated using r_A and r_B [104-106] and tabulated in table 5.4. Also u [107] and δ [106] were calculated and presented in table 5.4. According to most suitable proposed cations distributions, doped Co^{2+} ions are distributed over A and B sites at some composition and migrate the Zn^{2+} and Fe^{3+} ions from its preferential sites as discussed in experimental section. The theoretical a_{th} calculated from most suitable proposed cations distribution follows the same trend as experimental a varies.

The theoretically calculated a_{th} have great agreement with results of experimental a according proposed cation distribution. The calculated u value is slightly higher than that of ideal oxygen parameter ($u_{ideal} = 0.375Å$) because of deformation of unit cells in nanometer range [103, 106]. The variation in u value with doping possibly attributes to expansion and shrinkage of sites B and sites A by virtue of distribution of different size cations. The δ value first decrease with Co doping up to x = 0.066, then increase up to x =0.264 and lastly decrease at x = 0.528. This variation in δ value with doping possibly attributes to distribution of cations in different sub lattices having different radii.

Table 5.4. Proposed cations distribution [(**A1: Zn$_{0.4}$Fe$_{0.6}$, A2: Zn$_{0.4}$Fe$_{0.6}$, A3: Zn$_{0.26}$Co$_{0.05}$Fe$_{0.69}$, A4: Zn$_{0.35}$Co$_{0.03}$Fe$_{0.62}$, A5: Zn$_{0.38}$Co$_{0.02}$Fe$_{0.6}$, A6: Zn$_{0.33}$Co$_{0.07}$Fe$_{0.6}$) and (B1: Ni$_{0.6}$Fe$_{1.4}$, B2: Ni$_{0.567}$Co$_{0.033}$Fe$_{1.4}$, B3: Ni$_{0.534}$Zn$_{0.14}$Co$_{0.016}$Fe$_{1.31}$, B4: Ni$_{0.468}$Zn$_{0.05}$Co$_{0.102}$Fe$_{1.38}$, B5: Ni$_{0.336}$Zn$_{0.02}$Co$_{0.244}$Fe$_{1.4}$, B6: Ni$_{0.072}$Zn$_{0.07}$ Co$_{0.458}$Fe$_{1.4}$)]**, ionic radii of tetrahedral site (r_A), ionic radii of octahedral site (r_B), theoretical lattice constant (a_{th}), experimental lattice constant (a), oxygen parameter (u) and inversion parameter (δ).

x	*Cation Distribution Site A*	*Cation Distribution Site B*	r_A (Å)	r_B (Å)	a_{th} (Å)	a (Å)	u (Å)	δ (Å)
0.000	A1	B1	0.7300	0.6760	8.4786	8.3689	0.38959	0.01459
0.033	A2	B2	0.7300	0.6769	8.4810	8.3759	0.38955	0.01455
0.066	A3	B3	0.7127	0.6864	8.4797	8.3709	0.38840	0.01340
0.132	A4	B4	0.7274	0.6822	8.4870	8.3739	0.38909	0.01409
0.264	A5	B5	0.7285	0.6840	8.4977	8.3758	0.38918	0.01418
0.528	A6	B6	0.7247	0.6931	8.5161	8.4008	0.38862	0.01362

5.4.3 Magnetic analysis

The N_μ value of all prepared samples has also been calculated from Neel's two sub lattices model of ferrimagnetism [109, 99]. The values of N_μ were also calculated on the basis of proposed cations distribution by taking mean magnetic moment difference of B and A sites respectively and are tabulated in table 5.6. It is found that the calculated value of N_μ first increase at x = 0.033, then decreased at x = 0.066 and then further increased up to x = 0.264 doping concentration. Lastly at high doping concentration (x = 0.528), N_μ slightly decreased compared to x = 0.264. The calculated value of N_μ follow the same trend as observed experimentally for M_s and M_μ. Finally, N_μ have good agreement with experimental M_s and M_μ data according to

proposed cations distribution. Also the effect of Co doping on A-B, A-A and B-B magnetic interaction has been theoretically analyzed. A-B interactions are the strongest interaction of spinel system that hold the spins of different sites in particular direction and that depend on the distribution of cations having different magnetic moment. The strength of interactions in spinel nanoparticles system varies inversely for bond length and directly with bond angles [110]. The interatomic distance between cation-cations (*b-f*) and cation-anion (*p-s*) has been calculated [111] and are tabulated in table 5.5. Using cation-cation (*b-f*) and cation-anion distance (*p-s*), the bond angles $\theta_1, \theta_2, \theta_3, \theta_4$ and θ_5 were calculated [112] and listed in table 5.6. The strength of A-B and A-A magnetic interaction directly depend on θ_1, θ_2 and θ_5 while B-B interactions vary with θ_3 and θ_4 respectively [110, 112].

Table 5.5. Cation-cation (*b, c, d, e, f*) and cation-anion (*p, q, r, s*) for $Ni_{0.6-x}Zn_{0.4}Co_xFe_2O_4.$

x	b (Å)	c (Å)	d (Å)	e (Å)	f (Å)	p (Å)	q (Å)	r (Å)	s (Å)
0.000	2.9584	3.4689	3.6237	5.4356	5.1050	1.9700	2.0234	3.8740	3.6942
0.033	2.9608	3.4718	3.6267	5.4401	5.1092	1.9720	2.0245	3.8761	3.6971
0.066	2.9591	3.4697	3.6245	5.4368	5.1062	1.9805	2.0065	3.8417	3.6893
0.132	2.9601	3.4709	3.6258	5.4388	5.1080	1.9754	2.0174	3.8624	3.6940
0.264	2.9608	3.4717	3.6267	5.4400	5.1092	1.9751	2.0191	3.8656	3.6953
0.528	2.9696	3.4821	3.6375	5.4563	5.1244	1.9857	2.0170	3.8616	3.7036

It is found that the value of cation-cation interatomic distance *b, c, d, e, f* first increased at x = 0.033, then decreased at x = 0.066 and further increased with Co doping. The increased value of *b, c, d, e* and *f* at x = 0.033 is possibly attributed to distribution of larger size Co^{2+} ions in sites B in place of smaller size Ni^{2+} ions that increase the interatomic distance between cations. At x = 0.066, value of *b, c, d, e* and *f* slightly decrease. This decrement in values is due to distribution of smaller size Fe^{3+} and Co^{2+} ions in sites A. Further increasing value of *b, c, d, e, f* with doping possibly attributed to increasing concentration of Co^{2+} ions in sites B. The cation-anion (*p, q, r, s*) interatomic distance first increase at x = 0.033. This possibly due to the distribution of larger size Co^{2+} ions in sites B in place of smaller size Ni^{2+} ions. At x = 0.066, cation-anion interatomic distance *p* increases while *q, r* and *s* decrease. The increased value of *p* is possibly attributed to the migration of larger size Zn^{2+} ions in sites B. The decreased value of *q, r* and *s* is due to the distribution of smaller size Co^{2+} and Fe^{3+} ions in sites A. With increasing doping concentration,

value of s continuously increased because of distribution of larger size cations in sites B in place of smaller size Ni^{2+} ions. The value of p decreases up to x = 0.264 and then increase at x = 0.528. While the value of q and r increased up to x = 0.264 and then decrease. The decreased value of p up to x = 0.264 is possibly attributed to the decreasing inversion of Co^{2+} ions in sites A. The increased value of p at x = 0528 is due to the large inversion of Co^{2+} in A and high concentration of Co^{2+} ions in sites B. The increased value of q and r up to x = 0.264 also suggest the decreasing inversion of Co^{2+} and Zn^{2+} ions. The decreased value of q and r at x = 0.528 possibly attributes to the distribution of smaller size Co^{2+} ions in sites A in place of larger size Zn^{2+} ions. The calculated values of θ_1, θ_2 and θ_5 *first* increase up to x = 0.066, then decrease up to x = 0.264 and increased at x = 0.528.

Table 5.6. Bond angles (θ_1, θ_2, θ_3, θ_4, θ_5) between ions pairs and theoretically calculated magnetic moment (N_μ) for $Ni_{0.6-x}Zn_{0.4}Co_xFe_2O_4$.

x	θ_1 (Degree)	θ_2 (Degree)	θ_3 (Degree)	θ_4 (Degree)	θ_5 (Degree)	N_μ (μ_B)
0.000	120.595	134.279	97.326	125.887	67.613	5.200
0.033	120.607	134.323	97.304	125.883	67.643	5.233
0.066	120.969	135.632	96.670	125.757	68.511	4.066
0.132	120.751	134.838	97.051	125.833	67.985	4.952
0.264	120.724	134.744	97.097	125.842	67.922	5.344
0.528	120.899	135.377	96.791	125.782	68.343	5.308

The increased value of θ_1, θ_2 and θ_5 indicates the strength of A-B and A-A interaction. The variation in θ_1, θ_2 and θ_5 with Co doping is attributed to distribution of different magnetic moment cations in both sites that increase or decrease the A and B sites magnetic moment. The calculated θ_1, θ_2 and θ_5 value of Co doped Ni-Zn ferrites nanoparticles is higher than un-doped nanoparticles. This is because of high magnetic moment of Co^{2+} ions then the replaced Ni^{2+} ions. The value of θ_3 and θ_4 first decrease up to x = 0.066, then slightly increase up to x = 0.264 and then decrease at high concentration of Co doping. The decreased value of θ_3 and θ_4 up to x = 0.066 indicates the weakening of B-B interactions. This decrease of B-B interaction at x = 0.033 is possibly attributed to the increase in cation-anion distance p. The decreased B-B interaction at x = 0.066 is due to distribution of nonmagnetic Zn^{2+} ions in sites B. The increased value of

θ_3 and θ_4 up to x = 0.264 indicate the strengthening of B-B interaction. This possibly attributed to the distribution of high magnetic moment of Co^{2+} ions in sites B and decreasing interatomic cation-anion distance p. Also at high doping concentration, B-B interaction decreased because of increased interatomic distance p, s, b, f. The theoretically calculated N_μ follow the same trend as experimental M_s and M_μ and have good agreement with each other according to proposed cation distribution. The observed variation in cation-cation, cation-anion and bond angles in ions pairs with Co doping also support the experimental results and proposed cations distribution. The relation between Co doping, D, a, a_{th}, M_s, N_μ and H_c is shown in figure 5.7.
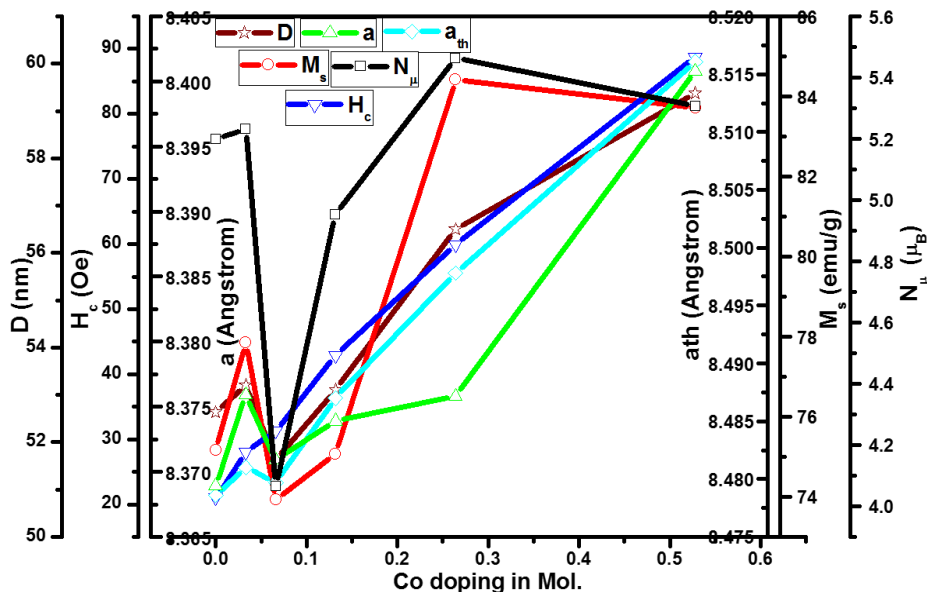
Figure 5.7: The relation between Co doping, crystallite size (D), experimental lattice constant (a) theoretical lattice constant (a_{th}), saturation magnetization (M_s), theoretical magnetic moment (N_μ) and coercivity (H_c) for $Ni_{0.6-x}Zn_{0.4}Co_xFe_2O_4$ nanoparticles.

The comparison between structural and magnetic properties of nanoparticles prepared by *sol-gel* and non-aqueous method annealed at 1100°C are shown in table 5.7. It is found that single phase spinel cubic structure with nanometer size particles have been prepared by non-aqueous method. The nanoparticles prepared by non-aqueous method have high value of M_s and M_μ as compared to *sol-gel* method. Also the values of H_c and M_r of nanoparticles prepared by non-aqueous method are lower and indicate the soft nature of nanoparticles as compared to *sol-gel* method.

Table 5.7: Comparison between structural and magnetic properties of nanoparticles prepared by *sol-gel* and non-aqueous method (***sol-gel***/*non-aqueous*) annealed at 1100ºC

x	D (nm)	Mₛ (emu/g)	M_μ (μ_B)	H_c (Oe)	M_r (emu/g)
0.000	**23**/52	**63.52**/75.17	**2.696**/3.190	**49.94**/21.04	**06.24**/1.23
0.033	**22**/53	**61.97**/77.85	**2.630**/3.304	**35.98**/27.97	**07.65**/2.24
0.264	**23**/56	**51.95**/84.42	**2.205**/3.584	**215.92**/59.90	**13.95**/5.64
0.528	0.528	**27**/59	**45.46**/83.72	**1.930**/3.555	**436.79**/88.78	**18.43**/7.48

Moreover, the particles size of sample (x=0) annealed at 1100ºC are smaller as compared to sample annealed at 700ºC (x=0) when samples prepared by sol-gel method. This decrease in size is due to increase in crystallinity and removal of defects at high annealing temperature (1100ºC) as discused in chapters. As we know that the smaller particle have large surface to volume ratio and hence more atoms on the surface as compared to larger particle that intended to high surface spin canting effect on the surface, which reduce the value of M_s. The annealed particles at 1100ºC (x=0) are smaller in size as compared to sample (x=0) annealed at 700ºC but have larger value of M_s. The larger value of M_s of smaller particles is due to long range ferromagnetic ordering of atoms inside the particle by virtue of high crystalline nature of samples as seen in FESEM images or regular arrangment of atoms inside the particles as compared to samples annealed at 700ºC. The arrangment of atoms inside the particles of samples annealed at 700ºC are much less regular due to amorphous nature as compared to samples annealed at 1100ºC and due to this, long range ferromagnetic ordering of atoms inside the particles has lost and smaller value of M_s has been observed. The surface to volume ratio of nanoparticles prepared by non-aqueous method are smaller due to larger size and have much less surface spin canting effect as compared to samples prepared by sol-gel method. Also the samples prepared by non-aqueous method are high crystalline in nature as seen in FESEM images that causes atoms are regularly arranged in perfect manner and have long range ferromagnetic ordering inside the particles as compared to sol-gel method. Therefore, dominent long range ferromagnetic ordering due to high crystallanity and high value of M_s; on the other hand low surface spin canting effect as well as absence of secondary phase has been obtained in ferrite nanopartilces prepared by non-aqueous as compared to nanoparticles prepared by sol gel method.

5.5 Conclusion

Single phase spinel cubic structure $Ni_{0.6-x}Zn_{0.4}Co_xFe_2O_4$ nanoparticles have been successfully synthesized by non-aqueous method. Phase identification has been done by XRD. Crystallite size (D) is found in nm range also calculated from prominent XRD peak (113). The found variation in crystallite size (D) and other structural parameters have been explained in terms of distribution of cations in tetrahedral (A) and octahedral (B) sites having different size. Crystallite size (D) of samples prepared by non-aqueous method is larger than samples prepared by *sol-gel* method (chapter-4). Homogeneous distribution of particles and high crystalline nature of prepared samples have been seen from FESEM images as compared to previously synthesized samples by *sol-gel* method. The samples prepared by non-aqueous method have good stoichiometry found from EDX. High saturation magnetization (M_s), low retentivity (M_r) and low coercivity (H_c) have been found in samples prepared by non-aqueous method as compared to *sol-gel* method. High saturation magnetization (M_s) of samples prepared by non-aqueous method is due to larger particle size, high crystalline nature and due to minimum surface spin distortion. The variation in saturation magnetization (M_s) with doping is attributed to distribution of cations in different sub lattices having different magnetic moment. The increase in coercivity (H_c) with doping is due to positive magneto crystalline anisotropy energy (K) of Co^{2+} ions that increased with increasing concentration of Co^{2+} ions in octahedral (B) sites. The very low value of coercivity (H_c) indicates that prepared samples by non-aqueous methods are magnetically soft in nature than samples prepared by *sol-gel* method. Theoretically calculated lattice constant (a_{th}), Neel magnetic moment (N_μ) and other parameters calculated from proposed cations distribution have good agreement with results that obtained from experimental data. Lastly it is concluded that, the structural and magnetic properties of $Ni_{0.6-x}Zn_{0.4}Co_xFe_2O_4$ nanoparticles strongly depend upon methods of preparation, annealing temperature, distribution of types of cations in sites A and B and dopant concentration. Single phase spinel cubic structure, nanometer range crystallite size, high crystallinity, high saturation magnetization and low coercivity $Ni_{0.6-x}Zn_{0.4}Co_xFe_2O_4$ nanoparticles are successfully prepared by non-aqueous method and indicate the usefulness of these materials in targeted drug delivery, hyperthermia, MRI, EMI shielding and magnetic recording device applications.

CHAPTER 6
SUMMARY

6.1 Summary

Ni-Zn ferrites are soft magnetic material and very important from technological point of view. The unique properties of Ni-Zn ferrite nanoparticles such as low coercivity, low magnetic losses, high Curie temperature, high resistivity, moderate saturation magnetization, good mechanical hardness, chemical stability, high magnetic permeability and resistance to corrosion make it promising candidates for electrical, electronics and bio-medical applications. In this work we have enhanced the magnetic properties of Ni-Zn ferrite system in terms of doping, synthesis methods and annealing temperature. Co^{2+} ions have been used as dopant because of its high magnetic moment, positive magneto crystalline anisotropy energy and high curie temperature. In order to synthesize the undoped and Co doped Ni-Zn ferrite nanoparticles first of all *sol-gel* method has been used. Further, we have developed a new method that is non-aqueous method in order to prepare the nanoparticles in short duration, without complexing agent and at low temperature. The structural, morphological, stoichiometric and magnetic properties of all prepared samples have been analyzed using XRD, FESEM, EDX and VSM respectively. The variation in structural and magnetic properties have been explained in terms of doping, distribution of cations in different sub-lattices, synthesis methods and annealing temperatures.

In first objective, all samples have been processed by *sol-gel* method and annealed at 700°C temperature. The variation in structural and magnetic properties has been explained in terms of Co^{2+} ions distribution in octahedral (B) sites. From XRD analysis it has been found that the prepared samples at x = 0.264, 0.27 and 0.528 of Co doping have single phase spinel cubic structure. The crystallite size (*D*) of all prepared samples has been calculated using Scherer formula and found to increase with Co doping because of Co^{2+} ions distribution in octahedral sites having larger size as compared to replaced Ni^{2+} ions. The decrease in *D* value possibly attributes to prominent hematite phase effect. The strain present in the crystal structure also found in proportion with the secondary phase. The confirmation of crystallite size and type of strain present in prepared nanoparticles has been done from Williamson-Hall (W-H) method using XRD data. The calculated crystallite size (*W-H D*) from W-H method is equivalent to that calculated from Scherer formula in nm range and a positive slop of linear fitted W-H plots shows tensile strain present in all prepared nanoparticles. The morphology of prepared samples gets changed with Co doping with agglomeration of particles as investigated by FESEM. FESEM

micrographs also shows the porous nature of samples. EDX study revealed that in prepared samples, all elements are present in stoichiometric ratio. The magnetic properties measurement from VSM shows that the saturation magnetization (M_s) initially decreased with Co doping up to x = 0.033 and then increased with doping and reached maximum at x = 0.528. The reduced value of M_s is due to dominant spin canting effect caused by prominent secondary phase. The increased value of M_s is credited to increasing concentration of Co^{2+} ions in octahedral sites having high magnetic moment then replaced Ni^{2+} ions and decreasing effect of secondary phase. The obtained values of retentivity (M_r) as well as coercivity (H_c) continuously increased with Co doping because of its positive magneto-crystalline anisotropy energy. The theoretical and experimental results have good agreement with each other according to proposed cations distribution. The single phase spinel cubic structure and higher value of M_s at x = 0.528 indicates the usefulness of these material in EMI shielding.

In second objective, undoped and Co doped Ni-Zn ferrite nanoparticles were also synthesized by sol gel method and annealed at high temperature 1100°C. XRD study revealed that when samples annealed at high temperature, most of the hematite phase diminished and single phase spinel cubic structure nanoparticles has formed other than at x = 0.0165. Also the **D** value of prepared samples slightly decreased when samples annealed at 1100°C. This decrease in **D** value is due to removal of secondary phase, increasing crystallinity, increasing density or decreasing porosity of samples and changing distribution of cations at high annealing temperature. Estimated crystallite size (**W-H D**) from W-H method is also equivalent to that calculated from Scherer formula. The negative slope of linear fitted W-H plots shows the compressive strain present in the particles which is due to the effect of high annealing temperature. The morphology of prepared samples also gets changed when samples annealed at high temperature. FESEM micrograph shows that the prepared samples annealed at 1100°C are highly crystalline in nature then samples annealed at 700°C. The magnetic behavior of nanoparticles has also been found to change at high annealing temperature 1100°C. The undoped Ni-Zn ferrite nanoparticles annealed at 1100°C have high value of saturation magnetization (M_s) than sample annealed at 700°C perhaps due to removal of secondary phase and increasing crystallinity at high annealing temperature. Further saturation magnetization (M_s) decreased with Co doping is due to distribution of Co^{2+} ions in tetrahedral (A) sites at high annealing temperature. Also retentivity (M_r) and coercivity (H_c) of undoped Ni-Zn ferrite nanoparticles is

smaller compared to the samples annealed at low temperature. This is because of inverse relation of coercivity (H_c) with magnetization (M_s) and crystallinity. Further with doping, the value of retentivity (M_r) and coercivity (H_c) first decrease up to x = 0.033 and then increases. The decreased value is attributed to the Co^{2+} ions distribution in tetrahedral (A) sites. The increased value after x = 0.033 is due to Co^{2+} ions distribution in octahedral (B) sites. The theoretical lattice constant (a_{th}), Neel magnetic moment (N_μ) and other parameters calculated from proposed cations distribution also have good agreement with results obtained from experimental data.

In third objective, undoped and Co doped Ni-Zn ferrite nanoparticles have been synthesized by new developed method that is non-aqueous in nature. Single phase spinel cubic structure nanoparticles have been successfully synthesized by non-aqueous method and confirmed by XRD. The samples prepared by non-aqueous method have larger crystallite size (**D**) than samples prepared by *sol-gel* method. The variation in **D** value and other structural parameters with doping are due to distribution of cations in tetrahedral (A) and octahedral (B) sites having different size. Also estimated crystallite (**W-H D**) sizes from W-H method are equivalent to that calculated from Scherrer's formula in nm range. The negative slope of linear fitted W-H plots shows that the prepared samples by non-aqueous method have compressive strain. The samples prepared by non-aqueous method have homogeneous grain distribution and high crystalline nature as compared to previous synthesized samples by *sol-gel* method seen from FESEM images. The samples prepared by non-aqueous method are stoichiometric in ratio as observed from EDX spectra. High saturation magnetization (M_s), low retentivity (M_r) and low coercivity (H_c) has been found in samples prepared by non-aqueous method as compared to *sol-gel* method. High saturation magnetization (M_s) of samples prepared by non-aqueous method is due to larger crystallite size (**D**), high crystalline in nature or long ferromagnetic ordering and due to minimum surface spin distortion. The variation in saturation magnetization (M_s), retentivity (M_r) and coercivity (H_c) with doping are due to cations distribution effect. Low value of coercivity (H_c) indicates that prepared samples by non-aqueous methods are magnetically soft in nature than samples prepared by *sol-gel* method. Single phase spinel cubic structure, nanometer crystallite size (**D**), high crystallinity, high saturation magnetization (M_s) and low coercivity (H_c) $Ni_{0.6-x}Zn_{0.4}Co_xFe_2O_4$ nanoparticles are successfully prepared by non-aqueous method and indicate

the usefulness of these materials in target drug delivery, hyperthermia, MRI, EMI shielding and magnetic recording device applications.

The developed non-aqueous method is very simple, cost effective, low temperature synthesis, multi component spinel system nanoparticle can be prepared in short duration and nanoparticles can be prepared without complexing agent as compared to *sol-gel* method. On the basis of above findings, it is concluded that, the structural and magnetic properties of spinel ferrites nanoparticles strongly depend upon methods of preparation, annealing temperature, distribution of types of cations in sites A and B and dopant concentration.

REFERENCES

1. G. A. Mansoori, "Principles of nanotechnology: molecular-based study of condensed matter in small systems," *World Sci.*, 2005.

2. M. Roukes, "Plenty of room,plenty of history," *Nat. Nanotechnol.*, vol. 4, pp. 783–784, 2009.

3. A. Navrotsky, "Materials and nanotechnology," *J. Franklin Inst.*, vol. 340, pp. 263–268, 2003.

4. R. Waser, "Nanotechnology: Volume 4: Information Technology II," *John Wiley & Sons*, vol. 4, 2008.

5. K. Bogunia-kubik and M. Sugisaka, "From molecular biology to nanotechnology and nanomedicine," *Biosyst. 65*, vol. 65, pp. 123–138, 2002.

6. L. Mazzola, "Commercializing nanotechnology," *Nat. Biotechnol.*, vol. 21, pp. 1137–1143, 2003.

7. M. Henini, "Nanotechnology–growing in a shrinking world," *III-Vs Rev.*, vol. 11, pp. 30–34, 1998.

8. M. Geller, F. Hopfer, and D. Bimberg, "Nanostructures for nanoelectronics: No potential for room temperature applications," *Microelectro. J.*, vol. 39, pp. 302–306, 2008.

9. D. Minoli, "Nanotechnology applications to telecommunications and networking," *John Wiley & Sons,* 2005.

10. L. M. Smith, "Molecular robots on the move," *Nat.*, vol. 465, pp. 167–168, 2010.

11. C. C. Jordan, I. Kaiser, and V. C. Moore, "2013 Nanotechnology patent literature review: graphitic carbon-based nanotechnology and energy applications are on the rise." *Nanotech. L. & Bus,* vol. 11, pp. 111, 2014.

12. P. Afanasiev, "Elemental sulfur and sulfur-rich compounds II. topics in current chemistry, 231," *J. Am. Chem. Soc.*, vol. 126, pp. 14678–14680, 2004.

13. G. Binning, H. Rohrer, C. Gerber, and E. Weibel, "Surface studies by scanning tunneling microscopy," *Phys. Rev. Lett.*, vol. 49, pp. 57–61, 1982.

14. H. Lilholt, "Deformation of polycrystals: Mechanisms and microstructures," 1981.

15. B. Rogers, J. Adams, and S. Pennathur, "Nanotechnology: Understanding small systems," *Crc Pres.*, 2014.

16. M. Faraday, "The Bakerian lecture: experimental relations of gold (and other metals) to light," … *Trans. R. Soc. …*, vol. 147, pp. 145–181, 1857.

17. M. Pavlovic, J. Mayfield, and B. Balint, "Nanotechnology and its application in medicine." *In Handb. of Medical and Healthcare Tech. Springer New York*, pp. 181-205, 2013.

18. D. C. Mattis, "History of magnetism," *Theory Magn. I Statics Dyn.*, pp. 1–38, 1981.

19. J. Smit, and H. P. J. Wijn, "Ferrites," *Philips Tech. Lib. Eindhoven*, 1959.

20. R. Valenzuela, "Magnetic ceramics: Chemistry of solid state materials," *Cambridge Uni. New York,* 1994.

21. D. W. McRobbie, A. M. Elizabeth, J. G. Martin, and R. P. Martin, "MRI from picture to proton," *Cambridge university press*, 2007.

22. B. Bederson, "Essay: Samuel abraham goudsmit (1902-1978)," *Phys. Rev. Lett.*, vol. 101, pp. 2–6, 2008.

23. J. L. Snoek, " New developments in ferromagnetic materials," *Elsevier Pub. Comp.,* vol. 19, 1949.

24. J. L. Neel, "Anti-ferromagnetism and ferromagnetism proceeding soft he," *Physical Soci. London,* vol. 65, pp 869–885, 1951.

25. P. W. Anderson, "Antiferromagnetism. theory of suyerexchange," *Phys. Rev.*, vol. 79, pp. 350–352, 1950.

26. J. H. Van-Vleck, "On the theory of ferromagnetic resonance," *Phys. Rev.,* vol. 78, pp 266, 1950.

27. Y. Yafet, and C. Kittle, "X-ray diffraction and magnetic measurements of the Fe-Cr spinels," *Phy. Rev,* vol. 87, pp. 290, 1952.

28. B. D. Cullity, and C. D. Graham, "Introduction to magnetic materials," *John Wiley & Sons*, 2011.

29. E. V. Gopalan, and M. R. Anantharaman, "On the synthesis and multifunctional properties of some nanocrystalline spinel ferrites and magnetic nanocomposites." *PhD diss., Cochin University of Sci. Tech.,* 2009.

30. B. Issa, I. M. Obaidat, B. A. Albiss, and Y. Haik, "Magnetic nanoparticles: Surface effects and properties related to biomedicine applications," *Int. J. Mol. Sci.*, vol. 14, pp. 21266–21305, 2013.

31. M. Sugimoto, "The Past, present and future of ferrites," *J. Am. Ceram. Soc.*, vol. 82, pp. 269–280, 1999.

32. E. K. Sickafus, and R. Hughes, "Spinel compounds: structure and property relations," pp. 3277-3278, 1999.

33. V. G. Harris, N. C. Koon, C. M. Williams, Q. Zhang, M. Abe, and J. P. Kirkland, "Cation distribution in NiZn-ferrite films via extended X-ray absorption fine structure," *Appl. Phys. Lett.*, vol. 68, pp. 2082–2084, 1996.

34. L. Néel, "Sur Linterpretation des proprietes magnetiques des ferrites de terres rares," *Comptes Rendus Hebdomadaires des Seances De L Academie des Sci.,* vol. 239, pp. 8-11, 1954.

35. S. Geller, and M. A. Gilleo, "The crystal structure and ferrimagnetism of yttrium-iron garnet, Y 3 Fe 2 (FeO4) 3." *J. Phys. Chem. solids*, vol. 3, pp. 30-36, 1957.

36. H. Zijlstra, "Permanent magnets; theory," *Handb. Ferromagn. Mater.*, vol. 3, pp. 37–105, 1982.

37. K. J. Standley, "Oxide magnetic materials," *Oxford University Press*, 1972.

38. A. L. Stuijts, G. W. Rathenau, and G. H. Weber. "Ferroxdure ii and iii, anisotropic permanent magnet materials," *Philips Tech. Rev,* vol. 16, pp. 7, 1954,

39. G.I. Likhtenshtein, J. Yamauchi, S. Nakatsuji, A.I. Smirnov, and R. Tamura, "Fundamentals of magnetism", *Nitroxides: Applicat. Chem., Biomedi., Mater. Sci.*, pp. 1-45, 2008.

40. T. Thomson, L. Abelmann, and H. Groenland, "Magnetic data storage: past present and future," *Magn. nanostructures Mod. Technol.*, pp. 237–306, 2008.

41. R. R. Muslim, "Magnetic properties of manganese ferrite nanoparticles." *PhD diss., Thapar University Patiala*, 2012.

42. C. B. Carter, and M. G. Norton, "Ceramic materials: science and engineering," *Springer Sci. Bus. Media*, 2007.

43. O. Kahn, "Molecular magnetism," *VCH Publishers Inc.(USA),* pp. 393, 1993.

44. B. Viswanathan, and V. R. K. Murthy, "Ferrite materials: science and technology," *Springer Verlag*, 1990.

45. S. P. Gubin, Y. A. Koksharov, G. B. Khomutov, and G. Y. Yurkov, "Magnetic nanoparticles: preparation, structure and properties," *Russ. Chem. Rev.*, vol. 74, pp. 489–520, 2005.

46. D.C. William and D.G. Rethwisch, "Fundamentals of materials science and engineering: an integrated approach," *John Wiley & Sons*, 2012.

47. D. S. Mathew and R. S. Juang, "An overview of the structure and magnetism of spinel ferrite nanoparticles and their synthesis in micro emulsions," *Chem. Eng. J.*, vol. 129, pp. 51–65, 2007.

48. E. C. Stoner and E. P. Wohlfarth, "A mechanism of magnetic hysteresis in heterogeneous alloys," *Philos. Trans. R. Soc. London. Ser. A, Math. Phys. Sci.*, vol. 240, pp. 599–642, 1948.

49. P. J. Thomas and G. U. Kulkarni, "*Nanocry.: Synthes., Proper. Applicat,*" *Springer*, 2007.

50. Q. A. Pankhurst, and R. J. Pollard, "Fine-particle magnetic oxides," *J. Phys: Condens. Matter*, vol. 5, pp. 8487, 1993

51. A. H. Lu, E. L. Salabas, and F. Schüth, "Magnetic nanoparticles: Synthesis, protection, functionalization, and application," *Angew. Chemie - Int. Ed.*, vol. 46, pp. 1222–1244, 2007.

52. M. Arruebo, R. Fernández-pacheco, M. R. Ibarra, and J. Santamaría, "Magnetic nanoparticles for drug delivery," *Nano Tod.*, vol. 2, pp. 22–32, 2007.

53. T. Suzuki, T. Tanaka, and K. Ikemizu, "High density recording capability for advanced particulate media," *J. Magn. Magn. Mater.*, vol. 235, pp. 159–164, 2001.

54. E. Olsen and J. Thonstad, "Nickel ferrite as inert anodes in aluminium electrolysis: Part I. Material fabrication and preliminary testing," *J. Appl. Electrochem.*, vol. 29, pp. 293–299, 1999.

55. S. Gubbala, H. Nathani, K. Koizol, and R. D. K. Misra, "Magnetic properties of nanocrystalline Ni-Zn, Zn-Mn, and Ni-Mn ferrites synthesized by reverse micelle technique," *Phys. B Condens. Matter,* vol. 348, pp. 317–328, 2004.

56. P. Rao, "Initial Permeability Dependence on the microstructural and compositional changes in Ni-Zn-Sc ferrites," *J. Phys. IV*, vol. 7, pp. C1-239, 1997.

57. D. De Materiales and A. Postal, "Synthesis, microstructure and magnetic properties of Ni–Zn ferrites," *J. Magn. Magn. Mater.*, vol. 256, pp. 174–182, 2003.

58. J. da Silva and N. D. Mohallem, "Preparation of composites of nickel ferrites dispersed in silica matrix," *J. Magn. Magn. Mater.*, vol. 226–230, pp. 1393–1396, 2001.

59. M. Jalaly, M. H. Enayati, and F. Karimzadeh, "Investigation of structural and magnetic properties of nanocrystalline Ni0.3Zn0.7Fe2O4 prepared by high energy ball milling," *J. Alloys Compd.*, vol. 480, pp. 737–740, 2009.

60. M. Sertkol, Y. Köseoğlu, A. Baykal, H. Kavas, and M. S. Toprak, "Synthesis and magnetic characterization of Zn0.7Ni0.3Fe2O4 nanoparticles via microwave-assisted combustion route," *J. Magn. Magn. Mater.*, vol. 321, pp. 157–162, 2009.

61. B. P. Rao and O. F. Caltun, "Microstructure and magnetic behaviour of Ni-Zn-Co ferrites," *J. Optoelectron. Adv. Mater.*, vol. 8, pp. 995–997, 2006.

62. P. G. Bercoff and H. R. Bertorello, "Localized canting effect in Zn-substituted Ni ferrites," *J. Magn. Magn. Mater.,* vol. 213, pp. 56–62, 2000.

63. H. Su, H. Zhang, X. Tang, Y. Jing, and Y. Liu, "Effects of composition and sintering temperature on properties of NiZn and NiCuZn ferrites," *J. Magn. Magn. Mater.,* vol. 310, pp. 17–21, 2007.

64. R. Kumar, H. Kumar, R. R. Singh, and P. B. Barman, "Variation in magnetic and structural properties of Co-doped Ni-Zn ferrite nanoparticles: a different aspect," *J. Sol-gel Sci. Technol.*, vol. 78, pp. 566–575, 2016.

65. B. I. Kharisov, H. V. R. Dias, O. V. Kharissova, A. Vázquez, Y. Peña, and I. Gómez, "Solubilization, dispersion and stabilization of magnetic nanoparticles in water and non-aqueous solvents: recent trends," *RSC Adv.*, vol. 4, pp. 45354–45381, 2014.

66. Q. Chen, P. Du, W. Huang, L. Jin, W. Weng, and G. Han, "Ferrite with extraordinary electric and dielectric properties prepared from self-combustion technique," *Appl. Phys. Lett*., vol. 90, pp. 132907, 2007.

67. P. L. Leng, M. G. Naseri, E. Saion, A. H. Shaari, and M. A. Kamaruddin, "Synthesis and characterization of Ni-Zn ferrite nanoparticles (Ni0.25Zn0.75Fe2O4) by thermal treatment method," *Adv. Nanoparticles*, vol. 2, pp. 378–383, 2013.

68. S. R. Shannigrahi, K. P. Pramoda, and F. A. A. Nugroho, "Synthesis and characterizations of microwave sintered ferrite powders and their composite films for practical applications," *J. Magn. Magn. Mater*., vol. 324, pp. 140–145, 2012.

69. E. Rezlescu, L. Sachelarie, P. D. Popa, and N. Rezlescu, "Effect of Substitution of divalent ions on the electrical and magnetic properties of NiZnMe ferrite," *IEEE Trans. Magn.*, vol. 36, pp. 3962–3967, 2000.

70. C. M. Srivastava, and M. J. Patni, "*Advances in Ferrites*," vol. 1, pp. 226, 1989.

71. M. S. R. Prasad, B. R. Babu, K. V. Ramesh, and K. Trinath, "Structural and magnetic studies on chromium substituted ni-zn nano ferrite synthesized by citrate gel auto combustion method," *J. Supercond. Nov. Magn*., vol. 27, pp. 2735–2745, 2014.

72. H. Huili, B. Grindi, G. Viau, and L. Ben Tahar, "Effect of cobalt substitution on the structure, electrical, and magnetic properties of nanorcrystalline Ni0.5Zn0.5Fe2O4 prepared by the polyol process," *Ceram. Int.*, vol. 40, pp. 16235–16244, 2014.

73. K. Bhattacharjee, S. P. Pati, G. C. Das, D. Das, and K. K. Chattopadhyay, "Effect of particle size distribution on the structure, hyperfine, and magnetic properties of Ni0.5Zn0.5Fe2O4 nanopowders," *J. Appl. Phys*., vol. 116, pp. 0–10, 2014.

74. K. Velmurugan, V. Sangli, K. Venkatachalapathy, and S. Sendhilnathan, "Synthesis of nickel zinc iron nanoparticles by coprecipitation technique," *Mater. Res.*, vol. 13, pp. 299–303, 2010.

75. Z. Beji, L. S. Smiri, N. Yaacoub, J.-M. Grenèche, N. Menguy, S. Ammar, and F. Fiévet, "Annealing effect on the magnetic properties of polyol-made Ni−Zn ferrite nanoparticles," *Chem. Mater.*, vol. 22, pp. 1350–1366, 2010.

76. N. Chen and M. Gu, "Microstructure and microwave absorption properties of Y-substituted Ni-Zn ferrites," *Open J. Met.*, vol. 2, pp. 37–41, 2012.

77. X. Shen, Y. Wang, X. Yang, L. Lu, and L. Huang, "0.3-3 GHz magneto-dielectric properties of nanostructured NiZnCo ferrite from hydrothermal process," *J. Mater. Sci. Mater. Electron.*, vol. 21, pp. 630–634, 2010.

78. G. S. V. R. K. Choudary, M. C. Varma, A. M. Kumar, K. H. Rao, and B. R. Kumar, "Enhancement of magnetic properties in cobalt substituted Ni-Zn nanoferrite system," *AIP Conf. Proc.*, vol. 1347, pp. 31–34, 2011.

79. S. Thakur, S. C. Katyal, A. Gupta, V. R. Reddy, and M. Singh, "Room temperature ferromagnetic ordering in indium substituted nano-nickel-zinc ferrite," *J. Appl. Phys.*, vol. 105, pp. 10–13, 2009.

80. S. B. Waje, M. Hashim, Z. Abbas, D. Ehsan, and D. Ehsan, "Room temperature measurements of physical and magnetic characteristics of," *Aust. J. Basic Appl. Sci.*, vol. 3, pp. 2716–2723, 2009.

81. S. Komarneni, E. Fregeau, E. Breval, and R. Roy, "Hydrothermal preparation of ultrafine ferrites and their sintering," *J. Am. Ceram. Soc.*, vol. 71, pp. C-26-C-28, 1988.

82. A. Ataie, M. R. Piramoon, I. R. Harris, and C. B. Ponton, "Effect of hydrothermal synthesis environment on the particle morphology, chemistry and magnetic properties of barium hexaferrite," *J. Mater. Sci.*, vol. 30, pp. 5600–5606, 1995.

83. M. Seki, "Observations of uftrafine ZnFe204 particles with transmission electron microscopy," *J. Appl. Phys.*, vol. 63, pp. 1424–1427, 1988.

84. A. R. West, "Solid state chemistry and its applications," *John Wiley & Sons*, 2007.

85. J. Gangwar, B. K. Gupta, S. K. Tripathib, and A. K. Srivastava, "Phase dependent thermal and spectroscopic responses of different morphogenesis of Al2O3 nanostructures," *Nanoscal.*, vol. 7, pp. 13313–13344, 2015.

86. B. E. Warren, "X-ray Diffraction," *Courier Corp.*, 1969.

87. X. Shen, Y. Wang, X. Yang, Y. Xia, J. F. ZHUANG, and P. Tang, "Megahertz magneto-dielectric properties of nanosized NiZnCo ferrite from CTAB-assisted hydrothermal process," *Trans. Nonferrous Met. Soc. China*, vol. 19, pp. 1588–1592, 2009.

88. J. S. Ghodake, R. C. Kambale, S. D. Kulkarni, S. R. Sawant, and S. S. Suryavanshi, "Complex permeability studies of Ni–Co–Zn ferrites synthesized by an oxalate precursor method," *Smart Mater. Struct.*, vol. 18, pp. 125009, 2009.

89. S. L. Pereiraa, H.-D. Pfannesa, A. A. M. Filhob, L. C. B. de M. Pintob, and M. A. Chíncaro, "A comparative study of NiZn ferrites modified by the addition of cobalt," *Mater. Res.*, vol. 2, pp. 231–234, 1999.

90. L. Z. Li, L. Peng, X. H. Zhu, and D. Y. Yang, "Effects of Cu and Co substitution on the properties of Ni-Zn ferrite thin films," *J. Electro. Sci. Tech.,* vol. 10, pp. 88, 2012.

91. B. S. Yoo, Y. G. Chae, Y. M. Kwon, B. W. L. D. H. Kim, and C. Liu, "Effects of solution concentration on the structural and magnetic properties of Ni0.5Zn0.5Fe2O4 ferrite nanoparticles prepared by sol-gel," *J. Magn.*, vol. 18, pp. 230–234, 2013.

92. Y. M. Kwon, M.-Y. Lee, M. Mustaqima, C. Liu, and B. W. Lee, "Structural and magnetic properties of Ni0.6Zn0.4Fe2O4 ferrite prepared by solid state reaction and sol-gel," *J. Magn.* vol. 19, pp. 64–67, 2014.

93. P. Laokul, V. Amornkitbamrung, S. Seraphin, and S. Maensiri, "Characterization and magnetic properties of nanocrystalline CuFe2O4, NiFe2O4, ZnFe2O4 powders prepared by the Aloe vera extract solution," *Curr. Appl. Phys.*, vol. 11, pp. 101–108, 2011.

94. M. George, S. S. Nair, A. M. John, P. A. Joy, and M. R. Anantharaman, "Structural, magnetic and electrical properties of the sol-gel prepared Li 0.5 Fe 2.5 O 4 fine particles," *J. Phys. D. Appl. Phys.*, vol. 39, pp. 900–910, 2006.

95. S. Prabahar and M. Dhanam, "CdS thin films from two different chemical baths - Structural and optical analysis," *J. Cryst. Growth*, vol. 285, pp. 41–48, 2005.

96. M. Javed Iqbal and M. Rukh Siddiquah, "Structural, electrical and magnetic properties of Zr-Mg cobalt ferrite," *J. Magn. Magn. Mater.*, vol. 320, pp. 845–850, 2008.

97. H. Kumar, M. Kumar, P. B. Barman, and Ragini Raj Singh, "Stable and luminescent wurtzite CdS, ZnS and CdS/ZnS core/shell quantum dots," *Appl. Phys. A*, vol. 117, pp. 1249-1258, 2014.

98. A. Ahlawat, V. G. Sathe, V. R. Reddy, and A. Gupta, "Mossbauer, Raman and X-ray diffraction studies of superparamagnetic NiFe2O4 nanoparticles prepared by *sol-gel* auto-combustion method," *J. Magn. Magn. Mater.*, vol. 323, pp. 2049–2054, 2011.

99. L Neel, "Théorie du traînage magnétique de diffusion," *J. de Physique et le Radium*, vol. 13, pp. 249-264, 1952.

100. M. Y. Lodhi, K. Mahmooda, A. Mahmoodb, H. Malik, M. F. Warsib, I. Shakir, M. Asghar, and M. A. Khan, "New Mg0.5CoxZn0.5Fe2O4 nano-ferrites: Structural elucidation and electromagnetic behavior evaluation," *Curr. Appl. Phys.*, vol. 14, pp. 716–720, 2014.

101. S. Thakur, S. C. Katyal, and M. Singh, "Structural and magnetic properties of nano nickel-zinc ferrite synthesized by reverse micelle technique," *J. Magn. Magn. Mater.*, vol. 321, pp. 1–7, 2009.

102. S. S. Nair, M. Mathews, P. A. Joy, S. D. Kulkarni, and M. R. Anantharaman, "Effect of cobalt doping on the magnetic properties of superparamagnetic γ-Fe2O3-polystyrene nanocomposites," *J. Magn. Magn. Mater.*, vol. 283, pp. 344–352, 2004.

103. H. M. Zaki, S. H. Al-Heniti, and T. A. Elmosalami, "Structural, magnetic and dielectric studies of copper substituted nano-crystalline spinel magnesium zinc ferrite," *J. Alloys Compd.*, vol. 633, pp. 104–114, 2015.

104. M. A. Hakim, S. Kumar, S. S. Sikder, and K. Hanium, "Cation distribution and electromagnetic properties of spinel type Ni–Cd ferrites," *J. Phys. Chem. Solids*, vol. 74, pp. 1316–1321, 2013.

105. K. A. Mohammed, A. D. Al-Rawas, A. M. Gismelseed, A. Sellai, H. M. Widatallah, A. Yousif, M. E. Elzain, and M. Shongwe, "Infrared and structural studies of Mg 1-xZn xFe 2O 4 ferrites," *Phys. B Condens*. Matter, vol. 407, pp. 795–804, 2012.

106. R. Sharma, P. Thakur, M. Kumar, N. Thakur, N. S. Negi, P. Sharma, and V. Sharma, "Improvement in magnetic behaviour of cobalt doped magnesium zinc nano- ferrites via co-precipitation route," *J. Alloys Compd.*, 2016.

107. M. Houshiar, F. Zebhi, Z. Jafari, A. Alidoust, and Z. Askari, "Synthesis of cobalt ferrite (CoFe2O4) nanoparticles using combustion, coprecipitation, and precipitation methods: A comparison study of size, structural, and magnetic properties," *J. Magn. Magn. Mater.*, vol. 371, pp. 43–48, 2014.

108. C. A. Goldman, "Modern ferrite technology," *Springer Sci. Bus. Media*, 2006.

109. M. Arana, V. Galván, S. E. Jacobo, and P. G. Bercoff, "Cation distribution and magnetic properties of LiMnZn ferrites," *J. Alloys Compd.*, vol. 568, pp. 5–10, 2013.

110. G. Kumar, J. Shah, R. K. Kotnala, V. P. Singh, Sarveena, G. Garg, S. E. Shirsath, K. M. Batoo, and M. Singh, "Superparamagnetic behaviour and evidence of weakening in super-exchange interactions with the substitution of Gd3+ ions in the Mg-Mn nanoferrite matrix," *Mater. Res. Bull.*, vol. 63, pp. 216–225, 2015.

111. N. H. Vasoya, V. K. Lakhani, P. U. Sharma, K. B. Modi, R. Kumar, and H. H. Joshi, "Study on the electrical and dielectric behaviour of Zn-substituted cobalt ferrialuminates," *J. Phys. Condens. Matter*, vol. 18, pp. 8063–8092, 2006.

112. V. K. Lakhani, T. K. Pathak, N. H. Vasoya, and K. B. Modi, "Structural parameters and X-ray Debye temperature determination study on copper-ferrite-aluminates," *Solid State Sci.*, vol. 13, pp. 539–547, 2011.

113. H. Fujimori, H. Yoshimoto, T. Masumoto, and T. Mitera, "Anomalous eddy current loss and amorphous magnetic materials with low core loss (invited)," *J. Appl. Phys.*, vol. 52, pp. 1893–1898, 1981.

114. T. Tsutaoka, "Frequency dispersion of complex permeability in Mn-Zn and Ni-Zn spinel ferrites and their composite materials," *J. Appl. Phys.*, vol. 93, pp. 2789–2796, 2003.

115. A. M. Abdeen, "Electric conduction in Ni–Zn ferrites," *J. Magn. Magn. Mater.*, vol. 185, pp. 199–206, 1998.

116. M. A. El Hiti, "Dielectric behaviour in Ni–Zn ferrites," *J. Magn. Magn. Mater.*, vol. 192, pp. 305–313, 1999.

117. S. A. Saafan, T. M. Meaz, E. H. El-Ghazzawy, M. K. El Nimr, M. M. Ayad, and M. Bakr, "A.C. and D.C. conductivity of NiZn ferrite nanoparticles in wet and dry conditions," *J. Magn. Magn. Mater.*, vol. 322, pp. 2369–2374, 2010.

118. S. Singhal and K. Chandra, "Cation distribution and magnetic properties in chromium-substituted nickel ferrites prepared using aerosol route," *J. Solid State Chem.*, vol. 180, pp. 296–300, 2007.

119. P. S. A. Kumar, J. J. Shrotri, S. D. Kulkami, C. E. Deshpande, and S. K. Date, "Low temperature synthesis of Ni0.8 Zn0.2 Fe2O 4 powder and its characterization," *Mater. Lett.*, vol. 27, pp. 293–296, 1996.

120. M. Veverka, Z. Jirák, O. Kaman, K. Knížek, M. Maryško, E. Pollert, K. Závěta, a Lančok, M. Dlouhá, and S. Vratislav, "Distribution of cations in nanosize and bulk Co-Zn ferrites.," *Nanotech.,* vol. 22, pp. 345701, 2011.

121. M. Niyaifar, "Effect of preparation on structure and magnetic properties of ZnFe2O4," *J. Magn.*, vol. 19, pp. 101–105, 2014.

122. S. A. Oliver, V. G. Harris, H. H. Hamdeh, and J. C. Ho, "Large zinc cation occupancy of octahedral sites in mechanically activated zinc ferrite powders," *Appl. Phys. Lett*., vol. 76, pp. 2761, 2000.

123. G. A. Sawatzky, F. Van Der Woude, and A. H. Morrisii, "Mossbauer study of several ferrimagnetic spinels," *Phys. Rev.*, vol. 187, pp. 747–757, 1969.

124. V. Sreeja, S. Vijayanand, S. Deka, and P. A. Joy, "Magnetic and mössbauer spectroscopic studies of NiZn ferrite nanoparticles synthesized by a combustion method," *Hyperfine Interact.*, vol. 183, pp. 99–107, 2008.

125. J. Xiang, X. Shen, and X. Meng, "Preparation of Co-substituted MnZn ferrite fibers and their magnetic properties," *Mater. Chem. Phys*., vol. 114, pp. 362–366, 2009.

126. D. Venkatesh, M. S. R. Prasad, B. R. Babu, K. V. Ramesh, K. Trinath, and 1C, "Effect of sintering temperature on the structure and magnetic properties of Ni-Zn Nanoferrites," *J. Magn.*, vol. 20, pp. 229–240, 2015.

127. S. Singh, N. Kumar, A. Jha, M. Sahni, R. Bhargava, A. Chawla, R. Chandra, S. Kumar, and S. Chaubey, "Effect of annealing temperature on the physical properties of Zn-ferrite nanoparticles," *J. Supercond. Nov. Magn*., vol. 27, pp. 821–826, 2014.

128. C. N. Chinnasamy, A. Narayanasamy, N. Ponpandian, K. Chattopadhyay, K. Shinoda, B. Jeyadevan, K. Tohji, K. Nakatsuka, T. Furubayashi, and I. Nakatani, "Mixed spinel structure in nanocrystalline NiFe2O4," *Phys. Rev. B*, vol. 63, pp. 184108, 2001.

129. X. Li, Q. Li, Z. Xia, and W. Yan, "Effects on direct synthesis of large scale mono-disperse Ni0.5Zn0.5Fe2O4 nanosized particles," *J. Alloys Compd*., vol. 458, pp. 558–563, 2008.

130. G. R. Kumar, "Synthesis, structural and magnetic properties of copper substituted nickel ferrites by sol-gel method," *Mater. Sci. Appl*., vol. 3, pp. 87–91, 2012.

131. P. K. C. and B. K. N. and S. B. and S. D. and K. G. and U. K. and P. K. M. and D. D. and M. A. and F. Mazaleyrat, "Magnetic and hyperfine properties of nanocrystalline Ni0.2 Zn 0.6 Cu 0.2 Fe2O4 prepared by a chemical route," *J. Phys. Condens. Matter*, vol. 18, pp. 5253, 2006.

132. M. A. Khan, M. Javid Ur Rehman, K. Mahmood, I. Ali, M. Niaz Akhtar, G. Murtaza, I. Shakir, and M. Farooq Warsi, "Impacts of Tb substitution at cobalt site on structural, morphological and magnetic properties of cobalt ferrites synthesized via double sintering method," *Ceram. Int*., vol. 41, pp. 2286–2293, 2015.

133. R. Kumar, H. Kumar, M. Kumar, R. R. Singh, and P. B. Barman, "Enhanced saturation magnetization in cobalt doped ni-zn ferrite nanoparticles," *J. Supercond. Nov. Magn*., vol. 28, pp. 3557–3564, 2015.

134. B. H. Guan, L. K. Chuan and H. Soleimani "synthesis, characterization and influence of calcinations temperature on magnetic properties of Ni0.75Zn0.25Fe2O4 nanoparticles synthesized by sol-gel technique," *Am. J. Appl. Sci.,* vol. 11, pp. 878–882, 2014.

135. P. Gao, E.V. Rebrov, T. M. Verhoeven, J.C. Schouten, R. Kleismit, G. Kozlowski, J. Cetnar, Z. Turgut and G. Subramanyam "Structural investigations and magnetic properties of *sol-gel* Ni 0.5Zn0.5Fe2O4 thin films for microwave heating," *J. Appl. Phys*., vol. 107, pp. 0–8, 2010.

136. E. J. Choi, Y. Ahn, K.-C. Song, D. H. An, B. Lee, and K. U. Kang, "Cation distribution and spin-canted structure in cobalt ferrite particles from a cobalt-iron hydroxide carbonate complex," *J. Korean Phys. Soc*., vol. 44, pp. 1518–1520, 2004.

137. M. K. Fayekt, A. A. Bahgat, Y. M. Abbas, and L. Moberg, "Neutron diffraction and mossbauer effect study on a cobalt substituted zinc ferrite," *J. Phys. C Solid State Phys.*, vol. 15, pp. 2509–2518, 1982.

138. A. M. Kumar, P. A. Rao, M. C. Varma, G. Choudary, and K. H. Rao, "Cation distribution in $Co_{0.7}Me_{0.3}Fe_2O_4$," *J. Mod. Phys*., vol. 2, pp. 1083–1087, 2011.

139. R. S. Yadav, J. Havlica, J. Masilko, L. Kalina, M. Hajdúchová, V. Enev, J. Wasserbauer, I. Kuřitka, and Z. Kozakova, "Structural, cation distribution, and magnetic properties of CoFe2O4 spinel ferrite nanoparticles synthesized using a starch-assisted sol–gel auto-combustion method," *J. Supercond. Nov. Magn*., vol. 28, pp. 1851–1861, 2015.

140. K. Nadeem, S. Rahman, and M. Mumtaz, "Effect of annealing on properties of Mg doped Zn-ferrite nanoparticles," *Prog. Nat. Sci. Mater. Int*., vol. 25, pp. 111–116, 2015.

141. A. Kumar, M. Chandra, P. Kumar, M. Kumar, M. A. G. Soler, and A. Agarwal, "Structural, optical and photoconductivity of Sn and Mn doped TiO 2 nanoparticles," *J. Alloys Compd.*, vol. 622, pp. 37–47, 2015.

142. S. Dhara, K. Imakita, P. K. Giri, and M. Fujii, "Strain dependence of the nonlinear optical properties of strained Si nanoparticles.," *Opt. Lett.*, vol. 39, pp. 3833–3836, 2014.

143. Y. Köseoğlu, F. Alan, M. Tan, R. Yilgin, and M. Öztürk, "Low temperature hydrothermal synthesis and characterization of Mn doped cobalt ferrite nanoparticles," *Ceram. Int.*, vol. 38, pp. 3625–3634, 2012.

144. K. Maaz, A. Mumtaz, S. K. Hasanain, and A. Ceylan, "Synthesis and magnetic properties of cobalt ferrite (CoFe2O4) nanoparticles prepared by wet chemical route," *J. Magn. Magn. Mater.*, vol. 308, pp. 289–295, 2007.

145. S. Chakrabarty, A. Dutta, and M. Pal, "Enhanced magnetic properties of doped cobalt ferrite nanoparticles by virtue of cation distribution," *J. Alloys Compd.*, vol. 625, pp. 216–223, 2015.

146. S. Xavier, S. Thankachan, B. P. Jacob, and E. M. Mohammed, "Effect of sintering temperature on the structural and magnetic properties of cobalt ferrite nanoparticles," *Nanosyst.: Phys. Chem. Math.,* vol. 4, pp. 430–437, 2013.

147. H. Igarashi and K. Okazaki, "Effects of porosity and grain size on the magnetic properties of NiZn ferrite," *J. Am. Ceram. Soc.*, vol. 60, pp. 51–54, 1977.

148. S. W. Lee and C. S. Kim, "Superparamagnetic properties Ni-Zn ferrite for nano-bio fusion applications," *J. Magn. Magn. Mater.*, vol. 304, pp. 418–420, 2006.

149. T. Nakamura, "Snoek's limit in high-frequency permeability of polycrystalline Ni–Zn, Mg–Zn, and Ni–Zn–Cu spinel ferrites," *J. Appl. Phys.*, vol. 88, pp. 348-353, 2000.

150. T. Nakamura, "Low-temperature sintering of Ni-Zn-Cu ferrite and its permeability spectra," *J. Magn. Magn. Mater.*, vol. 168, pp. 285–291, 1997.

151. E. Manova, D. Paneva, B. Kunev, E. Rivière, C. Estournès, and I. Mitov,"Characterization of nanodimensional Ni-Zn ferrite prepared by mechanochemical and thermal methods," *J. Phys. Conf. Ser.*, vol. 217, pp. 12102, 2010.

152. B. T. Naughton, P. Majewski, and D. R. Clarke, "Magnetic properties of nickel-zinc ferrite toroids prepared from nanoparticles," *J. Am. Ceram. Soc.*, vol. 90, pp. 3547–3553, 2007.

153. P. E. Meskin, V. K. Ivanov, A. E. Barantchikov, B. R. Churagulov, and Y. D. Tretyakov, "Ultrasonically assisted hydrothermal synthesis of nanocrystalline ZrO 2, TiO2, NiFe2O4 and Ni 0.5Zn0.5Fe2O4 powders," *Ultrason. Sonochem.*, vol. 13, pp. 47–53, 2006.

154. C. Upadhyay, H. C. Verma, and S. Anand, "Cation distribution in nanosized Ni-Zn

ferrites," *J. Appl. Phys.*, vol. 95, pp. 5746–5751, 2004.

155. S. Thakur, S. C. Katyal, A. Gupta, V. R. Reddy, S. K. Sharma, M. Knobel, and M. Singh, "Nickel - Zinc ferrite from reverse micelle process: Structural and magnetic properties, mössbauer spectroscopy characterization," *J. Phys. Chem. C*, vol. 113, pp. 20785–20794, 2009.

156. M. Sivakumar, T. Takami, H. Ikuta, A. Towata, K. Yasui, T. Tuziuti, T. Kozuka, D. Bhattacharya, and Y. Iida, "Fabrication of zinc ferrite nanocrystals by sonochemical emulsification and evaporation: Observation of magnetization and its relaxation at low temperature," *J. Phys. Chem. B*, vol. 110, pp. 15234–15243, 2006.

157. S. Verma, P. A. Joy, and S. Kurian, "Structural, magnetic and m??ssbauer spectral studies of nanocrystalline Ni0.5Zn0.5Fe2O4 ferrite powders," *J. Alloys Compd.*, vol. 509, pp. 8999–9004, 2011.

158. B. P. Rao, C.-O. Kim, C. Kim, I. Dumitru, L. Spinu, and O. F. Caltun, "Structural and magnetic characterizations of co-precipitated NiZn and MnZn ferrite nanoparticles," *IEEE Trans. Magn.*, vol. 42, pp. 2858–2860, 2006.

159. D. Rathore, R. Kurchania, and R. K. Pandey, "Structural, magnetic and dielectric properties of Ni1− x Zn x Fe2O4 (x= 0, 0.5 and 1) nanoparticles synthesized by chemical co-precipitation method," *J. nanosci. nanotech.*, vol. 13, pp. 1812-1819, 2013.

160. A. S. Albuquerque, J. D. Ardisson, W.A. Macedo, and M. C. Alves, "Nanosized powders of NiZn ferrite: synthesis, structure, and magnetism," *J. Appl. Physics*, vol. *87,* pp.4352-4357, 2000.

161. K. Gheisari, S. D. Bhame, J. T. Oh, and S. Javadpour, "Comparative studies on the structure and magnetic properties of Ni-Zn ferrite powders prepared by glycine-nitrate auto-combustion process and solid state reaction method," *J. Supercond. Nov. Magn.*, vol. 26, pp. 477–483, 2013.

162. M. Abdullah Dar, J. Shah, W. A. Siddiqui, and R. K. Kotnala, "Study of structure and magnetic properties of Ni–Zn ferrite nano-particles synthesized via co-precipitation and reverse micro-emulsion technique," *Appl. Nanosci.*, vol. 4, pp. 675–682, 2014.

163. X. Lu, G. Liang, Q. Sun, and C. Yang, "High-frequency magnetic properties of Ni-Zn ferrite nanoparticles synthesized by a low temperature chemical method," *Mater. Lett.*, vol. 65, pp. 674–676, 2011.

164. P. Parsons, K. Duncan, A. K. Giri, J. Q. Xiao, and S. P. Karna, "Electromagnetic properties

of NiZn ferrite nanoparticles and their polymer composites," *J. Appl. Phys*., vol.115, pp. 0–8, 2014.

165. E. Ateia, L. M. Salah, and A. A. H. El-Bassuony, "Investigation of cation distribution and microstructure of nano ferrites prepared by different wet methods," *J. Inorg. Organomet. Polym. Mater*., vol. 25, pp. 1362–1372, 2015.

165. N. Ponpandian and A. Narayanasamy, "Influence of grain size and structural changes on the electrical properties of nanocrystalline zinc ferrite," *J. Appl. Phys*., vol. 92, pp. 2770–2778, 2002.

167. G. Thirupathi and R. Singh, "Magnetic properties of zinc ferrite nanoparticles," *IEEE Trans. On Magnetics*, vol. 48, pp. 3630–3633, 2012.

168. M. Asif Iqbal, M. U. Islam, M. N. Ashiq, I. Ali, A. Iftikhar, and H. M. Khan, "Effect of gd-substitiution on physical and magnetic properties of Li 1.2Mg0.4 Gdx Fe(2-x)O4 ferrites," *J. Alloys Compd*., vol. 579, pp. 181–186, 2013.

169. G. A. Petitt and D. W. Forester "Mossbauer study of cobalt-zinc ferrites," *Phys. Rev. B*, Vol. 4, pp. 3912-3923, 1971.